Politecnico di Bari

Department of Mechanics, Mathematics and Management
MECHANICAL AND MANAGEMENT ENGINEERING
Ph.D. Program
SSD: ING-IND/14–MECHANICAL DESIGN AND MACHINE CONSTRUCTION

Final Dissertation

Development of innovative methods for residual stress analysis in advanced materials

---

by
SIMONE CARONE

Supervisors:
Prof. Caterina CASAVOLA
Prof. Giovanni PAPPALETTERA

Coordinator of Ph.D. Program:
Prof. Giuseppe Pompeo DEMELIO

Course n°36, 01/11/2020-31/03/2024

Politecnico di Bari

Department of Mechanics, Mathematics and Management
MECHANICAL AND MANAGEMENT ENGINEERING
Ph.D. Program
SSD: ING-IND/14–MECHANICAL DESIGN AND MACHINE CONSTRUCTION

Final Dissertation

Development of innovative methods for residual stress analysis in advanced materials

---

by

SIMONE CARONE

Referees:

Prof. Antonio BALDI

Eng. Giuseppe BARBIERI

Supervisors:

Prof. Caterina CASAVOLA

Prof. Giovanni PAPPALETTERA

Coordinator of Ph.D. Program:

Prof. Giuseppe Pompeo DEMELIO

Course n°36, 01/11/2020-31/03/2024

Abstract

Residual stress assessment is a key factor in engineering design owing to its impact on engineering properties of materials and structural components. Improper management of residual stresses can result in distortion, reduced fatigue life, degraded corrosion resistance, brittle fracture, and even failure during component fabrication, especially with technologies such as welding and additive manufacturing. Therefore, in the context of sustained industrial development for producing advanced components for cutting-edge applications, there is a need to advance residual stress measurement methods to make assessments faster and more reliable.

In this thesis, two residual stress measurement techniques have been adopted and improved: the contour method and hole drilling.

The first part of the thesis focuses on the contour method. A critical aspect of this technique is the time required to accurately measure the deformed surfaces after cutting the part. Therefore, in this thesis we adopted a full-field optical technique to expedite the surface acquisition step of the contour method. However, due to this approach, it was necessary to modify the subsequent processing of the point clouds of the deformed cut surfaces. Data located at the perimeter of the point clouds had to be excluded. Nevertheless, when compared to the data obtained by coordinate measuring machines, which is the standard profile acquisition technique in the contour method, the initial data points are closer to the perimeter, with a distance of only 0.2 mm. Using the optical technique, we obtained richer data that allowed us to measure the residual stress field in specimens only 2 mm thick, which is at the limits of the contour method. The contour method is attractive because of its insensitivity to microstructural changes, which makes it particularly suitable for the study of joints between different materials. In this thesis, the contour method was used to characterize residual stress fields in various types of advanced multi-material joints fabricated by laser welding and metal additive manufacturing.

The second part of the thesis is dedicated to the hole drilling technique. A tool based on a probabilistic machine learning framework has been developed to reduce instability problems notoriously associated with this technique. The proposed approach also enables quantification of the uncertainty of the final measurement output related to the fitting procedure of the strains measured using strain gauge rosettes. The developed methodology was finally applied to measure the residual stresses in advanced laser shock-peened aluminum AA 7050-T7451 specimens.

Contents

Chapter 1. Residual stresses: state of the art

1.1 Residual stress

Residual stresses are stresses that exist within materials and structures independently of external loads (forces and moments) or thermal gradients. Thus, these stresses have the property of being globally self-equilibrated [1–4]:

$$\int \boldsymbol{\sigma}\, dA = 0 \tag{1}$$

$$\int \boldsymbol{z} \times \boldsymbol{\sigma}\, dA = 0 \tag{2}$$

where $\boldsymbol{\sigma}$ is the stress in a point, dA is the infinitesimal area and $\boldsymbol{z}$ is the distance from a reference point.

Residual stresses can also be classified by the length of the region in which they equilibrate, which is referred to as l_0 [5]:

- Type I: Macro residual stresses which self-equilibrate over a length l_0^I larger than the grain size of the material and comparable to the macroscopic dimension of the component; Type I stresses are continuous between different phases and across grain boundaries (Figure 1(a));
- Type II: Micro residual stresses which vary on the scale of a single grain; in multi-phase materials these stresses are discontinuous between different phases (Figure 1(b));
- Type III: Micro residual stresses that are internal to a grain, essentially due to the presence of dislocations and other crystalline defects (Figure 1(c)).

In the design of composite materials, Type II residual stresses may also be of significance because of load transfer problems between the matrix and the reinforcement. However, in general, the most critical residual stresses to be aware of are Type I residual stresses. Most measurement techniques have been developed

for measuring these types of residual stresses, although they can be adapted to smaller scales to measure micro-stresses.

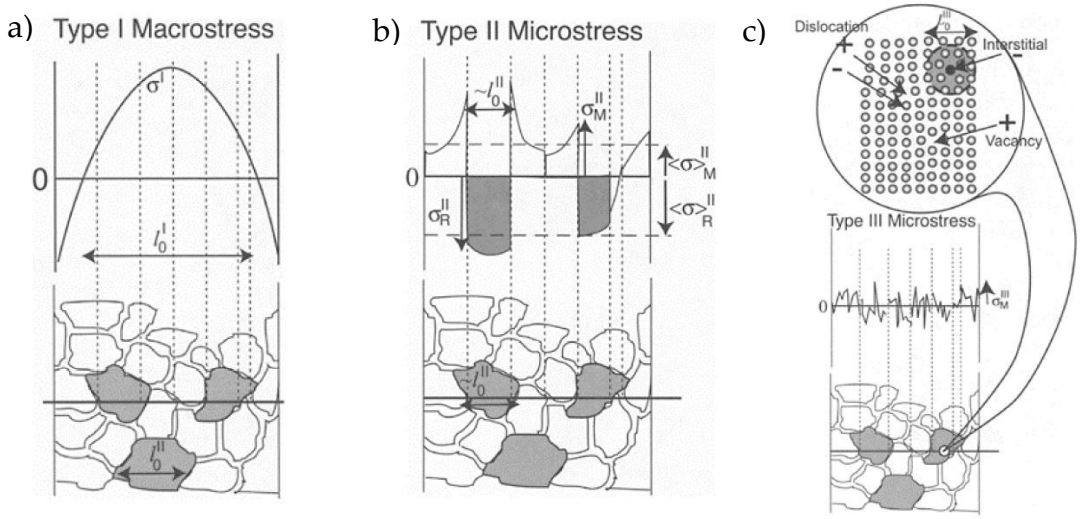

Figure 1. Classification of residual stresses according to the length over which they are balanced; (a) Type I macro-stress varies on a length scale $\boldsymbol{l_0^I}$ that is a considerable fraction of the sample size; (b) Type II micro-stress varies on a length scale $\boldsymbol{l_0^{II}}$ that is approximately equal to the grain size; (c) Type III micro-stress varies on a length scale $\boldsymbol{l_0^{III}}$ which is much smaller than the grain size [5].

Residual stresses are typically generated during fabrication processes as a result of misfits between different regions. These stresses can occur during thermal processes such as welding, casting, heat treatments, and additive manufacturing where non-uniform cooling or solidification results in different contraction or expansion in different regions of the material. Residual stresses can also be produced by non-uniform plastic deformation such as by bending and rolling, or by surface modifications during machining, grinding and carburizing. Additionally, they can be intentionally induced by surface treatments, such as shot peening, sand blasting or laser shock peening, to create a compression layer that enhances the fatigue life of the part (Figure 2).

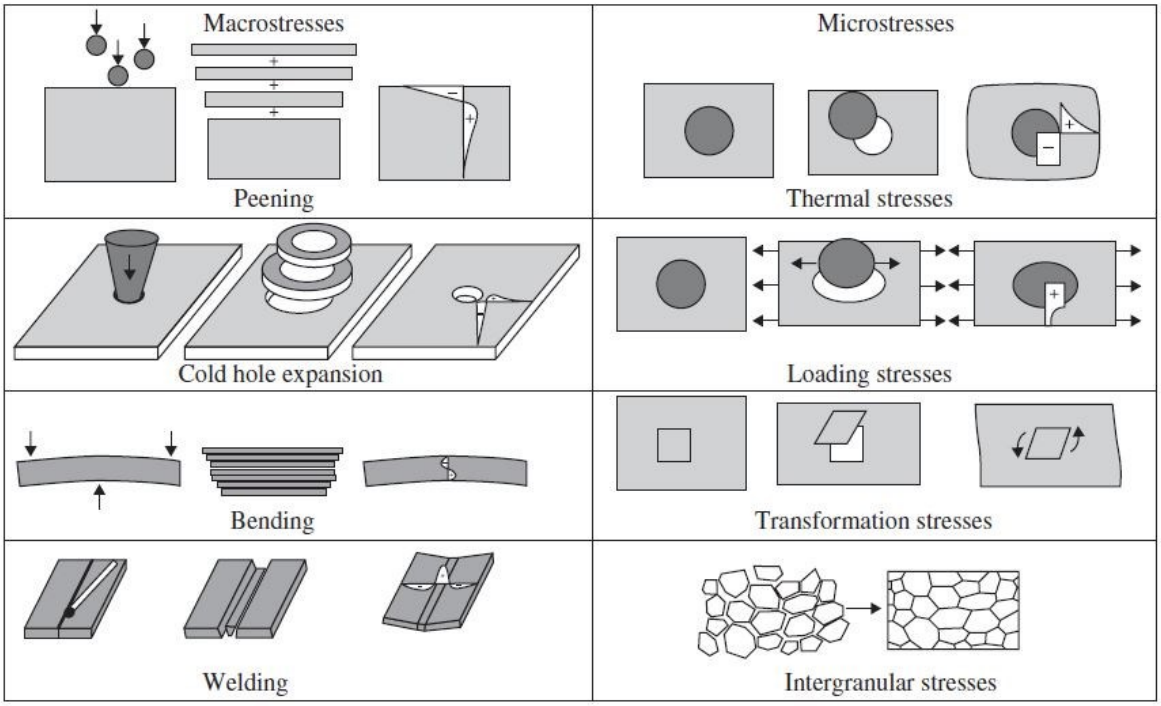

Figure 2. Examples of common ways via which residual stress occurs in engineering materials [6].

Residual stresses play a crucial role in engineering design as they can interact with in-service loads. Depending on their sign and location, they can have either a positive or negative impact on structural behavior of components. Moreover, they affect mechanical properties of parts, notably distortion, fatigue life, dimensional stability, corrosion resistance and failure mechanism [1,7–9]. Figure 3 illustrates the consequences of neglecting residual stresses during manufacturing processes.

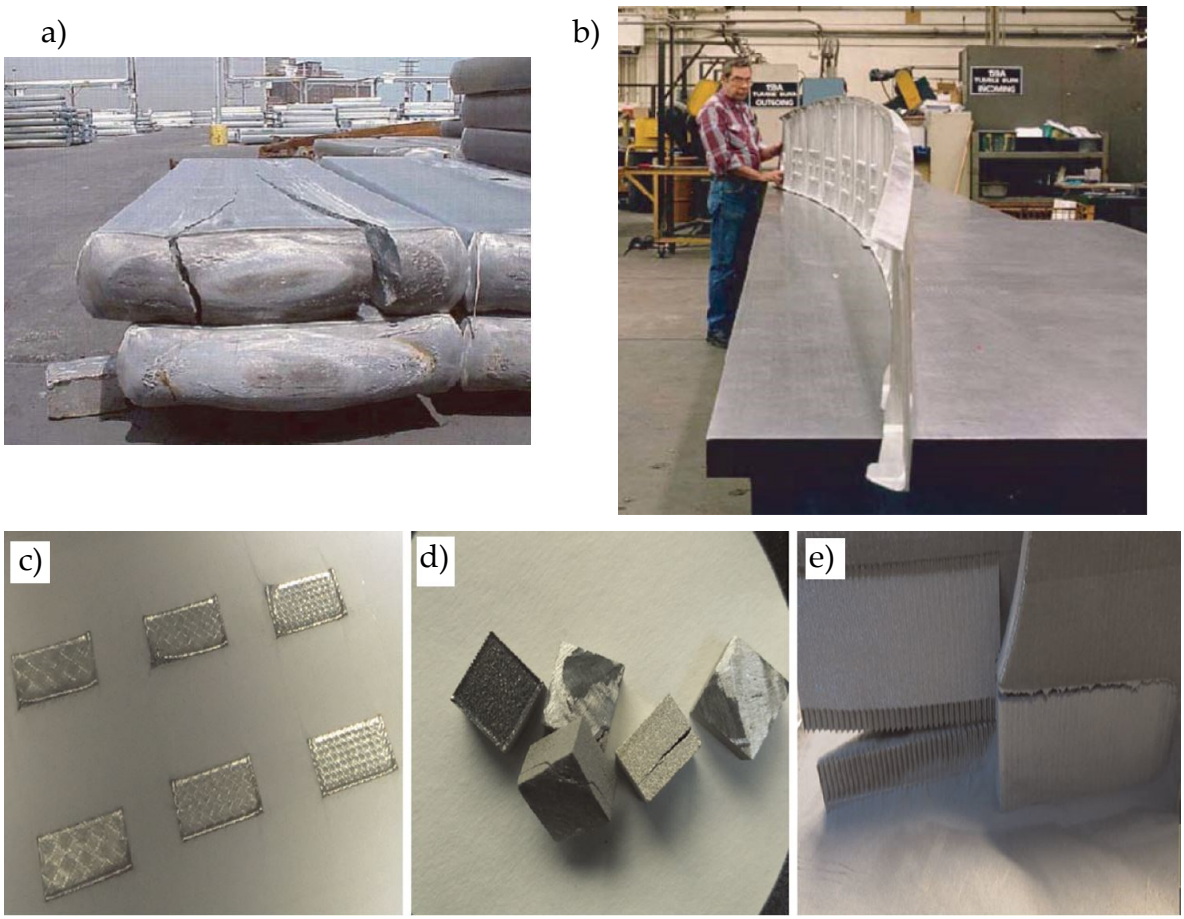

Figure 3. (a) Excessive residual stresses causing cracking in a cast aluminum ingot [2]; (b) Warpage of a Boeing C-17 cargo ramp caused by residual stress release after machining [2]; (c) warpage, (d) cracking and (e) base plate separation occurred during selective laser melting process [10].

1.2 Residual stress measurement techniques

Various techniques can be used to measure residual stresses, depending on several factors such as the material being examined, the required measurement resolution and depth, the damage caused to the component, and the cost and availability of the necessary instrumentation [2] (Figure 4).

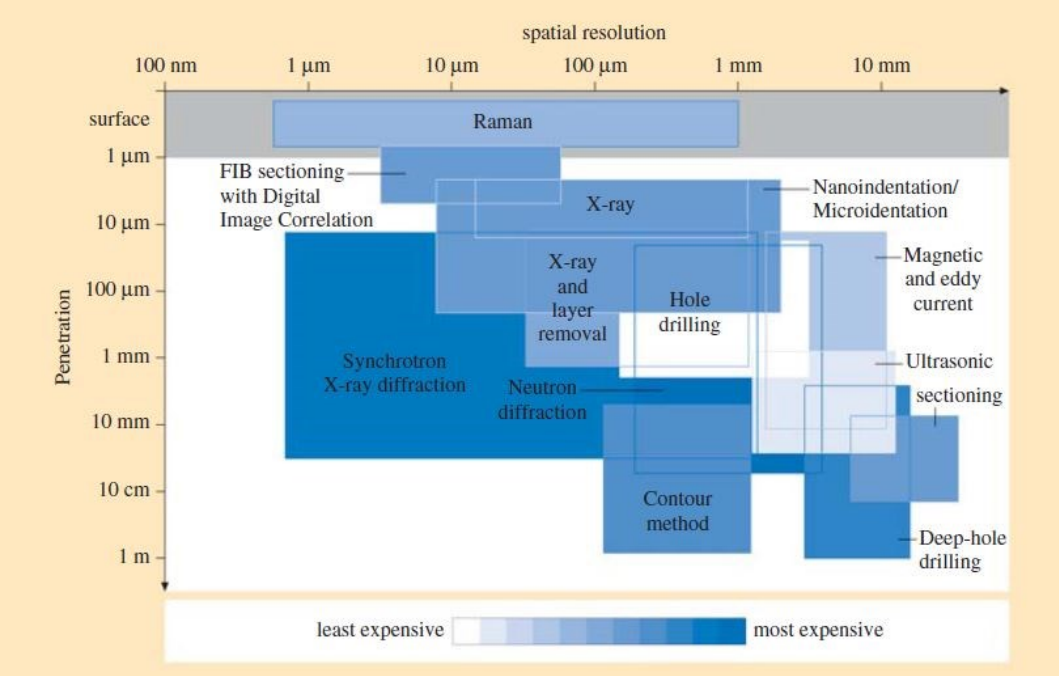

Figure 4. Scheme of the application range of residual stress measurement techniques based on their spatial resolution, depth of penetration into the material, and cost of measurement [2].

Residual stress measurement methods can be divided into nondestructive and destructive procedures.

The main nondestructive methods include diffraction-based, magnetic, and ultrasonic methods. The main destructive or semi-destructive methods include hole-drilling, ring-core, deep-hole, slitting, indentation, and contour methods.

This thesis will study and develop the contour method and hole-drilling. A more extensive description of these techniques will be provided in the following sections. Brief descriptions of the other mentioned techniques and their measurement principle will also be given.

Diffraction-based measurement methods employ electromagnetic radiation to measure the inter-atomic lattice spacing in crystalline materials [2,11]. A residual stress field deforms this spacing relative to the free-stress state. In diffraction-based techniques the interplanar dimension of the crystal is measured in order to determine the magnitude and direction of the residual stress field in the material. When electromagnetic radiation interacts with regularly arranged atoms or lattices a diffraction phenomenon occurs, causing incident rays to diffract in different directions and generating interference phenomena. The Bragg angle θ describes the angle for which constructive interference is produced, as stated by Bragg's law:

$$n\,\lambda = 2\,d\,sin\theta \tag{3}$$

where n is an integer, λ is the radiation wavelength and d is the lattice distance. From equation (3) the strain ϵ can be computed by knowing the variation in the Bragg angle $\Delta\theta$:

$$\epsilon = \frac{\Delta d}{d} = -cot\theta\;\Delta\,\theta \tag{4}$$

It is therefore necessary to have an accurate measurement of the interplanar spacing in absence of residual stresses, d_0. The difference among measurement methods that rely on the diffraction principle is primarily related to the depth of radiation penetration. Laboratory X-ray diffraction can probe a thin surface layer of specimens, usually tens of micrometers. Synchrotron sources use X-rays at much higher energy levels ($20 - 300\,keV$), allowing for much deeper penetration into materials, on the order of millimeters. In neutron diffraction, neutrons are scattered by interacting with the nuclei of atoms, rather than with electrons, as in X-rays, and can penetrate several centimeters into the material.

Magnetic Barkhausen Noise is a technique used to measure surface and sub-surface residual stresses in ferromagnetic materials. When an external magnetic field is applied, the magnetic domains in these materials reorient, resulting in small, irregular jumps in induced magnetism. These jumps can cause voltage pulses across a sensor coil, which are random in amplitude, duration, and temporal separation, and are therefore referred to as noise. The amount and character of noise produced is affected by the presence of residual stresses, which influence the way in which local magnetic changes occur. Thus, measuring and analyzing the Barkhausen noise can identify the residual stresses present in a ferromagnetic material.

The ultrasonic method involves feeding an ultrasonic wave into the material and measuring either the transmitted, reflected, or scattered wave. This method can detect residual stresses by measuring the speed at which the wave travels through the component. However, accurately measuring residual stresses using ultrasound can be challenging due to various factors such as grain size, defects in the component, and crystallographic texture, which also influence the ultrasound velocity. Therefore, it is crucial to consider these factors to obtain reliable measurements.

Indentation is considered a semi-destructive method because it causes minor damage to the component, but does not compromise its functionality. This technique has been widely used for measuring various mechanical properties, including hardness, Young's modulus, and yield strength. Recently, it has also been used to measure residual stresses. The reliability of this method is highest when measuring equibiaxial residual stress states, where the magnitude and sign of the principal components of the residual stresses are equal. Efforts are currently underway to extend its applicability to all possible stress states. This technique for measuring material properties is based on the phenomenon that the load required to indent a material at a given depth varies depending on the residual stresses present. When operating under displacement control, compressive stresses result in a greater load than a stress-free state, while tensile stresses result in a lower load.

Destructive techniques are based on the principle of residual stress relaxation that occurs following the removal of material. This relaxation results in deformation or displacement, which can be measured in the vicinity of the damage. The stresses originally present can then be calculated through an inversion process.

Hole drilling is one of the most commonly used destructive techniques for measuring surface and sub-surface residual stresses. Although a separate section will be devoted to this technique, a brief description is given here as other measurement methods are based on it. The measurement principle involves introducing a small hole at the position where residual stresses are to be measured. The residual stresses are relieved by the drilling process and the strains are measured at the surface by means of strain gauges placed around the hole. Figure 5 schematically illustrates the relaxation of residual stress after hole drilling. Residual stresses are calculated from the measured strains using calibration constants that depend on the type of strain gauge rosette used.

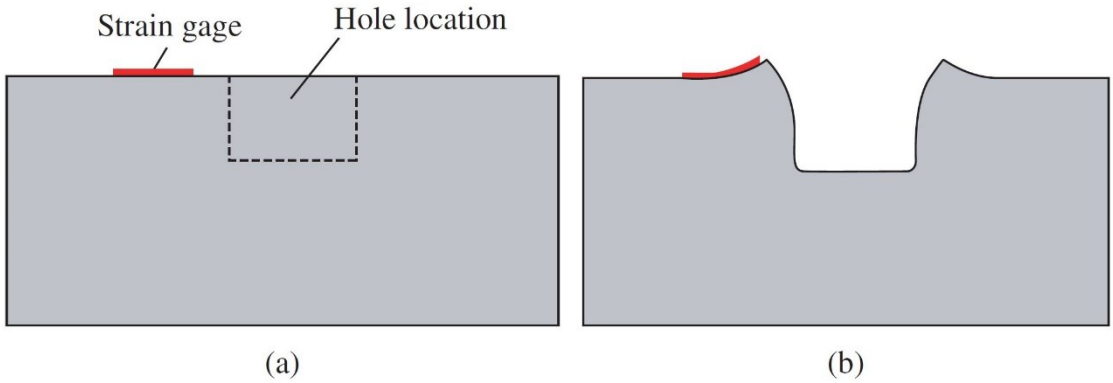

Figure 5. Schematic illustration of residual stress relaxation in hole drilling; (a) material cross-section before drilling; (b) material cross-section after drilling [12].

Figure 6 depicts the ring-core method, a variation of hole drilling, which involves drilling a cavity and placing a strain gage rosette in its center. This method enables the measurement of larger residual stresses due to the larger strains that can be obtained. However, it causes more damage to the component.

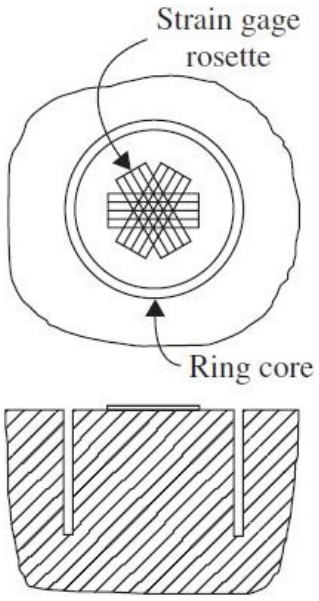

Figure 6. Ring core method [2].

The deep-hole method is also a variation of hole drilling. A hole is drilled through the thickness of the component, and its diameter is accurately measured. Then, an annular groove is drilled around the central hole. By measuring the variation in the diameter of the central hole, it is possible to trace the residual stresses that have relaxed as a result of making the groove. Figure 7 shows a schematic of this measurement method.

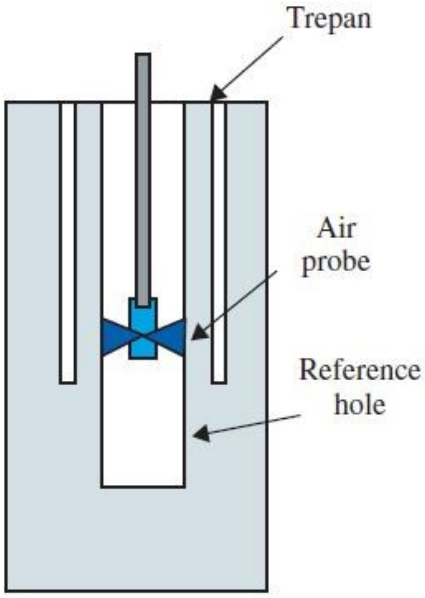

Figure 7. Deep hole method [2].

The slitting method involves stress relaxation through material removal by cutting a long slit along the thickness of the part. Strain gauges are placed on both the top and back surfaces to measure strains as the slit is incrementally cut. The cut can be made using a milling cutter or wire electro discharge machining (EDM). This technique allows for measuring residual stresses at depth, but it can only measure the residual stress component normal to the plane along which the slit is made.

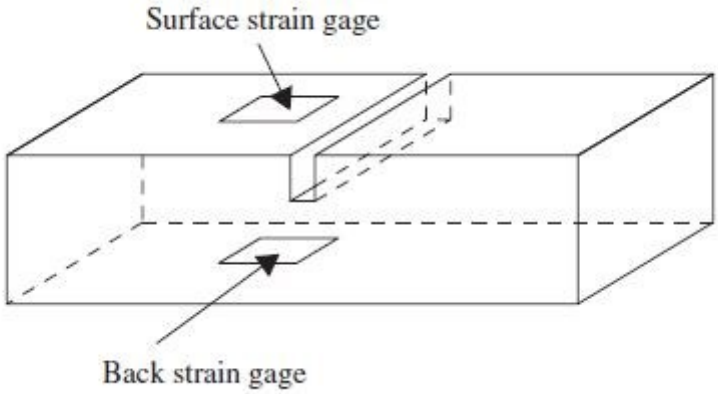

Figure 8. Slitting method [2].

1.3 Contour Method

The contour method is based on the principle of residual stress relaxation after material removal and it was invented by Prime in 2001 [13]. To conduct the measurement, the specimen is carefully cut into two parts, and the displacements

on the two new faces resulting from the cut are measured. By imposing the measured displacements as boundary conditions on a finite element (FE) model of the component and solving a static analysis, it is possible to trace the residual stresses normal to the cut plane. This provides a two-dimensional map of the residual stresses normal to the cutting plane along the entire cross section [14].

This technique is especially useful for measuring residual stress fields with high gradients, such as those found in welds, which can be more challenging to measure with point-wise techniques. Furthermore, this method is insensitive to microstructural gradients and has no limitations in terms of size and geometry complexity, making it ideal for measurements on welds and parts produced by additive manufacturing. However, it is currently limited to metals due to the required cutting accuracy achievable only through wire-EDM, which is applicable only to conductive materials.

1.3.1 Measurement Principle

The contour method theory applies Bueckner's principle. This principle states that if a cracked body under external loads has forces applied to the crack surfaces that close the crack, these forces must be equivalent to the stress distribution in an uncracked body of the same geometry under the same external load. This statement is derived from the principle of superposition, as shown in Figure 9. The equivalence of the stress intensity factors resulting from the external loads and those resulting from the tensile forces on the crack surfaces is demonstrated by the Bueckner's principle.

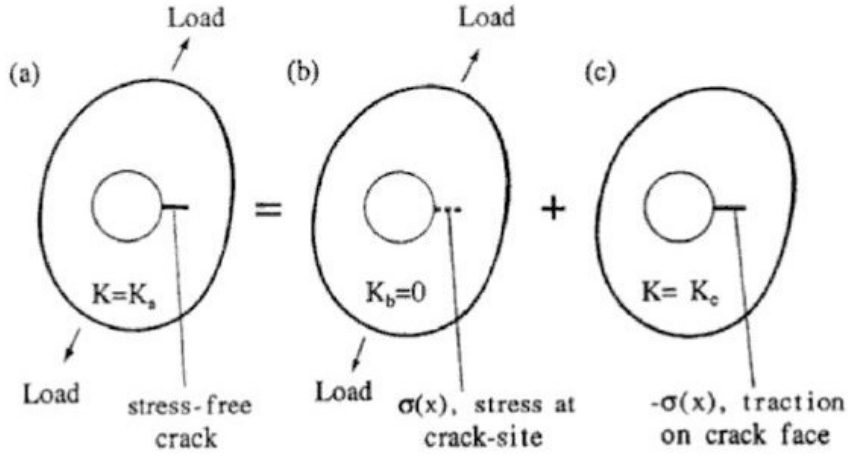

Figure 9. Application of the Bueckner's superposition principle [15].

The contour method is based on the measurement principle illustrated in

Figure 10. The figure displays a thick plate with residual stresses along the longitudinal direction (x) that vary according to a parabolic function throughout the plate's thickness. State A represents the undisturbed specimen with the residual stresses to be determined, as shown in only one quarter of the specimen. In state B, the component was divided into two parts along the plane at $x = 0$ and deformed due to relaxation of residual stresses. In state C, the cut and deformed surface of the component (without residual stresses), is forced back to its original shape, generating a change in stresses. Superimposing the stress field in B with that in C yields the original residual stresses in state A:

$$\sigma^A(x, y, z) = \sigma^B(x, y, z) + \sigma^C(x, y, z) \tag{5}$$

where σ indicates the whole stress tensor and the superscripts refer to the different states in Figure 10.

Using the described principle, it is only possible to determine the original stress distribution of state A along the cut plane x=0, since the stresses σ_x , τ_{xy}, and τ_{xz} are equal to zero on the newly formed free surface in state B.

As it is not experimentally feasible to measure the in-plane displacements relative to the deformed surface as a result of cutting, but only the displacements perpendicular to the cut plane, this measurement principle, together with some assumptions, can be used to experimentally determine the residual stresses normal to the cut plane: $\sigma_x^A(0, y, z)$. Therefore, a first approximation is to return the cut surface to its original position only in the direction normal (x) to the cut plane (state C), leaving the transverse displacements unconstrained. In the final step of the technique, which consists of a finite element analysis, leaving the transverse displacements unconstrained results in the automatic application of the conditions $\tau_{xy} = 0$ and $\tau_{xz} = 0$. Thus, the contour method makes it possible to measure the normal stresses σ_x and not the tangential stresses τ_{xy} and τ_{xz}.

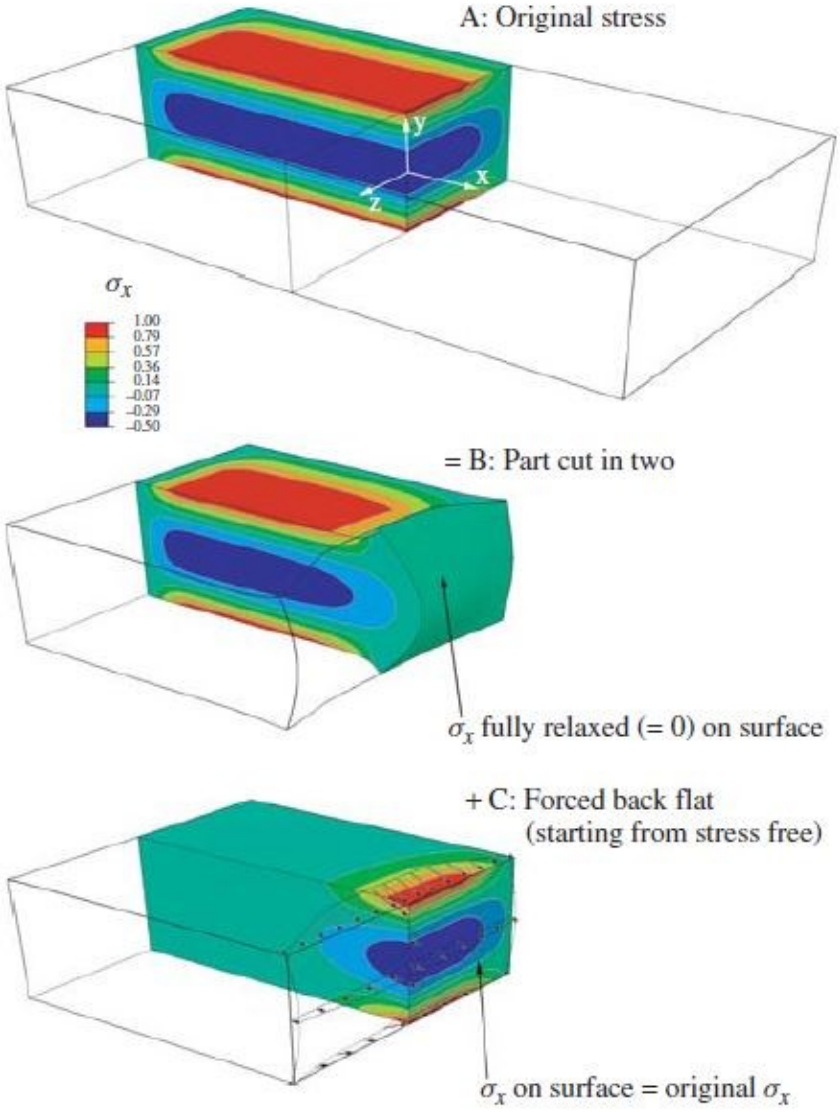

Figure 10. Measurement principle of the contour method [14].

However, transverse residual stresses may still be present in a part to be measured. Therefore, to eliminate their contribution, it is necessary to average the profiles measured from both cut surfaces, thus isolating only the normal stress contribution to the deformation of these new surfaces. To give a theoretical explanation, the deformations caused by residual stresses can be evaluated by the equivalent surface traction in the cut plane. For a cut surface with a single normal along the x-direction ($n_y = 0$), this equivalent stress $\boldsymbol{T}$ is given by:

$$T_x = -\sigma_x n_x, \quad T_y = -\tau_{xy} n_x \tag{6}$$

Figure 11 illustrates how the normal traction T_x is symmetrical to the cut plane, whereas the transverse traction T_y is antisymmetric. Therefore, averaging the two

profiles of the cut surfaces results in a single profile with only the normal stress contribution [13].

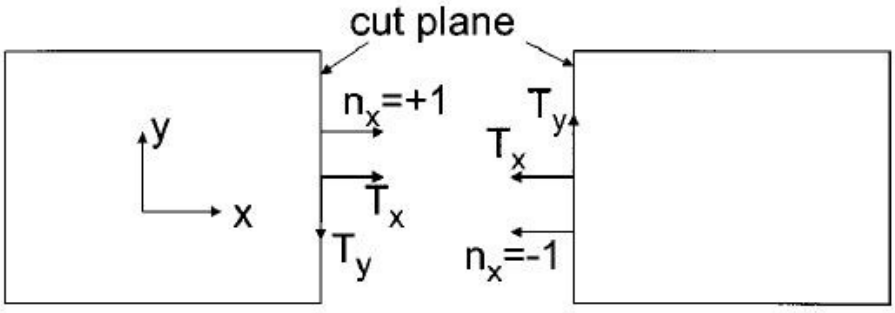

Figure 11. Surface tractions equivalent to residual stress release on the cut surface [13].

Having thus obtained a profile with only the contribution of the residual stresses normal to the cut plane, and considering that in state B (Figure 10) the residual stresses on the free surface are zero, it can be written from equation (5):

$$\sigma_x^B(0,y,z) = 0 \Downarrow \sigma_x^A(0,y,z) = \sigma_x^C(0,y,z) \quad (7)$$

which is the implementation of the contour method.

Some other assumptions and approximations are necessary for the standard implementation of the contour method:

- the superposition principle assumes that the material behaves elastically during residual stress relaxation and that the cutting process does not introduce itself stresses that influence the measurement;
- to simplify the FE modeling and analysis, since the deformations are rather small and it is a linear analysis, in state C, the newly formed surface can be modeled as flat and then forced into the opposite of the measured profile;
- to isolate only the normal stress contribution when averaging the cut surface profiles, the stiffnesses of the two cut parts must be the same. For homogeneous materials, if a symmetric part is cut in half, this assumption is satisfied. However, if the cut is asymmetric, a variation of the standard procedure must be adopted. This variation will be explained in the following chapters.

1.3.2 Practical Measurement Implementation

The practical implementation of the contour method consists of the following steps (Figure 12):

- make a straight cut through the specimen, perpendicular to the stress component of interest;
- measure the profiles of the two cut surfaces;
- align and average the two acquired profiles;
- fit the averaged displacements to enable evaluation at any location;
- build a FE model of the cut specimen;
- apply the displacements, with reverse sign, as boundary conditions in the FE model;
- perform a static FE analysis and retrieve the original residual stresses normal to the cut plane.

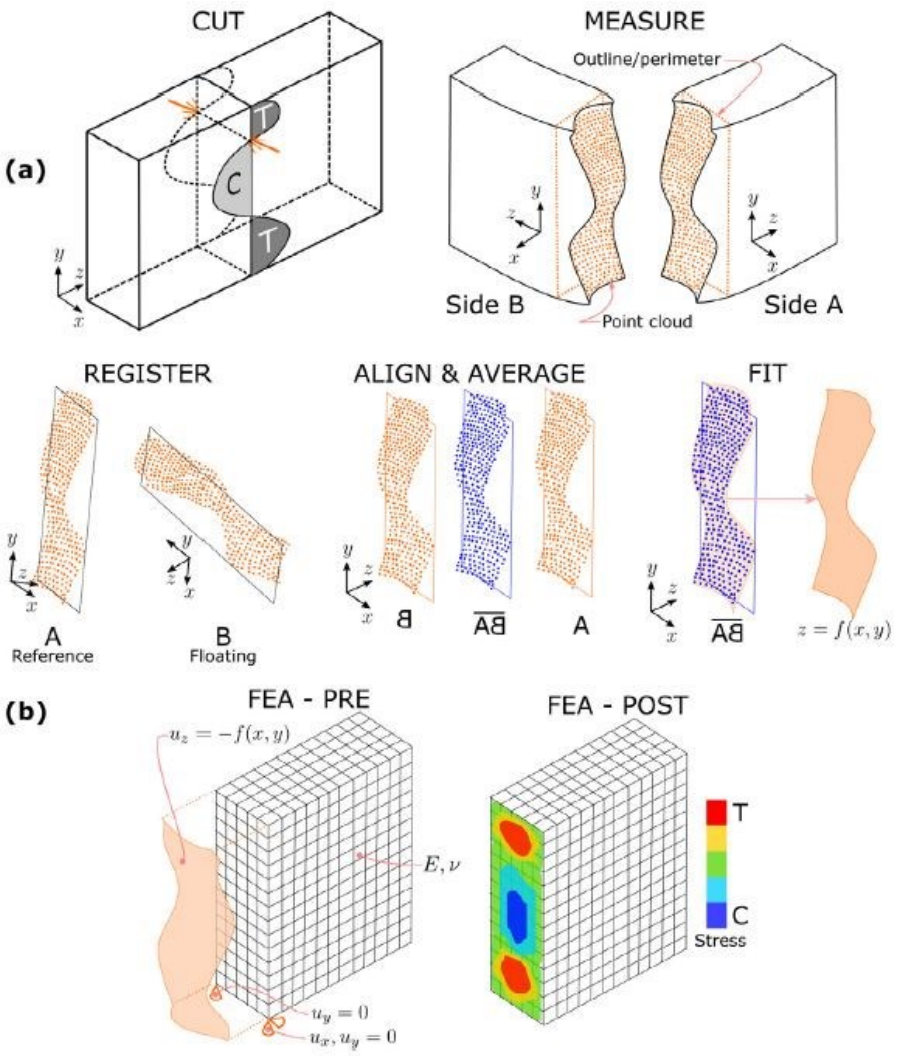

Figure 12. Schematic representation of the steps required for the contour method [16].

The cutting plane must be constrained to prevent movement while the residual stresses relax during the cutting process. Therefore, clamping is necessary on both sides of the cutting plane. The cutting process is a delicate step in the contour method, and clamping is crucial for success. The specimen should be well-constrained, with clamping occurring as close to the cutting plane as possible, to minimize errors in the final results. However, it is important to avoid introducing additional stresses by over-constraining the component. Figure 13 provides an example of this procedure.

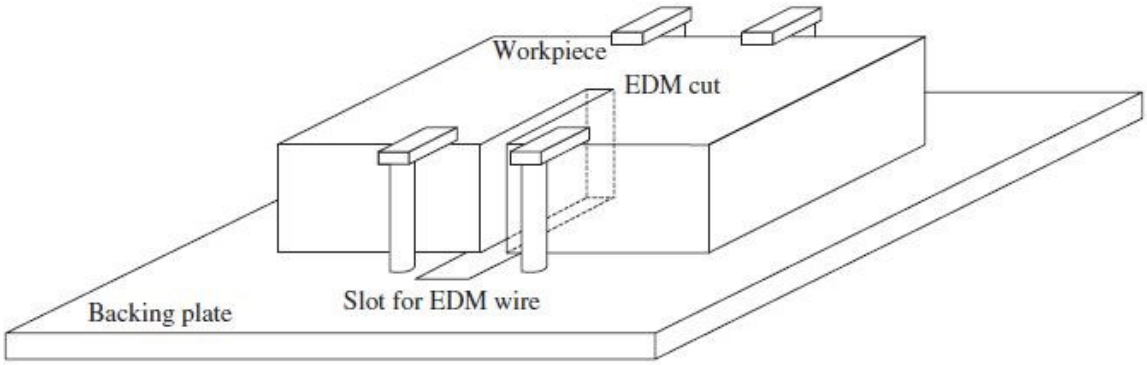

Figure 13. Illustration of the clamping procedure in the contour method [14].

To ensure the proper application of the contour method, the cutting process must produce a straight cut along a plane with low roughness on the cut surfaces. Additionally, the cut thickness (kerf) must be kept to a minimum, and no additional material should be removed from an already cut surface. Finally, the cutting process should not create plasticization or introduce residual stresses. Therefore, the most suitable technique for measuring residual stresses using the contour method is wire-EDM.

Wire-EDM is a thermal process that is suitable for processing conducting materials. It is based on a series of electrical, controlled, non-stationary discharges that are triggered between the tool electrode and the workpiece electrode, causing erosion on the latter. The electro-erosive process generates millions of electrical discharges that locally provide the heat necessary for the formation of small craters on the affected surface. The machining process involves connecting the workpiece and wire tool to the poles of an electric generator. Throughout the process, a small gap is maintained between the two electrodes. The wire unwinds via a pulley, passes through the workpiece, and rewinds on a second pulley. As the wire unwinds, cutting is done by discharges that are created at the front of the wire along

the feed direction. The workpiece and wire electrodes are immersed in a dielectric fluid that insulates them and ionizes easily, allowing for electrical discharges to occur at set intervals. This process enables the processing of conductive materials, regardless of their hardness. Compared with its conventional use, the use of wire EDM in the contour method is modified to perform a single cut with finishing process parameters. Finally, for a proper cutting process for contour method application, it is necessary to: clamp the component symmetrically and as close as possible to the cutting plane, wait for thermal equilibrium between the component and the dielectric tank (deionized water), make a single straight cut along the thickness of the component using finishing process parameters, remove the two cut parts from the machine while maintaining their integrity, and rinse to remove any debris adhering to the surfaces.

After cutting, the newly formed surfaces deform due to the relaxation of residual stresses. These surfaces must then be measured. The results obtained by the contour method depend on the accuracy with which the deviation from flatness of the cut surfaces can be measured. Typically, the contours of cut surfaces have a peak-to-valley distance of 10 μm to 150 μm, depending on the amount of residual stress originally present and the stiffness of the analyzed material. Therefore, an accurate and precise measurement technique is required for such surface height ranges. Surfaces are typically measured using coordinate measuring machines (CMMs) that utilize a probe to directly measure the coordinates of points on the component's surface. However, CMMs can be impractical for large components as they require several hours to acquire profiles. An alternative widely used technique is laser triangulation, which employs a laser diode to illuminate the surface area to be measured with visible light. The optical sensor reflects, acquires, and processes light to pinpoint the location of the scattering, allowing for the calculation of the distance between the sensor and the component surface. This technique is faster than CMM, but depending on the size of the component, it may also take several minutes to complete the measurement.

Therefore, there is a need to expedite this step of the contour method without sacrificing the ultimate accuracy of the residual stress measurement. To address this need, this thesis work will utilize a high-speed 3D imaging technique.

After acquiring the cut surfaces, they undergo a processing step, which will be explained in detail in the next chapter. Finally, a static FE analysis is conducted to obtain the residual stresses normal to the cutting plane.

1.4 Incremental Hole Drilling

As previously mentioned, hole drilling is a commonly used method for measuring surface and subsurface residual stresses [12]. This technique is standardized by ASTM E837-20 [17]. The damage caused to the specimen is minimal, usually consisting of a small hole that can be repaired or tolerated.

To determine surface strains as a result of drilling, rosettes, usually rectangular with three grids at 45 degrees to each other, or equiangular rosettes with three grids at 120 degrees to each other, are used to identify the three stress components in the plane σ_x, σ_y, and τ_{xy}. Figure 14 displays several examples of rosettes. Type A rosettes are intended for general use, while type B rosettes are suitable for making measurements near obstacles. However, the three strain gauges on the same side of type B rosettes can increase errors due to hole eccentricity. Type C rosettes are used for measuring very low stress values and for measurements on materials with low thermal conductivity, such as plastics.

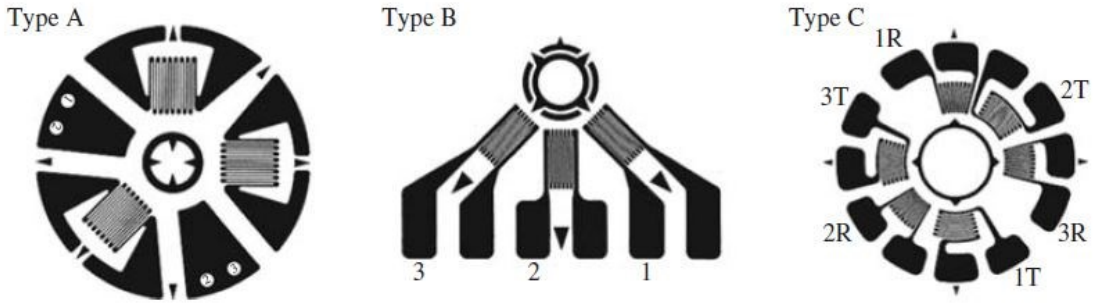

Figure 14. Standard strain gauge rosettes used for hole drilling measurements [17].

The main parameters for selecting the strain gage rosette are:

- *Nominal hole diameter*: typically $D_0 = 0.4D$, where D_0 is the hole diameter and D is the mean gage diameter of the rosette.
- *Hole depth*: The maximum hole depth zh_{max} is a function of the type of rosette used and the mean gage diameter. It is $0.28D$ for type A and B rosettes and $0.4D$ for type C rosettes.
- *Depth of Measured Stress Data*: The maximum depth at which residual stresses can be evaluated is a function of the rosette type and its mean gage diameter. This depth is less than zh_{max} and varies between $0.2D$ and $0.25D$ for type A and B rosettes and $0.3D$ and $0.35D$ for type C rosettes.
- *Specimen thickness*: A minimum specimen thickness of $1.2D$ is required

because drilling thinner specimens will cause significant specimen bending.

- *Distance from an edge*: The proximity of an edge to the hole causes a change in material stiffness and thus greater uncertainties in residual stress calculations. The standard requires that the rosette be attached to the surface of the part so that its center is at least $1.5D$ from the nearest edge.

Once the rosette is installed, the hole drilling machine is positioned so that the drill axis is aligned with the center of the rosette. For more details on the practical implementation of the hole drilling technique, see ASTM E837-20 [17].

Hole drilling can measure both uniform and nonuniform residual stresses along the depth of the hole. In both cases, the hole is drilled in small increments, typically 20 in the case of nonuniform stresses along the thickness. Hence the name incremental hole drilling (IHD). Figure 15 shows how residual stresses that vary along the thickness are evaluated using the hole-drilling technique.

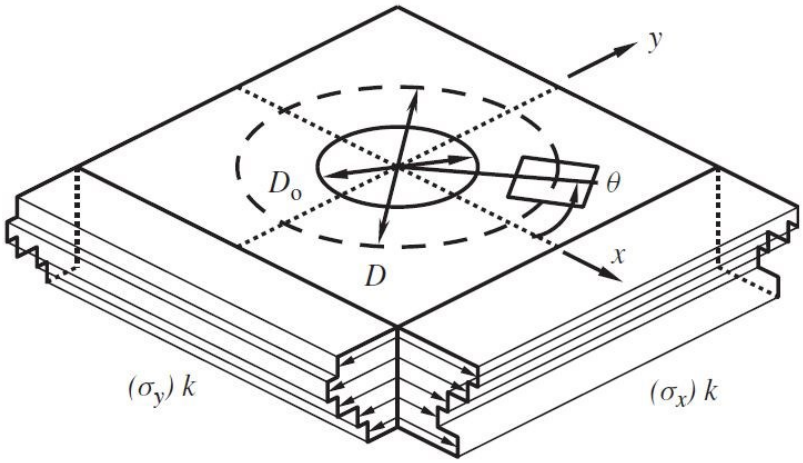

Figure 15. Stepwise variation of residual stresses along drilling depth [17].

In general, the relationship between measured strains and residual stresses is integral, usually a first order Volterra equation:

$$d(h) = \int_{h_0}^{h} g(H,h)\sigma(H)dH \tag{8}$$

where $d(h)$ are the measured strains, $\sigma(H)$ are the stresses originally present at depths H, the initial depth h_0 is typically zero, and the kernel function $g(H,h)$ describes the strain sensitivity to a stress at depth H within the material removed at

depth h. Therefore, an elastic inverse solution is needed to calculate the stress field. The integral method is the most commonly used calculation method for achieving this and is also included in the standard [17]. However, this method is highly sensitive to measurement errors for two reasons. Firstly, the deformation response at the surface, where the rosette is placed, becomes progressively smaller as the hole becomes deeper. Secondly, the inverse problem is numerically ill-conditioned, meaning that small errors in the measured strains can result in significant errors in the calculated residual stresses. Additionally, strains are typically measured at different depths than those at which residual stresses are then calculated. As a result, it is common practice to fit strain measurements using polynomials or splines to derive strains at the appropriate depths for stress calculations using the integral method. It is important to note that the choice of fitting parameters can significantly impact the final measurement output. Therefore, part of this thesis work will be devoted to develop a method to estimate the uncertainty resulting from the strain fit.

Chapter 2. Residual stress characterization of advanced multi-materials joints

This chapter illustrates the adoption of the contour method to analyze various advanced multi-material joints. The technique is used to obtain, in a single measurement, a two-dimensional map of the residual stresses in the direction perpendicular to a plane. This method enables investigation of the residual stress field in a reliable way, without errors related to microstructural changes, such as those present in welds, or errors related to the presence of complex microstructures, such as those in materials made by additive manufacturing.

The first section utilizes the contour method to analyze the longitudinal residual stress field in three different thin dissimilar laser welded joints. These joints consist of Ti6Al4V and Inconel 625, joined by pure Vanadium and a different steel insert for each joint, namely SAF 2507, AISI 316L and AISI 304. The purpose is to identify the joint with the lowest harmful tensile residual stresses.

The second section focused on the mechanical fatigue behavior of one type of the three above joints, built using the AISI 304 insert. However, a general and comprehensive approach was proposed. This consisted of first using surface non-destructive X-ray diffraction and then using the contour method with asymmetric subsequent cuts to obtain information on the entire residual stress field of the complex dissimilar joint. The mechanical quality of the dissimilar joints was evaluated by studying the fatigue behavior, residual stress field and fracture modes, emphasizing the intrinsic correlation of all the information collected.

In the last section the contour method was employed to assess the residual stress field in innovative continuous functionally graded materials, produced using Powder Bed Fusion-Laser Beam process, where the continuous variation in composition is within a single layer. Functionally graded structures of AISI 316L and 18Ni Maraging 300 were analyzed. The study also examined the effect of heat treatment, essential for improving the properties of the maraging steel, on residual stresses. Finally, the influence of utilizing material-differentiated process parameters was investigated.

2.1 Residual stress measurement on Titanium Grade 5 - Inconel 625 thin dissimilar welded joints by Contour Method

2.1.1 Introduction

The accuracy of the contour method results relies on the correct application of all the technique steps; therefore, several studies were carried on to improve the results of the contour method. Firstly, it is important to avoid or correct errors and artifacts during cutting [18–20], and use the best clamping arrangement as well [14,21]. Moreover, cutting-induced plasticity was studied and mitigated proposing "embedded" and "double-embedded" approaches [22–24]. Data processing was enhanced and criteria for determining optimal smoothing parameters were established in order to give better near-surface results [15,25–27]. Therefore, as shown by Toparli et al., the contour method can be applied successfully to thin samples, down to 2-mm-thick, although uncertainty in measurements is higher than for thicker samples [28]. Conventionally, surface profiles are measured using a coordinate measurement machine (CMM) or point-wise optical systems like laser scanning [13,25,29,30]. As outlined in [29], CMM is relatively slow and unsuited to measuring large components, thus using a full-field optical technique would allow for a reduction of measurement time.

The contour method has found broad engineering applications over time [31–34], owing also to its other various advantages like being insensitive to microstructural changes, and being able to capture steep stress gradients, especially in welds [14,25,32]. In spite of the great interest on these joints [35] only very few works investigated residual stresses of dissimilar welds and most of them concerned Al-to-Al joints. Prime et al. validated the ability of the contour method to measure fairly low magnitude residual stresses in a thick dissimilar aluminum friction stir weld [36]. Jafari et al. studied the influence on residual stresses of adding SiO2 nanoparticles in a 5-mm-thick dissimilar aluminum friction stir weld [37]. Xie et al. measured residual stresses in dissimilar titanium linear friction welded joints [38] and Zhang et al. applied the contour method to friction stir welded aluminum and copper plates [39]. No research work has been carried out on measuring residual stress in Ti-to-Ni dissimilar joints using the contour method [40–42].

This study aimed to measure residual stresses in 2-mm-thick laser-welded Ti-6Al-4V and Inconel 625 plates with intermediate inserts of Vanadium and steel using the contour method. In this study, three joints with different steel inserts were analyzed and the contour acquisition of the cut surfaces was carried out using fringe

projection, a full-field optical technique [43,44]. Finally, the results were compared to X-ray diffraction (XRD) measurements.

2.1.2 Materials and welding conditions

The nominal chemical compositions of the Ti-6Al-4V base metal, the Inconel 625 base metal and the Vanadium insert are given in Table 1, while the steel inserts were analyzed by X-Ray Fluorescence (XRF), measured chemical compositions are listed in Table 2. Nominal mechanical properties of the three different steel inserts are given in Table 3.

Table 1. Nominal chemical compositions (wt%) of Ti-6Al-4V, Inconel 625 and Vanadium.

Ti-6Al-4V											
	V	Al	Fe	O	N	H	Ti				
Min	3.5	5.5	0	0	0	0	Balance				
Max	4.5	6.8	0.3	0.2	0.05	0.015					
Inconel 625											
	Ni	Cr	Mo	Fe	Nb	Co	Mn	Si	Ti	Al	C
Min	58	20.0	8.0		3.15						
Max		23.0	10.0	5.0	4.15	1.0	0.50	0.50	0.40	0.40	0.10
Vanadium											
	V	Others									
Min	99.9	Balance									
Max											

Table 2. Chemical compositions (wt%) of SAF 2507, AISI 304, AISI 316L measured by XRF.

SAF 2507						
	Fe	Cr	Ni	Mo	Mn	Cu
Concentration	61.73	23.18	7.36	4.78	2.41	0.55
Error	±0.24%	±0.33%	±0.83%	±0.69%	±0.74%	±4.7%
AISI 304						
	Fe	Cr	Ni	Cu	Mo	Ti
Concentration	71.13	19.96	7.82	0.7	0.27	0.12
Error	±0.18%	±0.27%	±0.66%	±2.79%	±2.36%	±2.9%
AISI 316L						
	Fe	Cr	Ni	Mn	Mo	Ti
Concentration	64.2	18.54	10.94	3.39	2.18	0.74
Error	±0.19%	±0.3%	±0.58%	±0.61%	±0.88%	±2.05%

Table 3. Yield strength and ultimate tensile strength of the three steel inserts [45,46].

	SAF 2507	**AISI 304**	**AISI 316L**
Yield strength (MPa)	>550	205	290
Ultimate tensile strength (MPa)	800-1000	515	580

An IPG Ytterbium Fiber Laser System (YLS-4000-CT), available at ENEA Casaccia, with a maximum output power of 4200 W at 1070 nm was used in the welding process. Laser power was transported to the piece through a 100 μm diameter optical fiber and focused by a 250 mm focal length lens, the divergence was 50 mrad while the beam product was 3 mm mrad. The welding head was equipped with a wobbling module that impresses an oscillatory motion to the focal spot by using two galvanometric mirrors. Those can be driven up to a frequency of 1 kHz leading to a maximum displacement of the laser beam of 4 mm. Forward movement is driven by a numerically controlled cartesian positioner (builder: Pegaso Sistemi s.r.l.) with x, y and z strokes equal to 550 mm, 550 mm and 300 mm, respectively. The welding set-up is shown in Figure 16.

Three butt-welded specimens with three different steel inserts were prepared. The Ti-6Al-4V and Inconel 625 sheets were 100 mm × 200 mm × 2 mm, the Vanadium insert was 10 mm × 200 mm × 2 mm, and the steel inserts were all 15 mm × 200 mm × 2 mm in dimensions. Figure 17 shows a schematic drawing of the welded plates while Table 4 reports the respective welding schemes. The welding sequence of the three samples is given in Table 5. Weldings were performed at 1750 W and with a nominal diameter of the laser spot of 250 μm to obtain full penetration in a single pass without filler material. Different welding speeds were used on the three interfaces: 40 mm/s at the Inconel 625/steel interface; 30 mm/s at the steel/Vanadium interface, with the wobbling of the laser spot set to a frequency of 500 Hz and an amplitude of 0.5 mm; 45 mm/s at the Vanadium/Ti-6Al-4V interface. Argon was applied to suppress plasma and as trailing and backing shielding gas, respectively with flow rates of 10 l/min, 20 l/min, and 10 l/min, as can be seen in Figure 16.

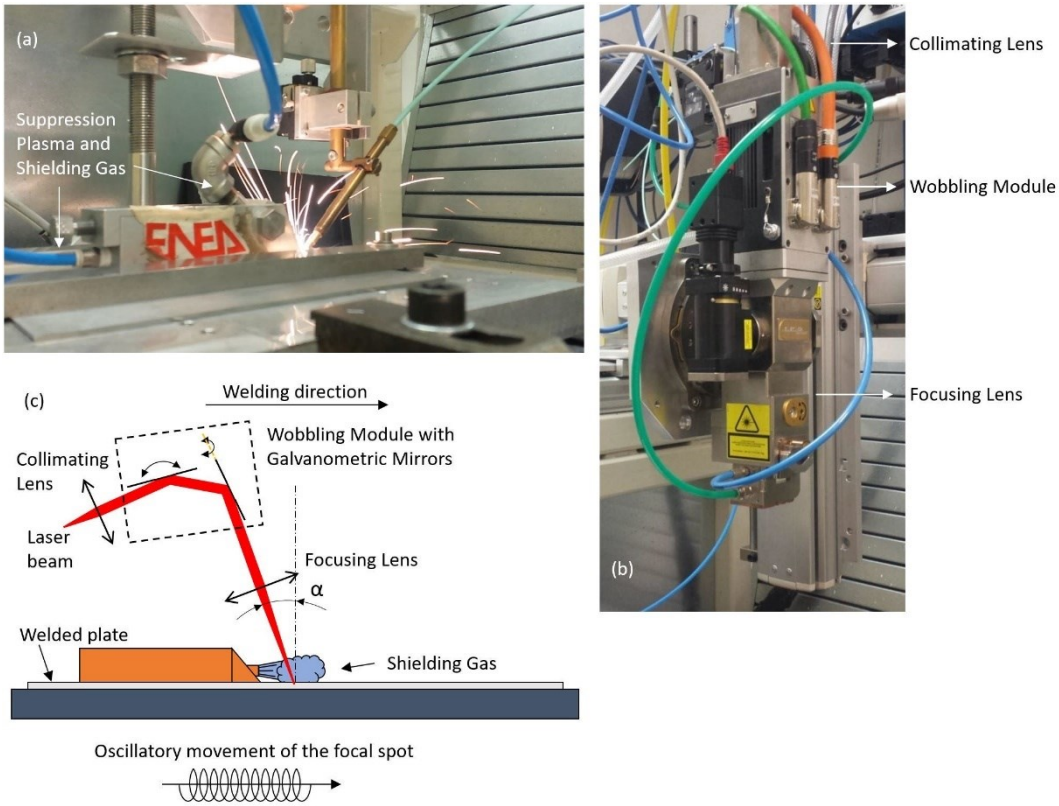

Figure 16. (a) Welding set-up; (b) welding head; (c) working principle diagram.

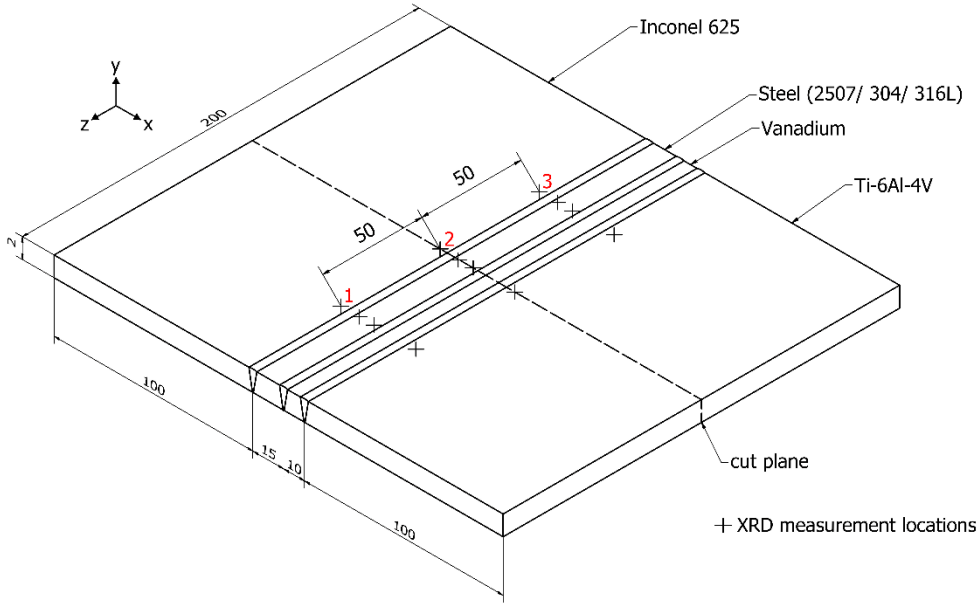

Figure 17. Schematic illustration of the welded plates. The cut plane used for the contour method is indicated as well as the locations for the XRD.

Table 4. Naming and welding schemes of the three samples.

ID plate	Welding scheme			
A	Inconel 625	SAF 2507	Vanadium	Ti-6Al-4V
B	Inconel 625	AISI 316L	Vanadium	Ti-6Al-4V
C	Inconel 625	AISI 304	Vanadium	Ti-6Al-4V

Table 5. Welding sequence of the three samples.

ID plate	Welding sequence						
A	Ti-6Al-4V	→	Vanadium	→	SAF 2507	→	Inconel 625
B	Ti-6Al-4V	→	Vanadium	→	AISI 316L	→	Inconel 625
C	Ti-6Al-4V	→	Vanadium	→	AISI 304	→	Inconel 625

2.1.3 Contour method set-up and procedure

The contour method was carried out following four main steps: specimen cutting by EDM, contour measurement of the two cut surfaces by fringe projection, data processing and finite element analysis [13,14].

The cut was performed with an Agiecut Classic 2S wire EDM machine. Every specimen was positioned in the EDM tank, submerged with deionized water together with the fixture, and, after reaching thermal equilibrium it was securely and symmetrically clamped. The cut plane (Figure 17) was taken transverse to the welding joint at the centerline of the plates. A 250 μm diameter brass wire and "skim" cut settings were used to minimize any recast layer and cutting-induced stresses [13,25].

The two halves of each sample were kept in a temperature-controlled laboratory for several hours to reach thermal equilibrium with the environment before surface profile measurements.

Usually, a CMM is used to measure the contours after the cut [13,14,29], furthermore non-contact optical scanners and confocal laser profilometers have been used [15,25,28,36,47]. In the present study, the measurement of the cut surfaces was performed using fringe projection.

The fringe projection method extracts the 3D surface shape of an object using the information encoded into a deformed fringe pattern captured by an image acquisition sensor [43]. A sequence of sinusoidal fringe patterns are directly projected on the specimen and analysis of the images captured by the camera is carried out. The result is in the form of the phase recorded at each pixel $\phi(i, j)$, which

is scaled into the 3D (x,y,z) coordinates of the sample surface [44,48]. The success of the fringe projection technique relies on the generation of high-quality fringe patterns. Having an 8 bit system which can project grayscale from 0 to 255, the computer generated fringe pattern can be described as:

$$I(i,j) = 255/2\left[1 + \cos\left(\frac{2\pi j}{P(i,j)} + \delta\right)\right] \quad (9)$$

Where (i,j) is the pixel index, $I(i,j)$ is the intensity of the projected fringe pattern, $P(i,j)$ is the fringe pitch, δ is the phase shift and the pattern varies sinusoidally along j direction.

Phase shifting can be used to extract the local pitch $P(i,j)$:

$$I_1(i,j) = 255/2\left[1 + \cos\left(\frac{2\pi j}{P(i,j)} - \frac{2\pi}{3}\right)\right] \quad (10)$$

$$I_2(i,j) = 255/2\left[1 + \cos\left(\frac{2\pi j}{P(i,j)}\right)\right] \quad (11)$$

$$I_3(i,j) = 255/2\left[1 + \cos\left(\frac{2\pi j}{P(i,j)} + \frac{2\pi}{3}\right)\right] \quad (12)$$

Finally, the height of the specimen under measurement $z(i,j)$ can be retrieved by:

$$z(i,j) = f_{cal}\big(P(i,j)\big) \quad (13)$$

Where f_{cal} is a calibration function which takes into account distortion and aberration effects both of the projector and camera lenses, of the triangulation angle between camera and projector, and of the variation of the fringe pitch $P(i,j)$ within the measurement volume.

The fringe projection method's high-speed nature significantly reduces the time required for acquiring cut surface measurements compared to standard CMM measurements.

In this study, a camera with a resolution of 2 MPix (1624 × 1234 pixels), a fringe

projector and a computer were used. The surfaces to be acquired were positioned perpendicular to the camera optical axis. The contour measurement set-up can be seen in Figure 18. A total of roughly 45000 data points for each surface were collected, with a point spacing of about 0.1 mm in both x and y dimensions.

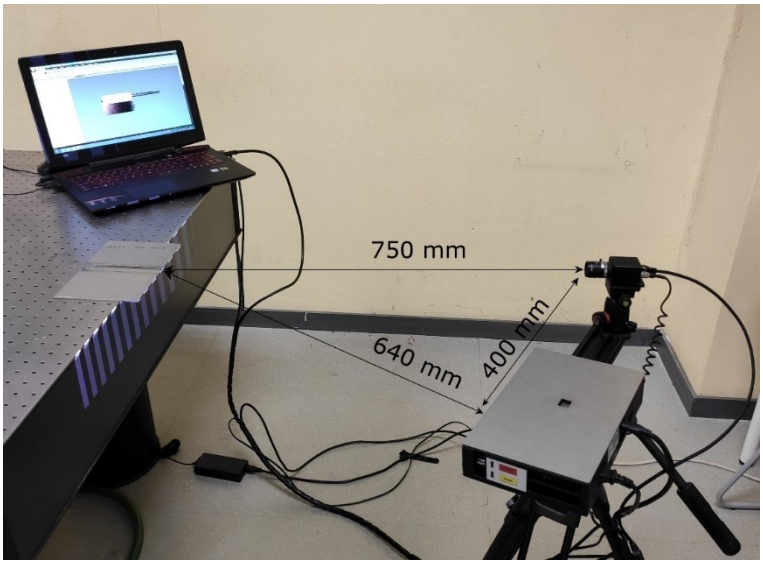

Figure 18. Surface contour measurement using fringe projection.

Each couple of point clouds, obtained from the three specimens, underwent the processing step (Figure 19) :

1. The point cloud from one surface was mirrored across the x-z plane. The data sets were then translated to a common origin.
2. The outliers were removed.
3. The perimeters were derived from the two point clouds by using the Matlab "boundary" function.
4. The data sets were further aligned by utilizing an iterative closest point procedure (ICP) [49].
5. Data near the outline were affected both by cutting effects and by optical contour measurements, thus points up to 0.2 mm below the perimeter were discarded.
6. The two sets of measurements were interpolated onto a common regular grid and averaged to minimize anti-symmetric errors and shear effects [18].
7. The averaged data were smoothed using not only bivariate cubic splines but quadratic as well, in order to get better near-surface results [26,28].
8. The fitting splines were selected by minimizing the uncertainty in the

calculated stresses. The uncertainty was estimated following the procedure illustrated by Prime et al. in [25].

9. The splines were then linearly extrapolated up to the perimeter using the Matlab Spline Toolbox.

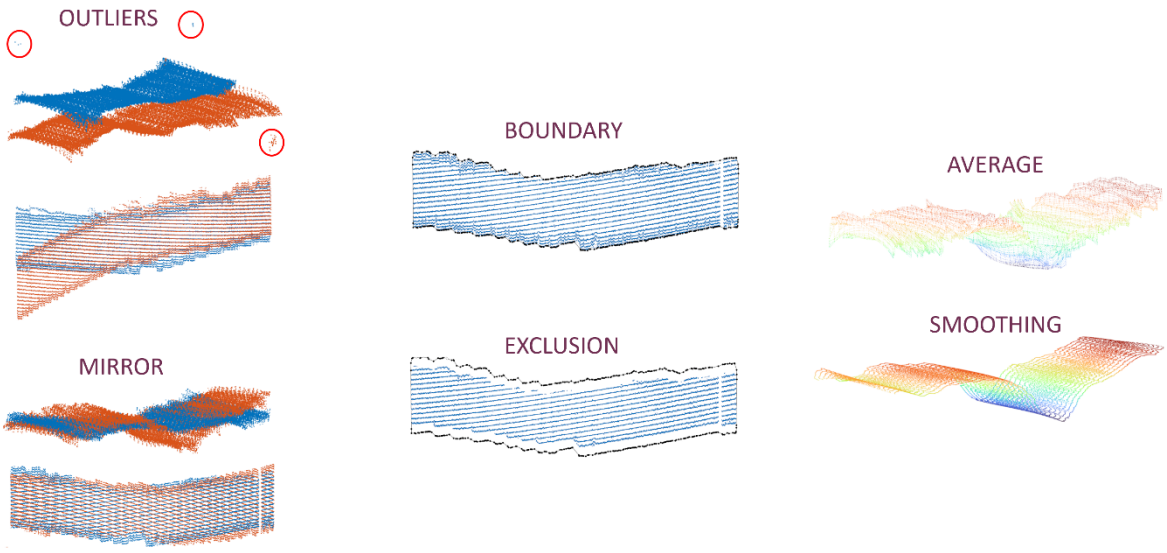

Figure 19. Scheme of the processing step of the contour method.

A three-dimensional elastic finite element (FE) model of a cut part of every sample was implemented with ABAQUS software using the measured perimeters. In the FE models the three welds of every plate were modeled as separation planes of nodes between one material and another, and thus different mechanical properties were applied. This approach is different from that adopted in [36] for a dissimilar aluminum alloy weld where a mean Young's modulus and a mean Poisson's ratio were used. The material mechanical properties are listed in Table 6. The mesh was generated with C3D8R elements having 0.1 mm × 0.1 mm dimensions in the cut plane. The smoothed and averaged contours were applied, with reversed sign, as boundary displacements conditions.

Table 6. Mechanical properties of the materials composing the welded plates [45,46].

	Inconel 625	**Steel**	**Vanadium**	**Ti-6Al-4V**
Young's modulus (GPa)	208	196	120.2	125.5
Poisson's ratio	0.28	0.28	0.36	0.36

2.1.4 X-ray diffraction measurement set-up

Surface residual stress measurements were performed using an Xstress 3000 G3R X-ray diffractometer by Stresstech instrumented with a Cr tube (λ=0.22897 nm) for Inconel 625 and steel inserts, and with a Ti tube (λ=0.274851 nm) for the Ti-6Al-4V plates. The measurements were carried out at the weld toes as near as possible to the weld beads (about 0.5 mm) in three different points for every material, as it can be seen in Figure 17. Both longitudinal and transverse surface residual stresses were measured.

The measurements were performed using the $\sin^2\psi$ method following the UNI EN 15305 standard [50]. The diffracted intensity, the peak width and the position of K-alpha 1 of the diffraction peak were determined by interpolating the peak profile by the Pearson VII function. The measurement parameters are summarized in Table 7.

Table 7. X-ray diffraction measurement parameters.

Material	Tube	Exposure time (s)	No. of Tilts	Tilt angle(°)	Psi oscillation	Collimator diameter (mm)	Voltage (kV)	Current (mA)
Inconel 625	Cr	35	4	±45	±3	1	30	8.0
Steel	Cr	60	4	±45	±0	1	30	8.0
Ti-6Al-4V	Ti	40	4	±40	±0	1	30	7.5

2.1.5 Contour method results

To select the fitting splines, the number of knots was varied along the x direction, from 3 knots (with a spacing of about 75 mm) to 30 knots (with a spacing of about 7.5 mm), and the corresponding FE analyses were conducted. Along the y direction only two and three knots were used for the cubic and quadratic splines respectively, owing to the low thickness of the samples and to avoid overfitting as well. The stress uncertainties were calculated following the procedure developed by Prime et al. [25] as well as the average stress uncertainties over the whole stress maps. The uniform spline knot spacings in x and y directions and the estimated average stress uncertainties for the three welded plates are listed in Table 8. Though higher with respect to analogous results reported for thicker specimens [25,36,51], the minima stress uncertainties calculated are consistent with those indicated by Toparli et al. for a 2 mm thick laser peened Al2024-T351 sample in [28].

The surface profiles of the three welded plates after cubic spline smoothing are shown in Figure 20, Figure 21, and Figure 22. For all the specimens the peak-to-valley difference of the averaged surface contours was about 100 μm.

Table 8. Knot spacing and stress uncertainties for both cubic and quadratic spline order for specimens A, B and C.

A			
Spline order	**Knot spacing *x* (mm)**	**Knot spacing *y* (mm)**	**Average stress uncertainty (MPa)**
Cubic	18.61	2.00	42.61
Quadratic	20.30	1.00	42.69
B			
Spline order	**Knot spacing *x* (mm)**	**Knot spacing *y* (mm)**	**Average stress uncertainty (MPa)**
Cubic	20.35	1.90	28.55
Quadratic	17.22	0.95	47.81
C			
Spline order	**Knot spacing *x* (mm)**	**Knot spacing *y* (mm)**	**Average stress uncertainty (MPa)**
Cubic	18.72	2.10	32.05
Quadratic	17.28	1.05	45.32

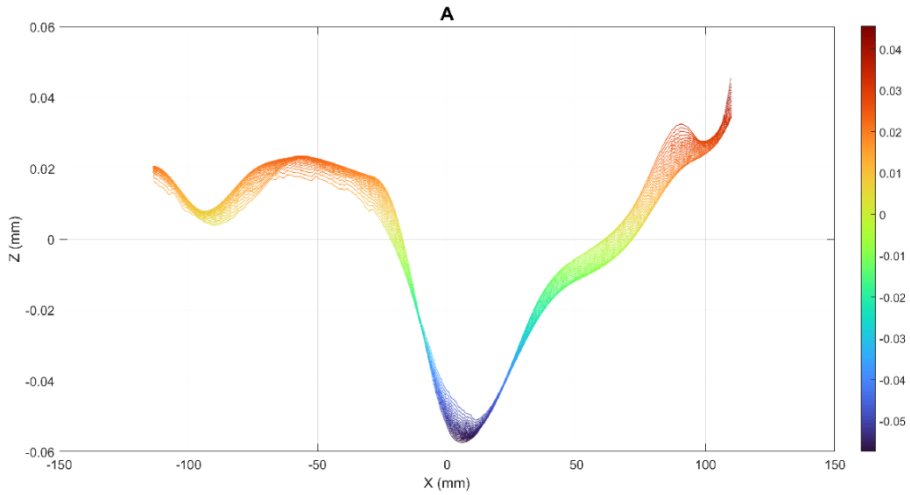

Figure 20. Surface profile of specimen A after cubic spline smoothing.

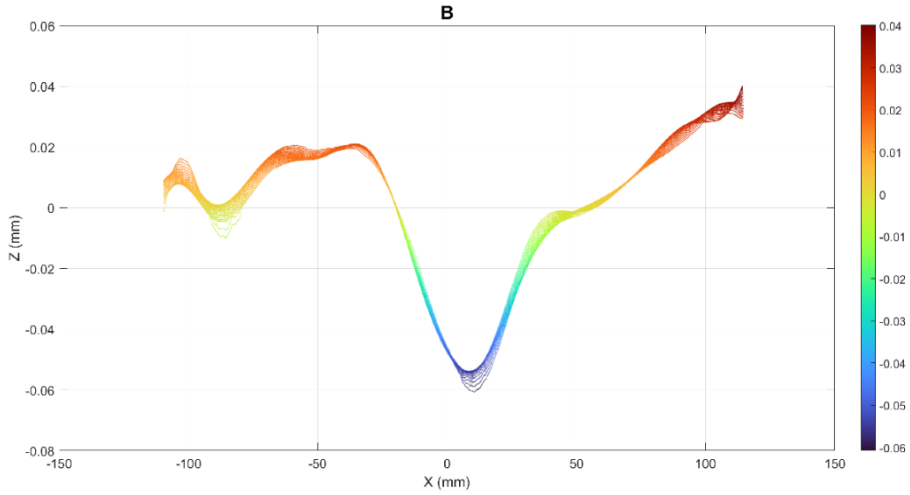

Figure 21. Surface profile of specimen B after cubic spline smoothing.

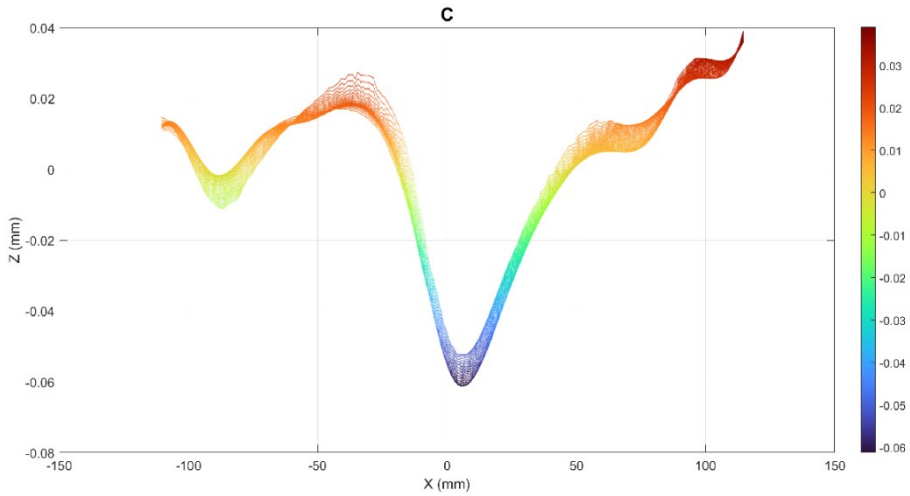

Figure 22. Surface profile of specimen C after cubic spline smoothing.

The contour method measures the stresses normal to the contour cut, therefore longitudinal (z-direction) residual stresses are measured in the present study.

Figure 23 shows the 2D longitudinal residual stress map of sample A with the SAF 2507 insert. Tensile residual stresses are located in the three-welds zone, balanced by compressive residual stresses in the base metals. Higher compressive stresses are localized in the Inconel 625 base material. Moreover, in the Inconel 625 region, surface tensile residual stresses occur due to cold rolling [52]. In the three-weld zone, the maximum tensile longitudinal stress is in the core of the steel insert with a value of more than 400 MPa. Also, at the SAF 2507 / Vanadium weld top-surface, tensile stress varies between 150 MPa and 320 MPa, while at the back slight compression can be found. In the Inconel 625 side of the welding with the steel insert, compressive stresses occur and extend from the joint interface to the base metal.

The 2D longitudinal residual stress maps of samples B and C, respectively with the AISI 316L and the AISI 304 inserts, are shown in Figure 24 and Figure 25. Likewise sample A, both stress maps present a tension zone in the three-welds region, while at the base metals, compression occurs. In the outline region, where the fitting splines were extrapolated, unreasonably high magnitude stresses can be found (e.g. 1144 MPa in Figure 24). These values are due to errors associated with the data extrapolation, therefore should not receive too much attention [26]. Indeed the minima and maxima stress values indicated in Figure 23, Figure 24 and Figure 25 do not include the outline extrapolated region.

Regarding specimen B, on the one hand, a shift of the highest tension zone to the Inconel 625 / AISI 316L weld can be found, with a maximum value of about 600 MPa. On the other hand, the compression region in the Inconel 625 side of the weld with the steel insert is shifted towards the base material rather than being near the welding. Nonetheless, compressive stresses are still present at the surface but not in the core. Furthermore, harmful tensile residual stresses at the top surface of the weld between AISI 316L and Vanadium inserts still exist, ranging from 160 MPa to 380 MPa.

Figure 25 shows that similarly to specimen A, in sample C the highest tensile residual stress zone is in the core of the steel insert near the AISI 304 / Vanadium interface, reaching about 560 MPa.

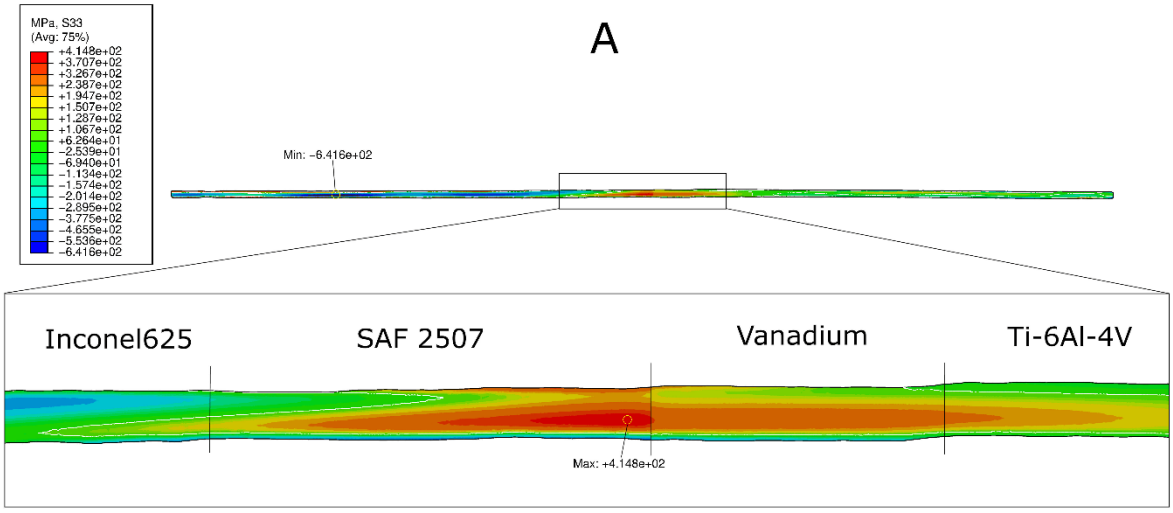

Figure 23. Longitudinal residual stress map of sample A (stresses are in MPa). The white lines indicate the isolines at zero MPa, showing the transition between compressive and tensile areas.

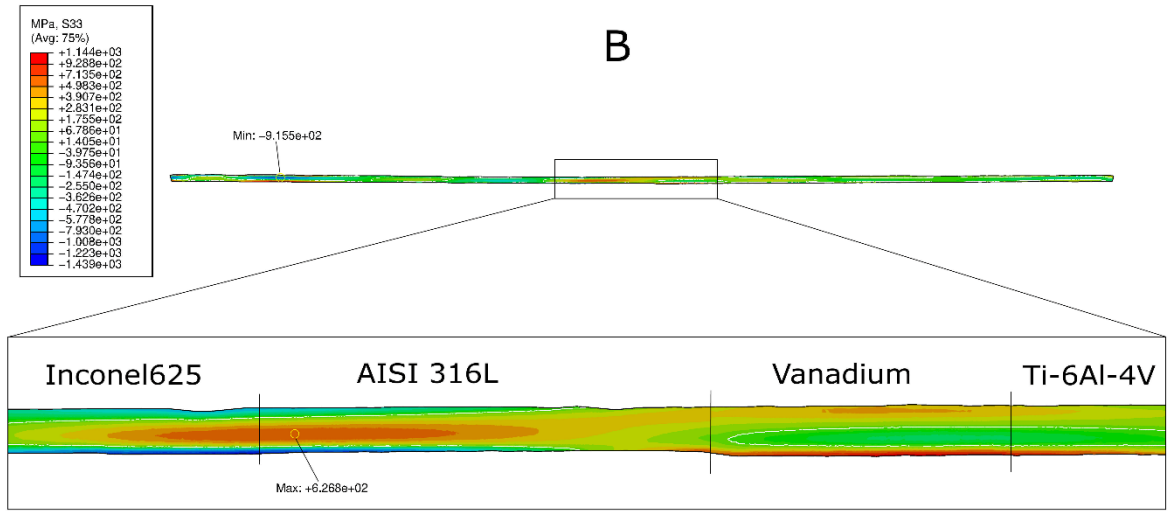

Figure 24. Longitudinal residual stress map of sample B (stresses are in MPa). The white lines indicate the isolines at zero MPa, showing the transition between compressive and tensile areas.

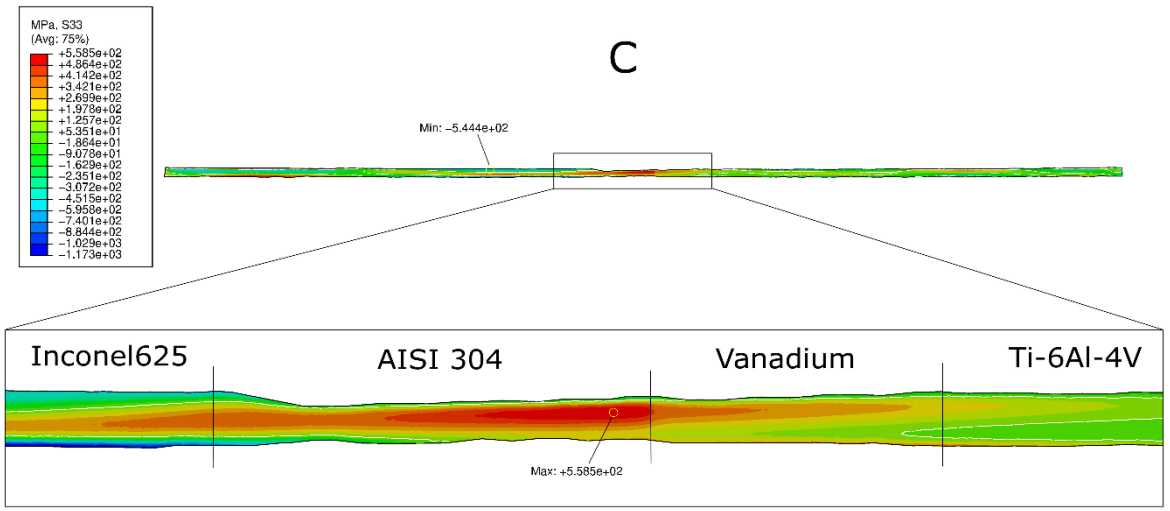

Figure 25. Longitudinal residual stress map of sample C (stresses are in MPa). The white lines indicate the isolines at zero MPa, showing the transition between compressive and tensile areas.

In dissimilar joints, residual stresses, besides the welding process, arise because of different coefficients of thermal expansion (CTE) of the two welded materials [53–55]. When a dissimilar joint cools down, unequal expansion and distortion occur. The material with the greater CTE shrinks more and faster, while the material with the lower CTE tends to shrink less and, together with the parent material, restrains the contraction of the first one. Therefore, once at room temperature, the material with the greater CTE has undergone more constraint to its contraction and thus develops higher tensile residual stresses. Table 9 reports the

CTEs of the materials used in the present study, and also the percentage difference between the CTEs of every welded joint of the three welded plates. The greatest difference always occurs at the steel / Vanadium weld. This is consistent with the results obtained by the contour method, where the highest tensile residual stress zone falls in the steel insert and near the interface with the Vanadium.

Table 9. Coefficient of thermal expansion and the percentage difference between the CTEs of the materials composing the welded plates [45,46].

	Materials						
	Inconel 625	SAF 2507	AISI 316L	AISI 304	Vanadium		Ti-6Al-4V
CTE ($\mu m/m\ K^{-1}$)	12.8	13.5	16.0	17.3	8.3		9.0
	Inconel-SAF2507	Inconel-AISI316L	Inconel-AISI304	SAF2507-Vanadium	AISI316L-Vanadium	AISI304-Vanadium	Vanadium-Ti6Al4V
CTEs %difference	5.47%	25.00%	35.16%	62.65%	92.77%	108.43%	8.43%

2.1.6 X-ray diffraction results

X-ray diffraction measurements were performed at the top surface of the welded plates, prior to contour method cutting, at the locations reported in Figure 17.

Figure 26 shows the measured surface longitudinal residual stresses of the three samples. In the Inconel 625 side of the weld with the steel insert, every specimen is characterized by compressive surface residual stresses, and sample B (with AISI 316L insert) reports the highest compression. The steel side of the joint with the Vanadium turns out to be the region affected by the greatest tensile stresses, in all three samples. The welded plate with the AISI 316L insert shows the lowest surface tensile residual stress, with a mean value of about 380 MPa among the three measurement locations.

The measured surface transverse residual stresses of the three specimens are shown in Figure 27. All welds are characterized by compressive transverse residual stresses. Slight compression can be found in the Titanium side of the joint with the Vanadium and in the steel side of the weld with the Inconel 625, while high compression affects the Inconel side. The only exception is in the steel side of the joint with the Vanadium where low tension occurs in samples B and C.

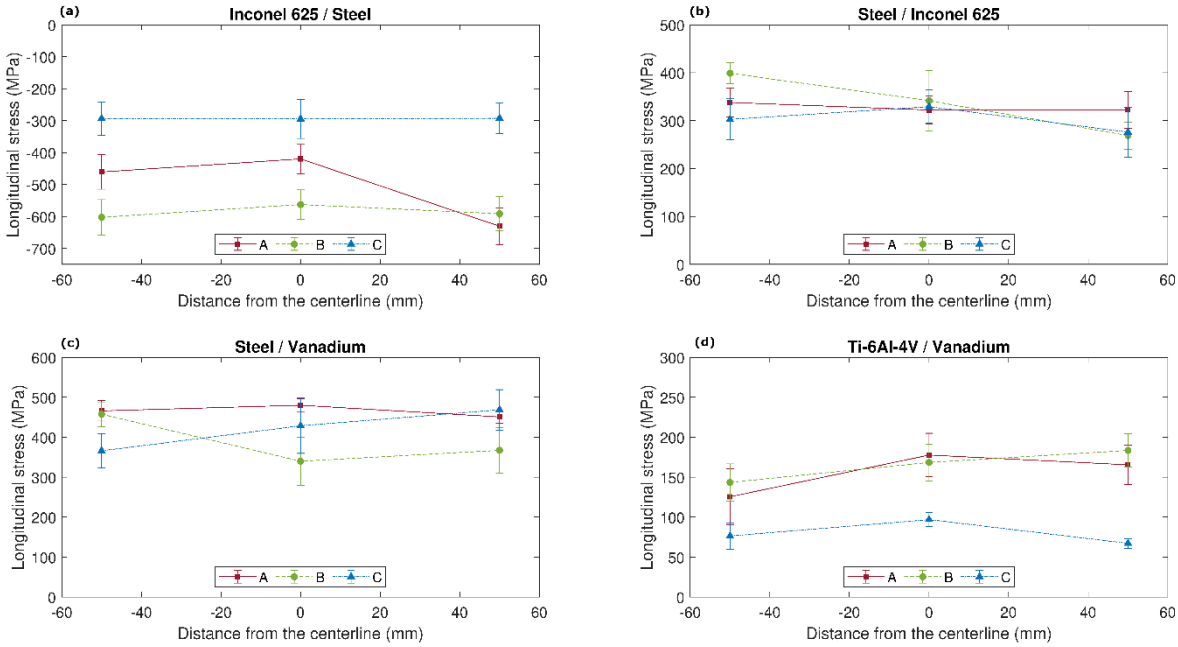

Figure 26. Surface longitudinal residual stresses in the three samples measured by X-ray diffraction.

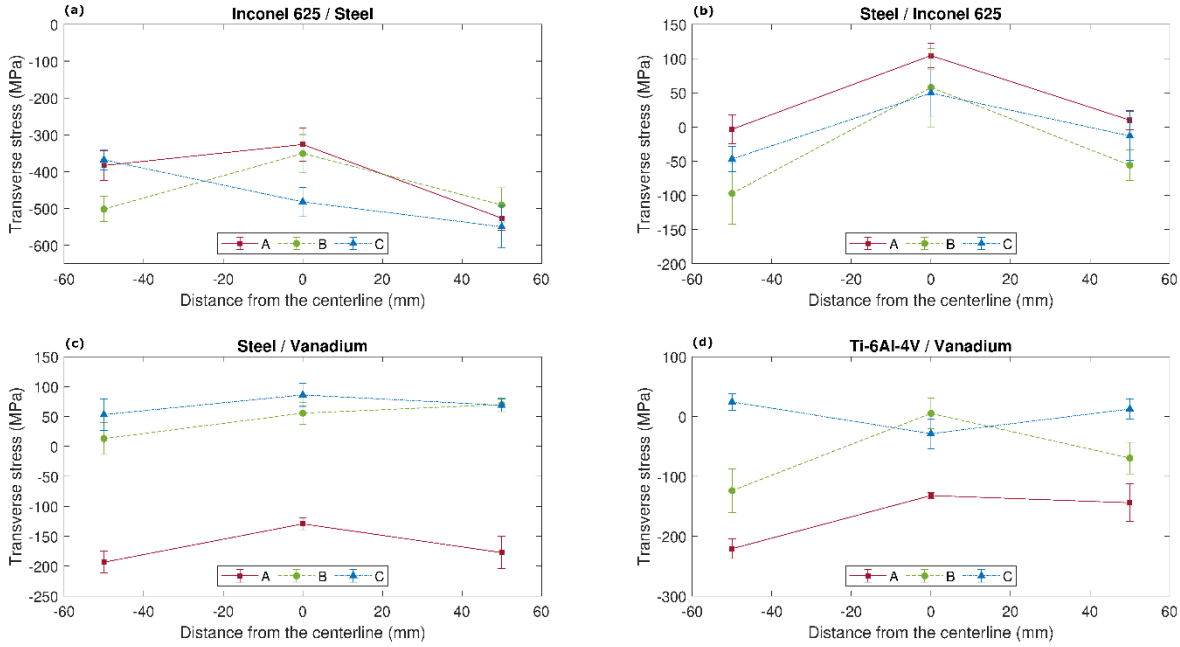

Figure 27. Surface transverse residual stresses in the three samples measured by X-ray diffraction.

2.1.7 Comparison of contour method and X-ray diffraction results

In-depth profiles of the residual stresses measured by contour method, both with cubic and quadratic spline fitting, were derived from the stress maps. The

profiles were taken at about 0.5 mm from the joint interfaces, likewise the previous XRD measurements.

Figure 28, Figure 29 and Figure 30 show the through-thickness residual stress distribution, along with mean values of the surface measurements by XRD. Cubic and quadratic fitting stress results have the same general trend. However, near-surface results are not stable, particularly for sample B, where a different spline order leads to high variations in the calculated stresses.

XRD measurements are consistent with contour method results, especially for specimen B (Figure 29). Furthermore, even though discrepancies in surface results can be seen, not considering the extrapolated region but 0.2 mm in-depth contour method results, the two techniques agree very well. The only exception is at the steel side of the weld with Inconel 625, where the contour method shows compressive stresses, while XRD indicates a tension region. This is probably owing to too large knot spacing in spline fitting, resulting in the inability of the contour method to capture a sudden change from compressive to tensile stresses within the space of 1 mm, and especially because of errors in the outline extrapolated region where the contour method is less precise.

Harmful surface tensile residual stresses occur in all the samples in the steel side of the weld with the Vanadium insert. As stated above, this is also due to the difference in CTEs. Therefore, considering the results obtained both by the contour method and the X-ray diffraction method, among the three dissimilar joints, the welding scheme that produces the lowest tensile residual stresses is the one with the AISI 316L insert. Although the lowest difference in CTEs occurs in the scheme with SAF 2507, it is not the plate with the lowest residual stresses, thus other material properties should be considered. This can be explained in accordance with the work of Lee and Chang, where they studied the influence of yield strength on welding residual stresses in similar and dissimilar weldments [56]. They found that longitudinal residual stresses increased with increasing yield strength in similar weldments. While, in the case of dissimilar welds, the maximum longitudinal residual stresses occurred in the material with the greater yield strength, and it increased with increasing the difference between yield strengths of the two welded materials. In fact, as reported in Table 3, SAF 2507 has the highest yield strength among the three steel inserts, which increases the development of nonuniform thermal strains when the welded joint cools down leading eventually to higher residual stresses [57].

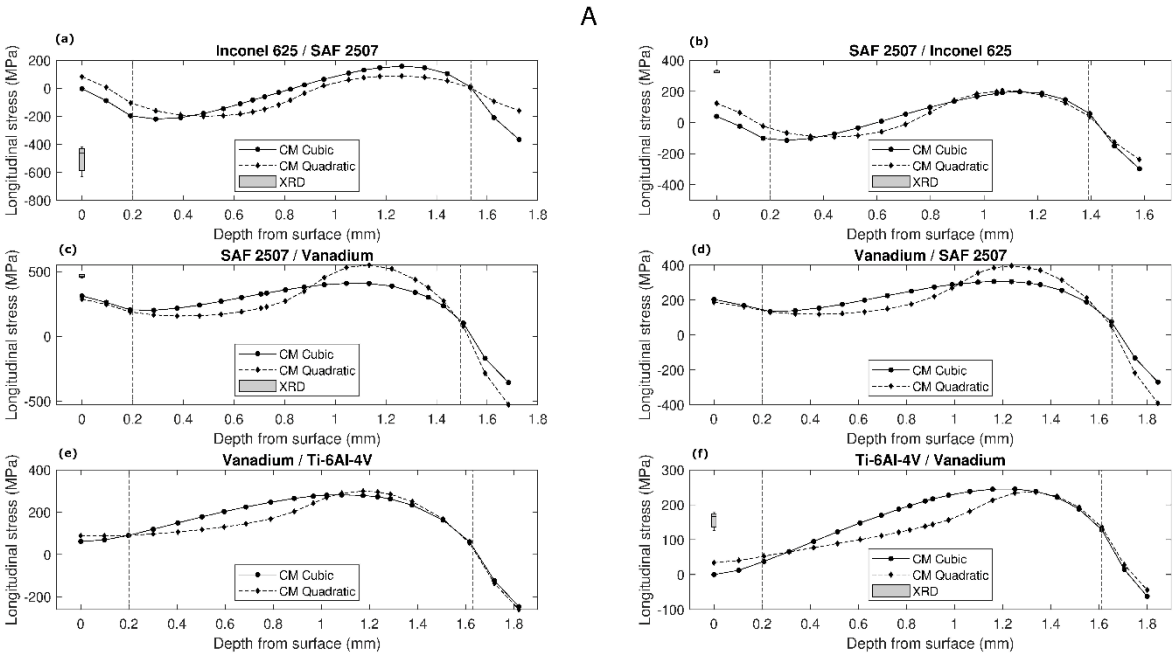

Figure 28. Comparison of in-depth residual stress results obtained by the contour method (CM), with both cubic and quadratic spline fitting, and surface residual stresses measured by X-ray diffraction (XRD), for sample A. Dashed vertical lines indicate the extrapolated regions.

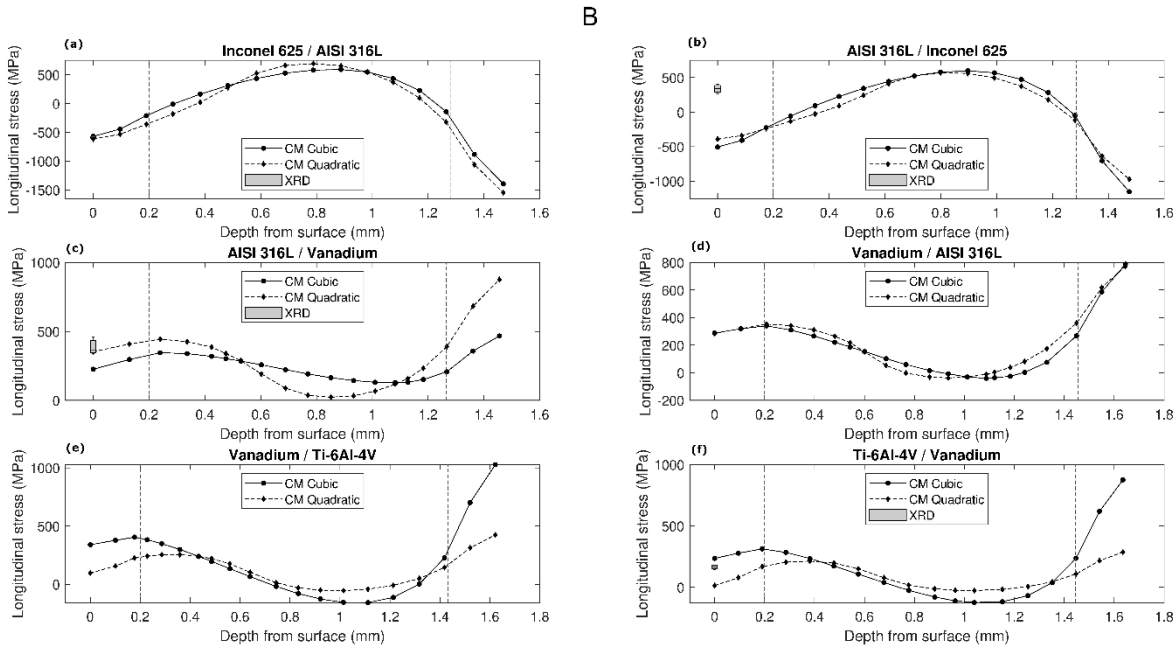

Figure 29. Comparison of in-depth residual stress results obtained by the contour method (CM), with both cubic and quadratic spline fitting, and surface residual stresses measured by X-ray diffraction (XRD), for sample B. Dashed vertical lines indicate the extrapolated regions.

C

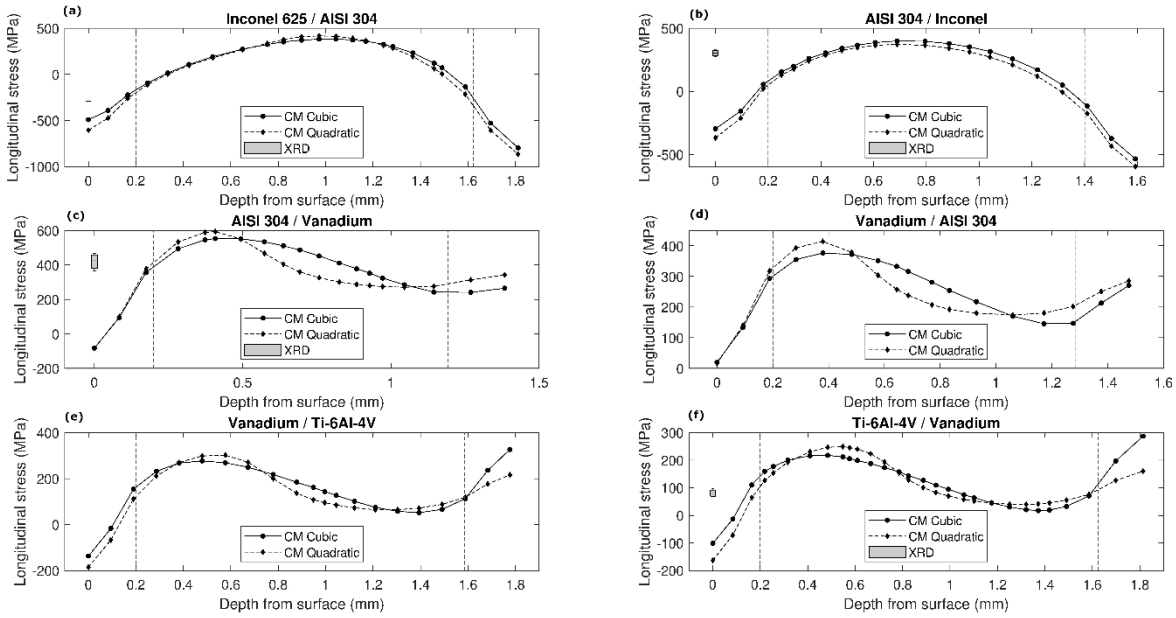

Figure 30. Comparison of in-depth residual stress results obtained by the contour method (CM), with both cubic and quadratic spline fitting, and surface residual stresses measured by X-ray diffraction (XRD), for sample C. Dashed vertical lines indicate the extrapolated regions.

2.1.8 Conclusions

In this piece of study, longitudinal residual stresses in 2 mm-thick laser-welded Ti-6Al-4V and Inconel 625 plates with intermediate steel and Vanadium inserts were measured by the contour method and by the X-ray diffraction. Three joints, realized with different steel inserts and with the same process parameters, were analyzed. During the implementation of the contour method, the profiles of the cut surfaces were acquired by fringe projection. Moreover, to deal with the configuration of the three dissimilar joints, each of which was composed by four different materials, the FE models were built up modeling the welds as separation planes of nodes between one material and another, and thus different mechanical properties were assigned.

The stress maps obtained by the contour method revealed that all the samples were characterized by tensile stresses located in the three-welds zone, balanced by compressive residual stresses in the base metals. Furthermore, for every joint, the highest tensile residual stress zone occurred in the steel insert, while compression was found in the Inconel 625 side of the welding with the steel. Notably, harmful surface tensile stresses developed at the welds between steel and Vanadium. This was due to the different CTEs of the two materials, in addition to the welding process itself.

XRD measurements were carried out at the weld toes at about 0.5 mm from the weld beads. The results were consistent with the contour method measurements. The sole exception was at the steel side of the weld with the Inconel 625, where the contour method was unable to detect a sudden change from compressive to tensile stresses in a short length, owing to low knot density in spline fitting.

Lastly, considering both the contour method and the X-ray diffraction results, the welding solution where the lowest harmful surface tensile residual stresses occurred was the dissimilar joint made with the AISI 316L insert.

2.2 Comprehensive approach for the evaluation of the mechanical behavior of dissimilar welded joints

2.2.1 Introduction

One of the extremely interesting research topics, resulting from the continuous and unstoppable industrial progress, is the development of advanced technologies to weld dissimilar materials. Indeed, the development of application-oriented engineering solutions which combine the unique properties of different materials has become increasingly compelling [58]. These solutions arise from the need to enhance design flexibility and product functionality, and respond as well to the demand for cost savings, by minimizing the use of expensive materials. It is straightforward that solutions to join dissimilar materials have become almost indispensable for cutting-edge applications that aim to lighten structures, especially in the automotive, marine and aerospace fields, where they have an impact also on the relevant target of greenhouse gas emissions reduction [40,59–62]. Therefore, all these factors collectively increase the need to study dissimilar welds. This should not only be performed from a manufacturing point of view, but the evaluation of the mechanical quality of these joints should be considered, as well.

Advanced techniques to join dissimilar metals are constantly developed and optimized [63–67] and among those, laser welding is one of the most widely employed, being a flexible process capable of producing high-quality welds with narrow heat affected zones [42,58]. However, the process of welding dissimilar materials entails several critical issues [58,68]. Due to different physical and chemical properties, a direct junction of the dissimilar materials can lead to the formation of micro-cracks and brittle intermetallic compounds, thereby deteriorating the mechanical properties of the dissimilar joint [69–72]. On the one hand, a way to address these problems, when adopting fiber laser welding, is to

properly tune the processing parameters, selecting a combination of higher laser power, higher welding speed, and focusing the beam with an offset toward one of the two welded materials [40,73]. On the other hand, the above mentioned issues can also be overcome by interposing suitable metallic inserts, thus inhibiting the development of brittle phases [74–79]. As a result, dissimilar joints can be particularly complex being made of more than two materials. The inherent complexity of this kind of joint would require a wise integration of different experimental approaches for a deeper comprehension of the mechanical behavior.

However, an up-to-date quality assessment of these joints mostly relies on research focused on evaluating microstructure, hardness, shear strength for lap joints or tensile strength for butt welds [40,42,75–78], and corrosion [80,81]. Many aspects cannot be fully captured by those analyses, especially when dealing with complex loading states, such as fatigue, which is a crucial condition for numerous applications in the automotive, marine, and aerospace fields, for which specific requirements are included in rules and regulation. As reported in [68,82], the fatigue strength of welded structures is a critical issue due to the formation of brittle intermetallic compounds and micro-cracks during welding [40,41,58]. Furthermore, the dissimilar welding process produces a residual stress field [1]. When welding dissimilar materials, residual stresses develop as a result of thermal cycles and of different Coefficients of Thermal Expansion (CTE) for each material, thereby significantly affecting the mechanical properties of the joint, most notably fatigue life [54,55]. Therefore, a comprehensive assessment of the residual stress state plays a key role in the characterization of dissimilar joints [2].

Nevertheless, most of literature studies investigating the residual stress state of laser-welded dissimilar joints are limited to localized and superficial measurements by X-ray diffraction (XRD) and hole drilling without any attempt to correlate this information with the fatigue behavior of the joint [83–86]. Furthermore, the majority of the research on fatigue properties of dissimilar welded joints does not analyze residual stresses and their contribution by any means. Conversely, only few studies investigated at the same time fatigue and residual stresses in dissimilar joints [87–91]. In [87], Scialpi et al. analyzed the fatigue behavior of an ultra-thin friction stir welded joint consisting of two different aluminum alloys, and performed hole drilling measurements. They found limited compressive residual stresses affecting the dissimilar joint; however, these results were influenced by the low plate thickness. Zhang et al. [88] studied the fatigue life of a dissimilar welded T-joint between SAF2205 and AISI 304. Residual stresses were measured using impact indentation method along a linear path at the weld toe;

nevertheless, to obtain more information, the authors had to perform a finite element simulation of the welding process. They found that the effect of residual stresses on fatigue estimation was significant and that residual stresses mainly affected mean stress rather than the stress amplitude. In addition, Ahmad et al. [89] had to perform a finite element analysis for residual stress assessment of a multi-pass welded joint between a Nickel alloy and 12Cr steel, using six surface hole drilling measurements to qualitatively validate numerical results. Therefore, the numerical results were used to investigate the effect of residual stresses on the fatigue stress range by exploiting a modified Goodman equation which takes into account welding residual stresses. Other research works on the fatigue behavior of dissimilar joints have only carried out point and surface measurements by X-ray diffractometry [90,91].

In view of the foregoing, to pursue a comprehensive investigation of the mechanical quality of dissimilar joints, it is necessary to study the fatigue properties and their correlation with residual stresses and defects. To carry out this extensive analysis, the authors propose to integrate information from fatigue characterization accompanied by thermographic analysis techniques, residual stress field assessment using experimental techniques as X-ray diffractometry and contour method, and fractographic and chemical evaluation of fracture surfaces. Therefore, a better understanding of the fracture modes can be obtained from information on the residual stress field, not only at the surface but also at depth, and from the analysis of fracture surfaces. Consequently, these results can be correlated with fatigue results with more confidence and accuracy, especially considering the complexity of dissimilar welds.

The aim of this research is to propose a comprehensive experimental approach to characterize the fatigue behavior of dissimilar joints, taking into account the relationship with residual stresses and fracture modes. A complex 2-mm-thick laser-welded Ti6Al4V/Inconel 625 dissimilar welded joint with intermediate inserts of Vanadium and AISI 304 was considered as case study [92,93]. Titanium alloys combine high strength with good corrosion resistance, while Inconel alloys exhibit superior mechanical properties even at elevated temperatures. This combination of materials would greatly reduce production costs of gas turbine engines, power industry parts, and even for ocean engineering systems (pipelines) [93]. Residual stresses, both longitudinal and transverse to the weld beads, were measured on surface by means of X-ray diffraction, whereas, for in-depth measurements, the multiple-cut contour method was implemented to determine full 2D maps of longitudinal residual stresses with the first cut, and transverse stresses in the

Vanadium insert. A detailed analysis of the fractured surfaces was performed. In this way, the fatigue behavior was investigated, highlighting the correlation between fatigue strength, residual stresses, and fracture modes to thoroughly evaluate the mechanical quality of the dissimilar joint. The suggested investigation approach, which combines information from several advanced experimental and numerical analysis, is aimed at providing a reliable and complete methodology to assess the quality and retrieve information on fatigue life of complex dissimilar welded joints. This approach provides more detailed and consistent data in comparison to the great majority of current literature, which are crucial to assess the reliability of similar welded solutions, especially in applications requiring advanced performance and accurate knowledge of the main features of the material.

2.2.2 Materials and methods

The suggested experimental methodology aimed at analyzing the fatigue behavior of dissimilar joints is structured as follows:

- as a first step, surface residual stresses are measured, both in the longitudinal direction and transverse to the weld seams, through a more precise and possibly nondestructive technique, such as X-ray diffraction;
- next, measurements are extended to depth by exploiting the contour method, which determines a 2D map of residual stresses acting normal to a plane [13]. This technique is easily applicable and particularly suitable to welded joints, owing to the fact that it is not affected by microstructural changes and inhomogeneities, and it is capable of capturing even steep stress gradients [13,32]. Indeed, it has been successfully employed on dissimilar joints, especially friction-welded [36–39,92];
- since the contour method is a destructive technique and capable of measuring only one stress component per each cut, longitudinal stresses, which are generally larger in magnitude, should be measured as first followed by transverse stress;
- subsequently, fatigue tests have to be performed in conjunction with a thermographic analysis of the increase in surface temperature of the specimens to monitor the failure zone [93];
- finally, fractographic and chemical assessment of the fracture surfaces has to be carried out;
- a final integration of all the information will allow for a thorough evaluation of the fatigue behavior of the joint and of the mechanisms and

the nature of the observed fracture.

The proposed methodology has been developed for one of the three dissimilar joints analyzed in the previous section of the thesis (Section 2.1). The materials and welding conditions for this type of dissimilar joint are again summarized here for ease of reading.

To manufacture the complex dissimilar joints examined, two inserts of pure Vanadium and AISI 304 were selected to join Ti6Al4V and Inconel 625 to inhibit the formation of Ti_xNi_y brittle phases. Additional information on the selection of this particular combination of interlayers can be found in [92,93]. The chemical compositions of the base metals, Vanadium and AISI 304 are reported in Section 2.1 in Table 1 and Table 2. Moreover, the mechanical properties of the investigated alloys are summarized in Table 10.

Table 10. Mechanical properties of the materials composing the welded plate [45,46].

Materials	σ_y **[MPa]**	σ_u **[MPa]**	**E [GPa]**	ν	ϵ_u **%**
Ti6Al4V	880	950	125.5	0.36	10
Vanadium	439	472	120.2	0.36	27
AISI 304	215	515	196	0.28	70
Inconel 625	460	880	208	0.28	45

Two butt-welded specimens were manufactured, with the same welding conditions, using the welding set-up reported in Figure 16 (Section 2.1). More details about the welding conditions have been given in the previous Section 2.1. A schematic drawing of the welded plates along with their dimensions is depicted in Figure 2.

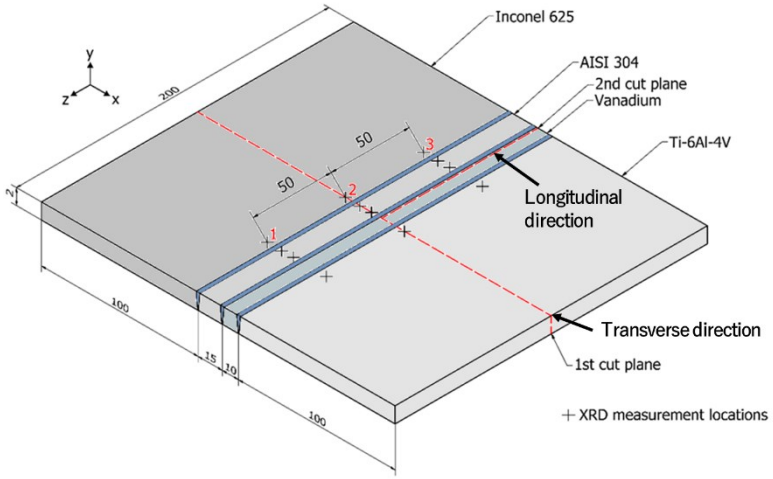

Figure 31. Schematic illustration of the welded plates. XRD measurement locations are indicated by crosses, while the two cuts used for the contour method are displayed by red dotted lines. All dimensions are in mm.

The residual stress state of the dissimilar welded joints was evaluated both on the surface and in depth to predict the fracture zone.

First, surface residual stresses, both longitudinal and transverse to the weld seams, were measured using X-ray diffraction. Thereafter, with the purpose of extending the investigation in depth as well, longitudinal residual stresses along the cross section were evaluated using the contour method. Finally, to complete the residual stress characterization and to consider fatigue test conditions, where the load is applied along the transverse direction, this component of residual stresses was also investigated. Due to the fact that the contour method is a destructive measurement technique, the plane along which the second cut is made was carefully chosen. As reported in the Section 2.1, the surface measurements by X-ray diffraction and the longitudinal residual stress map obtained by the contour method revealed that the most critical area was at the interface between AISI 304 and Vanadium; which has the lowest mechanical strength (Table 10); therefore, the second cut was carried out in the Vanadium insert near the weld with the stainless steel.

To investigate surface residual stresses, X-ray diffractometry measurements were carried out. A Xstress 3000 G3R X-ray diffractometer by Stresstech was used to measure both longitudinal and transverse surface residual stresses. It was instrumented with a Ti tube (λ = 0.274851 nm) for Titanium grade 5, and with a Cr tube (λ = 0.22897 nm) for Inconel 625 and AISI 304. Residual stresses were evaluated at three different points for each material composing the dissimilar joint, except for Vanadium for which the measurement could not be performed due to instrumental limitations. Each measurement point was located approximately 0.5 mm from the

weld seams, as shown in Figure 31. The $\sin^2\psi$ method was applied according to UNI EN 15305 standard [50]. The experimentally measured peak profile was interpolated by Pearson VII function, which allowed for the identification of the diffracted intensity, the K-alpha 1 position of the diffraction peak, and the width of the peak itself. The parameters used to perform X-ray diffraction measurements are reported in the previous Section in Table 7.

The implementation of the contour method complied with the following steps. Specimen cuts were performed using wire electric discharge machining (EDM), the contours of the cut surfaces were acquired using fringe projection. Contour data were processed and finally a finite element analysis was performed [14,92]. Standard contour method procedure was used to map longitudinal residual stresses along the first cut plane, which divides the welded plate in half along the transverse direction (Figure 31) [13,14,29,92]. Conversely, the new approach for asymmetric stiffness cuts, reported in [94], was applied for the second cut, which separated the welded joint into two parts that did not possess mirror symmetric stiffness (Figure 31). Furthermore, the original transverse residual stresses, in the plane of the second cut, were obtained by elastic superposition of the calculated stresses relaxed from both cuts [95].

Each contour cut was performed using an Agiecut Classic 2S wire EDM machine with a 250-μm-diameter brass wire and skim cut settings, submerging the specimen with deionized water and clamping it symmetrically with fixtures placed as close as possible to the cut line to minimize deformation during relaxing of residual stresses [13,14,20,29]. Moreover, to assess the longitudinal residual stresses, the plate was divided in half along a plane transverse to the three welds. The second cut, for transverse stresses evaluation, was parallel to the weld beads and crossed the Vanadium insert at a distance of 0.5 mm to the weld with the stainless steel, as shown in Figure 31. Before measuring the surface profile, the cut parts were kept in a temperature-controlled laboratory until reaching thermal equilibrium with the environment. In this study, as previously detailed, the measurement of the cut surfaces was achieved using fringe projection, a full-field optical technique that shortens the time of this phase of the contour method [43,44,92]. . The measurement setup, consisting of a fringe projector, a camera with resolution of 2 MPix and a computer, is shown in the previous Section in Figure 18.

The processing of the two point clouds obtained from the first cut was carried out following the same procedure reported in the previous Section [92]. A three-dimensional elastic Finite Element (FE) model of the cut part of the sample was built using ABAQUS® software and applying the mechanical properties reported in

Table 10. C3D8R elements were used with dimension of 0.1 × 0.1 × 0.1 mm^3 for the first and second cut planes. The sign of the averaged and smoothed contour of the first cut was reversed, then this point cloud was imposed to the FE model as initial boundary displacement. To process the clouds of the second cut, the procedure outlined in [94] was adopted. According to this methodology, the point clouds are not averaged before back-calculating the residual stresses, as in the standard contour method, which does not allow for the contribution of shear stresses to be eliminated. Conversely, the two contours are considered separately, they are smoothed and then applied to distinct FE models of the two cut parts with side-specific stiffnesses. After FE analyses, the back-calculated stresses are averaged to remove shear stress errors. Finally, as mentioned above, the uncut transverse residual stresses were reconstructed using the superposition of results from the first and second cut [95].

Experimental fatigue tests and fracture surface analysis were conducted in collaboration with the University of Messina to obtain information that correlates with the results of residual stress measurements. Fatigue tests were performed at room temperature with an Italsigma servo-hydraulic testing machine equipped with a 25 kN load cell, at a frequency of 10 Hz. An infrared (IR) camera (FLIR Systems SC640 IR camera, with a resolution of 640 × 480 pixels) was employed to monitor the surface temperature of the specimen during each fatigue test. The specimens were black painted to enhance their emissivity. The thermograms were captured at 1 frame each 30 s by FLIR ResearchIR Max software. Tests were performed using a load ratio R = 0.1 to avoid compression stresses, which could affect the results causing compression instability [96]. Given that the weld is a weak point of the specimen, no dog-bone sample shapes were needed.

Fractographies were carried out by both Optical Stereomicroscope (OM) and Scanning Electron Microscope (SEM). The former is a Leica Microsystems M165C stereomicroscope; the latter is a Hitachi TM3030 plus equipped with Thermo Scientific NORAN System 7 X-ray Microanalysis System. Energy Dispersive X-ray Analyses (EDS) were carried out by point-and-shot spectrum, line-scan and surface map tools to assess the elemental composition of the fracture surface and to evaluate whether the crack path was affected by the presence of some particular phases formed after the welding process. The surface topographies and the average values of surface roughness (Sa) were measured by a confocal microscope (Leica DCM 3D, Leica Microsystems). Statistical analyses were made on an area of 0.64 × 0.5 mm^2 according to ISO 25178, by means of LeicaMap 6.2 software. These scansions were obtained by an EPI 20X-L objective in LeicaScan DCM 3D software. The z-scan

covered a height of 360 μm with a z-step of 6 μm, being z the orthogonal direction to the fracture surface.

2.2.3 Residual stress results

The measurement and analysis of residual stresses provide a variety of information. Prior to fatigue tests, it allows for the presence of stress concentration zones to be highlighted, and consequently to predict possible fracture zones. Whereas, after the analysis of fracture surfaces, knowing residual stresses supports a better understanding of the main mechanisms and causes of failure.

Surface longitudinal and transverse residual stresses, measured by X-ray diffraction at the spots marked in Figure 31, are given in Figure 32 and Figure 33, respectively.

Figure 32 shows high compression on the surface of the Inconel 625 reaching −300 MPa, while the highest tensile stresses occur in the AISI 304 at the weld with the Vanadium. The transverse residual stresses, reported in Figure 33, highlight extremely high compressive stresses, up to −550 MPa, in the Inconel. Furthermore, in the Ti6Al4V and in the AISI 304 at the interface with the Inconel, slight compression or low tension is detected, whereas, at the weld with the Vanadium, the AISI 304 is always characterized by surface tension, ranging from 60 to 90 MPa.

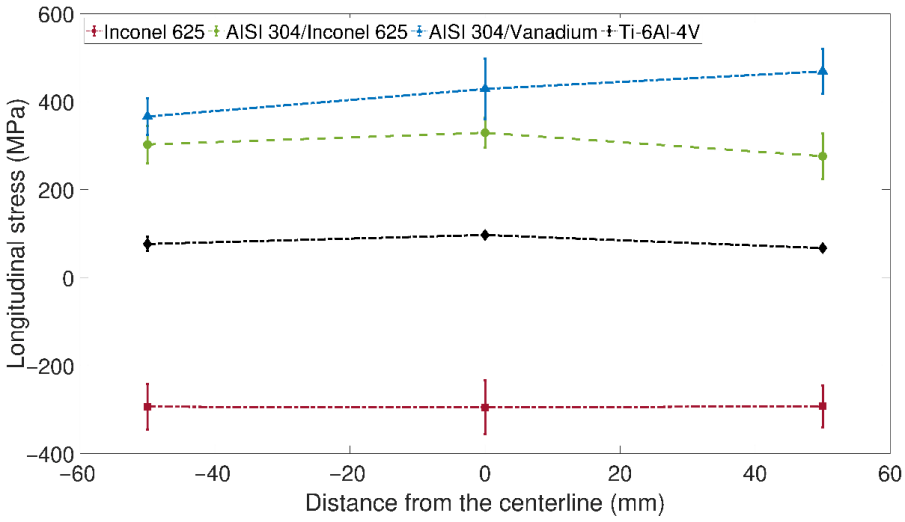

Figure 32. Surface longitudinal residual stresses measured by X-ray diffraction (stresses are in MPa).

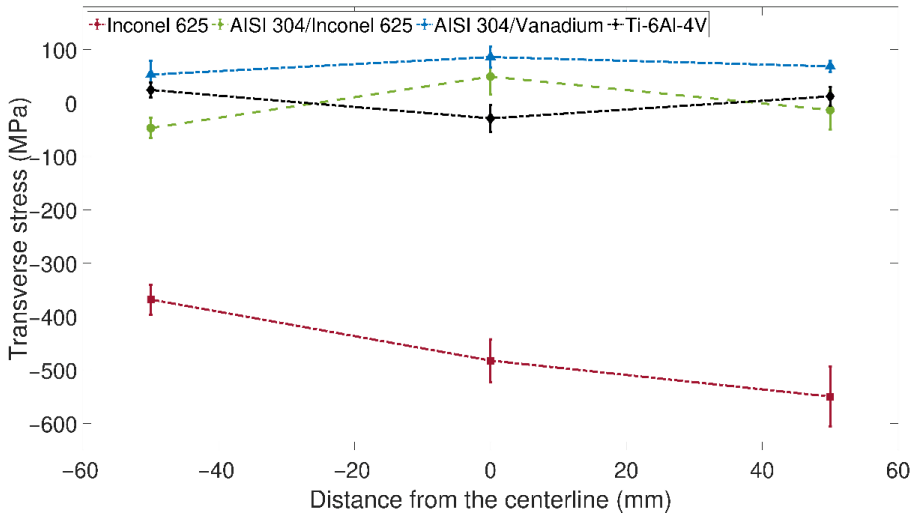

Figure 33. Surface transverse residual stresses measured by X-ray diffraction (stresses are in MPa).

The procedure developed by Prime et al. [25] was adopted in the implementation of the contour method to select the cubic fitting splines which minimizes the average stress uncertainties over the whole stress maps. To evaluate these uncertainties, the number of knots along the largest dimension of the cross sections was varied uniformly, while along the thickness only two knots were used to avoid overfitting. The average stress uncertainties with the corresponding knot spacing of the cross sections' largest dimension are reported in Table 11. For the second cut, the average stress uncertainties were calculated separately, where side A corresponds to the Inconel 625 side of the cut part, while side B is the Ti6Al4V side. In addition, the uncertainty for the final map of the transverse residual stresses was estimated by averaging the stress maps of the two sides and then applying the procedure outlined in [25].

Table 11. Knot spacings of the cross sections' largest dimension and average stress uncertainties for the first and second cut. Side A corresponds to the Inconel 625 side of the cut part, while side B is the Ti6Al4V side.

Cuts	Knot Spacing [mm]	Average Stress Uncertainty [MPa]
First Cut	18.72	32.05
Second Cut Side A	15.82	78.10
Second Cut Side B	14.32	12.22
Second Cut Average	-	35.92

The smoothed surface profiles of the first cut and of the two sides of the second cut are displayed in Figure 34. The peak-to-valley difference of the first cut was

about 100 μm, for the second cut on the side with the Titanium Grade 5 it was around 70 μm, while on the side containing the Inconel 625, the stiffer side, it was only 30 μm. Therefore, this large asymmetry in the normal displacements of the second cut must be taken into account by following the methodology reported in [94], rather than using the standard procedure of the contour method.

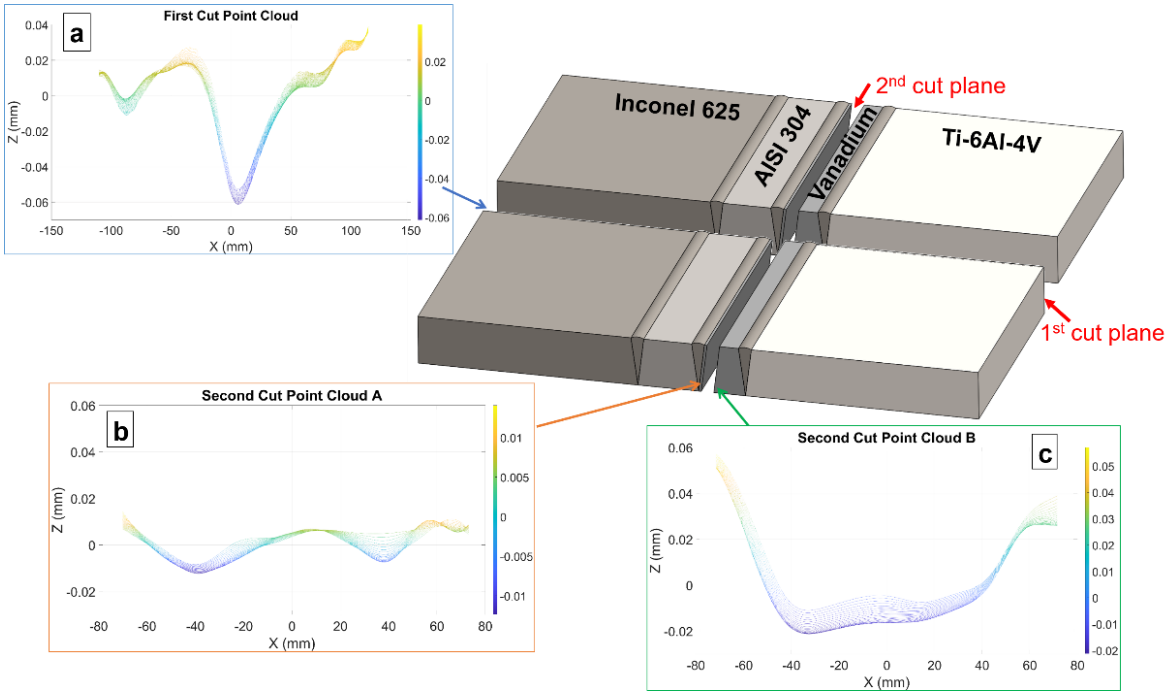

Figure 34. Surface profile of (a) the first cut, (b) the second cut side A (Inconel 625 side), and (c) the second cut side B (Ti6Al4V side), after cubic spline smoothing.

The 2D longitudinal residual stress map is shown in Figure 35. There are harmful tensile residual stresses in the area of the three welds, balanced by compression in the base metals. Notably, the most affected area by detrimental tensile residual stresses is the weld between the stainless steel and Vanadium, where the maximum value of nearly 560 MPa is reached. Furthermore, in the weld between Inconel 625 and AISI 304, high compression is recorded on the surface of the Inconel 625 side extending from the joint toward the base metal.

In dissimilar welds, residual stresses are generated not only by the welding process, but also by the different CTEs of the two welded materials [54,55]. During cooling from the melting temperature, a larger shrinkage affects the material with the higher CTE, but this is restrained by the parent material and the material with the lower CTE, which undergoes a lower contraction. Once the cooling process is over and room temperature is reached, the material with higher CTE has experienced greater shrinking limitation and consequently is subjected to higher tensile residual stresses. CTEs of the materials are reported in Table 12. The greatest

variation in thermal properties is found at the weld between the AISI 304 and the Vanadium. Indeed, the maximum tensile stress is located in the stainless steel insert right next to the interface with the Vanadium.

From surface residual stress measurements, high tensile stress was found in the weld between the stainless steel and Vanadium. This finding was confirmed by the analysis of longitudinal stresses in depth using the contour method. Moreover, Vanadium is the most critical material since it is characterized by the lowest ultimate tensile stress.

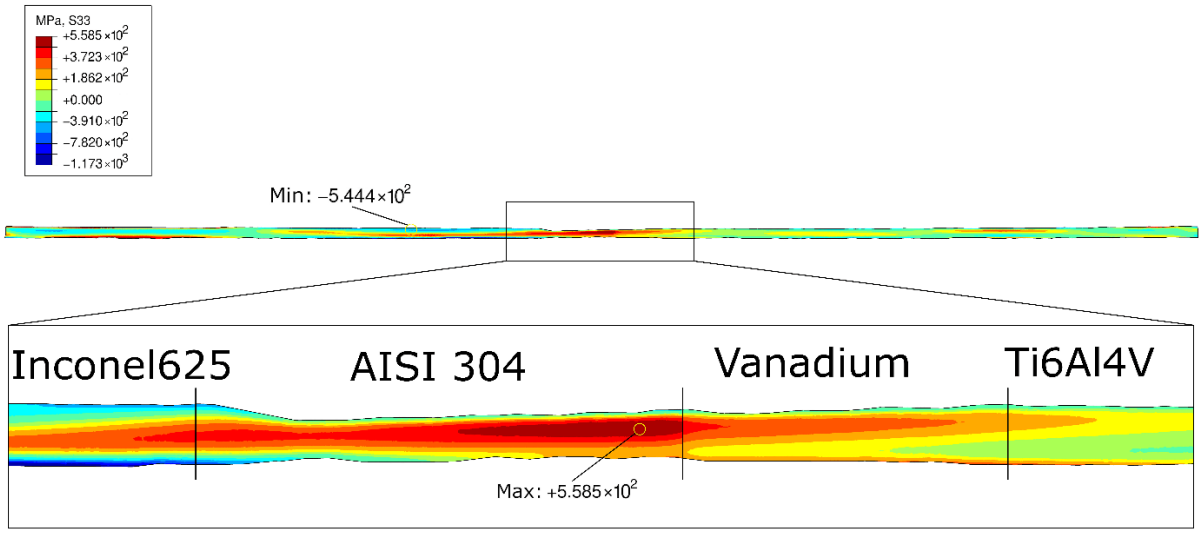

Figure 35. Longitudinal residual stress map (stresses are in MPa).

Table 12. Coefficient of thermal expansion of the materials composing the welded plates [45,46].

Property	Inconel 625	AISI 304	Vanadium	Ti6Al4V
CTE [μm/m K^{-1}]	12.8	17.3	8.3	9.0

Figure 36 shows the map of the transverse residual stresses acting in the Vanadium insert, measured by asymmetric stiffness analysis and superimposing the relaxed transverse stresses from the first cut [94,95]. The end of the welded plate is stress free, while from about 8 mm distance up to the first cut plane tensile residual stresses occur in the core of the insert, whereas compression affects the surface. The maximum tensile residual stress is about 350 MPa. A zone of lower tension, ranging between 60 and 120 MPa, can be seen near the first cut plane; however, no cracks or other sources of stress relaxation were found by visual inspection.

Furthermore, specimens cut in the central plate region, where significantly lower transverse tensile stresses are recorded, might be characterized by better fatigue behavior, if compared to those obtained from the area where the highest transverse tensile stresses were generated. As a consequence, it is possible that the interface between Vanadium and AISI 304 would not be the failure zone. Moreover, compressive residual stresses at the surface, aligned with the loading direction of the fatigue tests, are beneficial for fatigue life. Indeed, as reported in the fatigue results section, the fatigue strength in terms of stress range was found to be high, thus confirming the good quality of the joint.

In the outer region of the maps, high magnitude residual stresses can be found (e.g., −1173 MPa in Figure 35) owing to errors related to splines extrapolation; therefore, they should not be considered [28]. In fact, the maxima and minima stress values in Figure 35 and Figure 36 do not include results from these extrapolated regions.

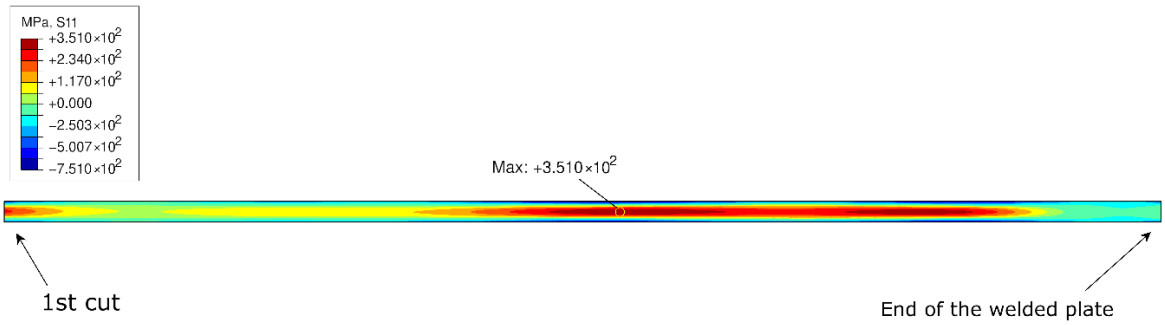

Figure 36. Transverse residual stress map in Vanadium insert using multiple cuts, asymmetric stiffness analysis, and superposition principle (stresses are in MPa).

From the analysis of the residual stresses, it is shown that the most critical area is the interface between AISI 304 and Vanadium, where the highest values of the residual stresses occur, and the most critical material is Vanadium, which has the lowest mechanical strength (Table 10).

2.2.4 Fatigue results

The surface temperature was monitored by an IR camera during each test. A typical temperature map during fatigue tests is shown in Figure 37. The IR technique proved its suitability in identifying the failure zone, which is detected as the area subjected to the maximum temperature. Indeed, the red dot in the images indicates the hottest point (in correspondence of the Vanadium/Ti6Al4V for test 4) which is

the site of the final fracture of the specimen. The thermographic analyses confirm the results obtained by the evaluation of the residual stresses: Vanadium is the critical material in the dissimilar welded joints.

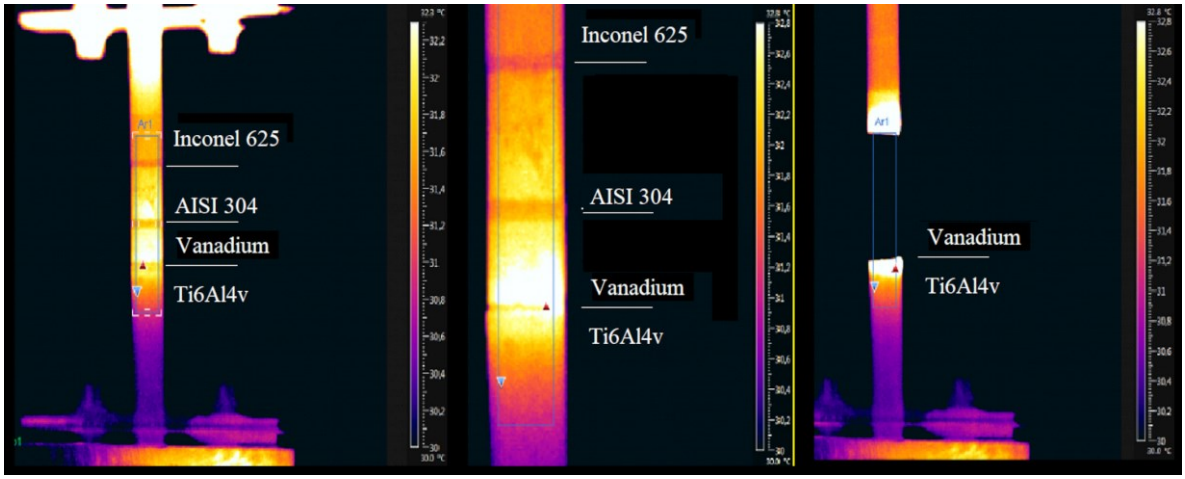

Figure 37. Temperature map during a fatigue test [97].

The parameters used and the results obtained for each fatigue specimen tested are shown in Table 13 and are retrieved from [93]. Due to the limited availability of samples extracted from the welded plates, only one test was conducted for each applied stress range level. The applied stress range $\Delta\sigma$ was calculated considering the nominal stress on the cross-net area to simplify its evaluation. However, in some cases, structural or local approaches in the presence of welds [68,98] could be preferred.

Table 13. Parameters and results obtained from fatigue tests.

Specimen	Δσ [MPa]	Number of Cycles to Failure	Zone of Fracture
1	140	5,000,000	Runout
2	160	5,000,000	Runout
3	170	1,148,109	V-SS
4	180	1,011,176	Ti-V
5	180	2,885,345	Ti-V
6	200	440,740	Ti-V
7	200	192,951	V-SS
8	220	67,000	Ti-V
9	220	149,345	V-SS

Table 13 reports the fracture zone, where "V-SS" is the interface between Vanadium and AISI 304 stainless steel, while "Ti-V" is the interface between

Ti6Al4V alloy and Vanadium. As reported in Table 13, the fatigue tests confirm the results, obtained by analyses of residual stress and thermographic images, that the fracture region is related to the presence of Vanadium, which has the lowest tensile strength. The Δσ-N curve is shown in Figure 38.

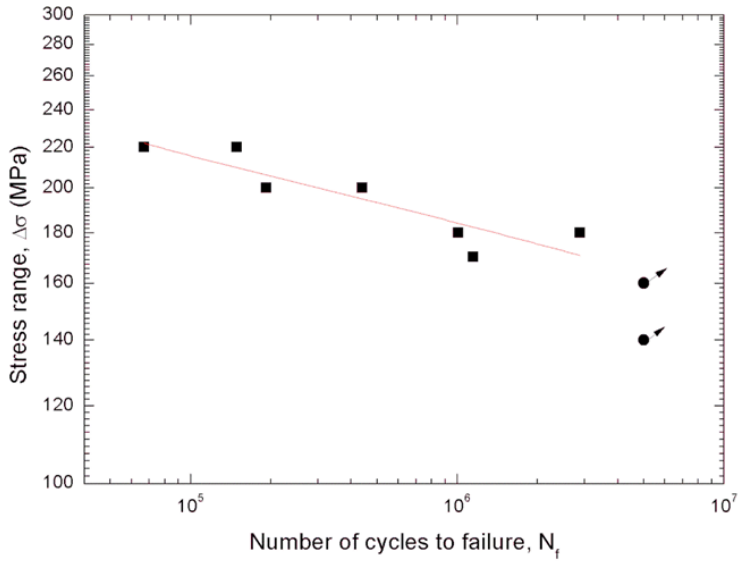

Figure 38. S-N curve of Ti6Al4V-Inconel 625 joints [97].

Although the residual stress analysis correctly identified the most critical material where failure always occurs, the failure originated in the zone of maximum residual stresses only on half of the specimens. Several reasons could be responsible for this phenomenon. First, this observation highlights that residual stresses are not the only factor affecting failure, and it is therefore necessary to perform a thorough fractographic analysis. As it can be seen in Table 13, the contribution of a plurality of factors is further confirmed by the absence of a clear correlation between the applied stress range and the failure zone. For similar welded joints, numerical analyses on the effect of residual stresses on fatigue life have shown that high stress ranges produce a relaxation of residual stresses, as a result of plastic strain, thus their influence is mitigated. Some researchers have found that this relaxation occurs almost exclusively in the very early cycles [99]. While others have reported that residual stresses are significantly lowered in the first cycle due to large plastic deformations, and in the following cycles these decrease progressively due to fatigue damage [100]. The major impact of residual stresses on fatigue life over the high number of cycles was also observed by Zhang et al. in [88] through numerical simulations of a T-joint between dissimilar steels. Due to the complex nature of the dissimilar joint under investigation, this correlation between the applied stress range Δσ and residual stresses is not obvious. In fact, the Ti-V interface experiences

a lower residual stress state than V-SS interface, but it turns out to be a fracture zone even for the low applied stress range $\Delta\sigma$, when instead residual stresses should be the predominant fracture cause (Table 13). However, it should also be noted that specimens 4, 5, and 6 were extracted from the central portion of the plate, where transverse residual stresses are lower, and thus other causes may have been responsible for the fracture at the interface between Vanadium and Ti6Al4V.

The value of the fatigue strength in terms of stress range $\Delta\sigma$ is in the range between 160 and 170 MPa. The value confirmed the good quality of the obtained joints, since the fatigue strength is higher than the value of tensile strength (145 MPa), obtained during static tests which were carried out on laser-welded Ti-Inconel joint [77].

2.2.5 Failure analysis

Starting from the fatigue test results, the fracture surface topography of two specimens (Figure 39) subjected to the same value of stress range $\Delta\sigma = 200$ MPa were analyzed by a confocal microscope. This choice was related to the significantly different fatigue life experienced by the specimens, as well as to the different occurrence of the fracture zone (Table 14).

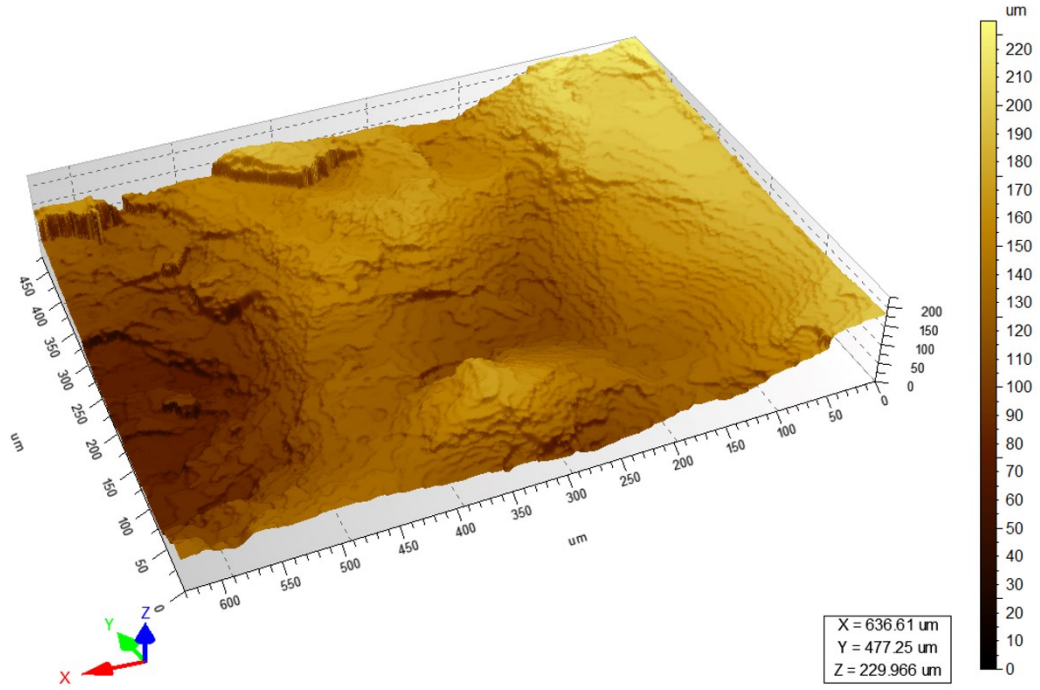

(a)

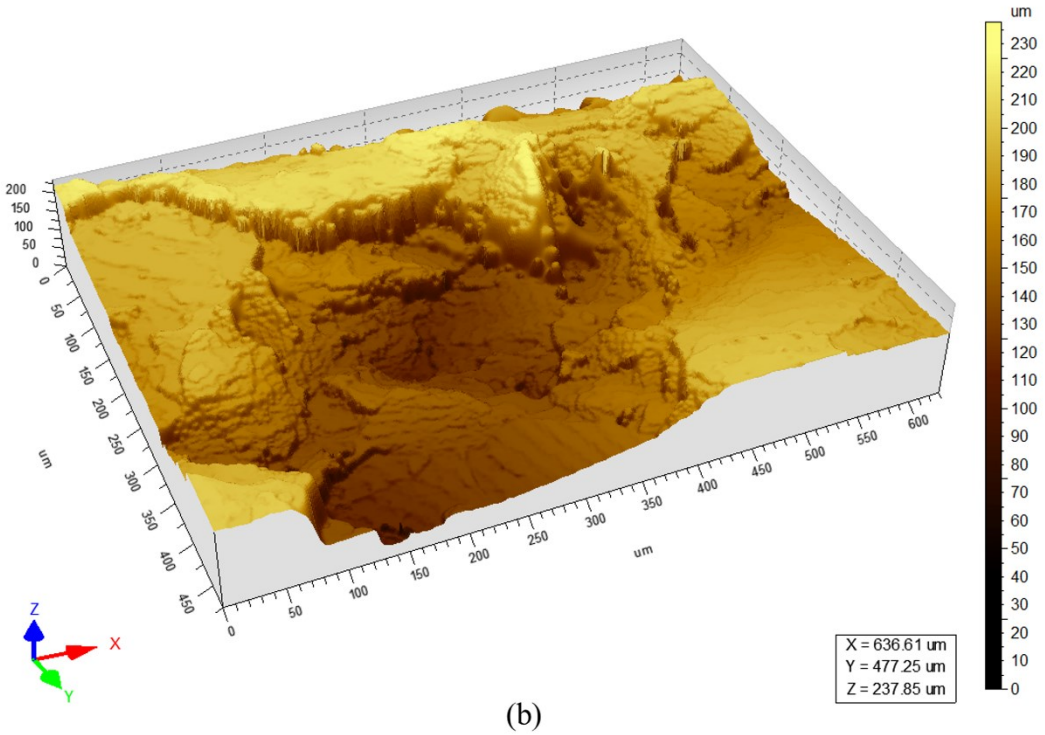

(b)

Figure 39. Surface topography of the specimens tested at Δσ = 200 MPa: (a) Failure at 440,740 cycles (specimen 6); (b) failure at 192,951 cycles (specimen 7) [97].

Table 14. Surface parameters calculated by topographical analysis of specimens 6 and 7.

Specimen	Δσ [MPa]	$N_{fracture}$	Fracture zone	S_q [µm]	S_{sk}	S_{ku}	S_p [µm]	S_v [µm]	S_z [µm]	S_a [µm]
6	200	440,740	Ti-V	48.54	0.11	2.45	127.63	102.33	229.97	39.72
7	200	192,951	V-SS	49.80	−0.15	1.98	101.60	136.25	237.85	42.87

The parameters related to the surface topography are reported in Table 14 and highlight the higher roughness (S_a) of V-SS interface, as well as inverted values of the skewness (S_{sk}). Considering that the skewness is the measure of the profile asymmetry with regard to the mean line, it is expected that the surface of specimen 7 is very unsmoothed. Nevertheless, Persistent Slip Bands (PSB) and a number of irregular crack planes can be seen on the surface (Figure 40(b)). The fatigue life could have been affected by the presence of voids on the crack path. As measured by SEM observations (Figure 40(b)), the dimensions of the discontinuities are similar to those analyzed in [101].

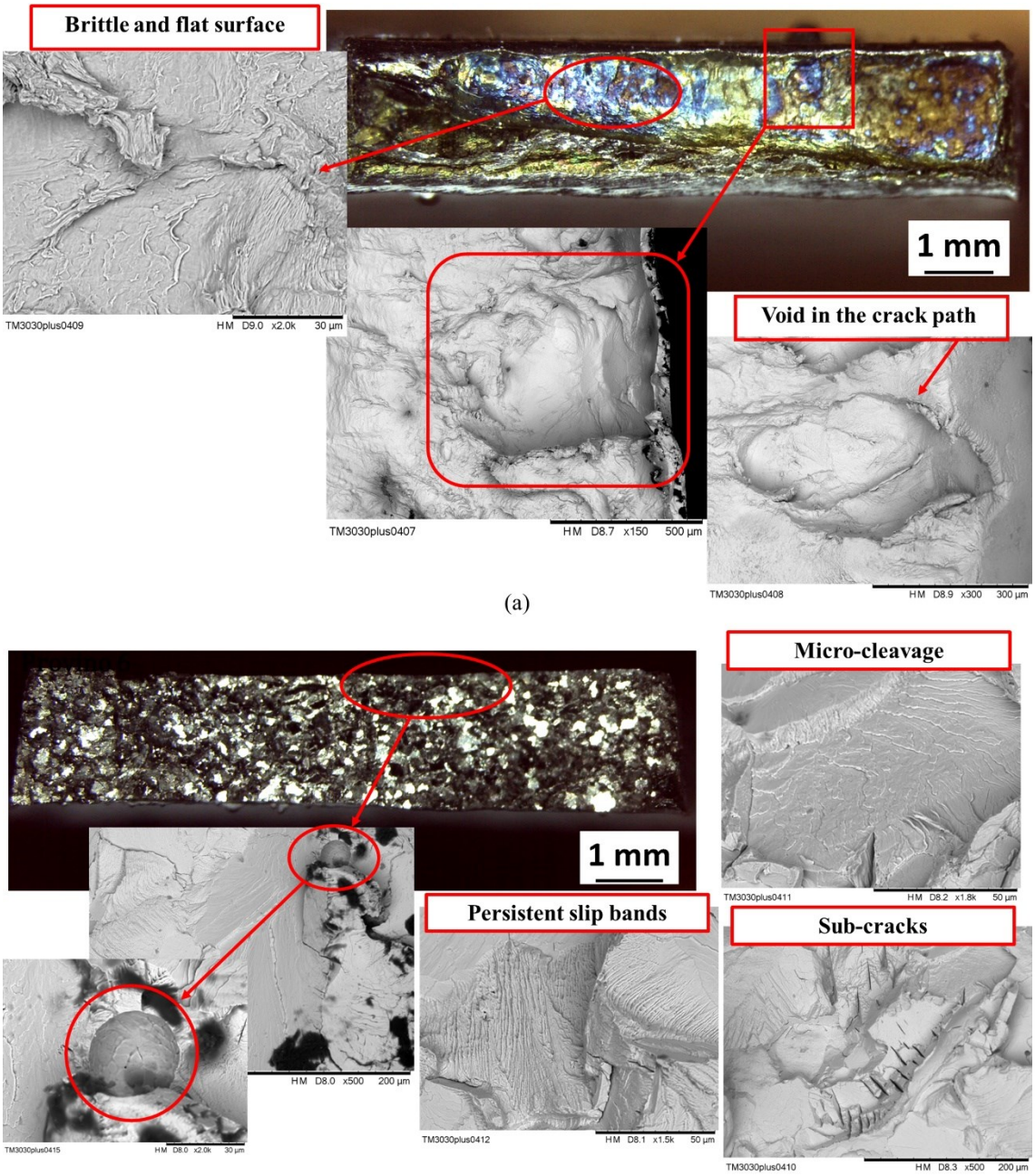

Figure 40. Fracture surfaces of the specimens tested at $\Delta\sigma = 200$ MPa: (a) Failure at 440,740 cycles (specimen 6); (b) failure at 192,951 cycles (specimen 7) [97].

Specimen 6 experienced an initial ductile mode in correspondence of a large void (about 500 mm, Figure 40(a)), while the fast propagation was influenced by other voids, which produced a brittle and flat surface. The initial ductile behavior can be related to the presence of Vanadium at the fracture interface.

Microcleavage crack growth is a low energy process and therefore an undesirable fatigue crack growth mechanism. As shown in Figure 40(a), the microcleavage involves the fracture along specific crystallographic planes, which is the reason for its transcrystalline origin. The surface appears flat and contains

several parallel ridges which represent the cleavage planes.

Analyzing in depth the elemental composition of the fracture surface of specimen 7 (Figure 41), the brittle behavior is due to the presence of voids, considering that EDS did not highlight any relevant modification. In addition to the occurrence of voids, as Panontin and Hill highlighted in [102], the onset of brittle fracture is strongly influenced by the residual stress field, which decrease the J-value for brittle fracture initiation as a consequence of an increase in constraint. In fact, the highest harmful residual stresses occurred at the weld between Vanadium and AISI 304.

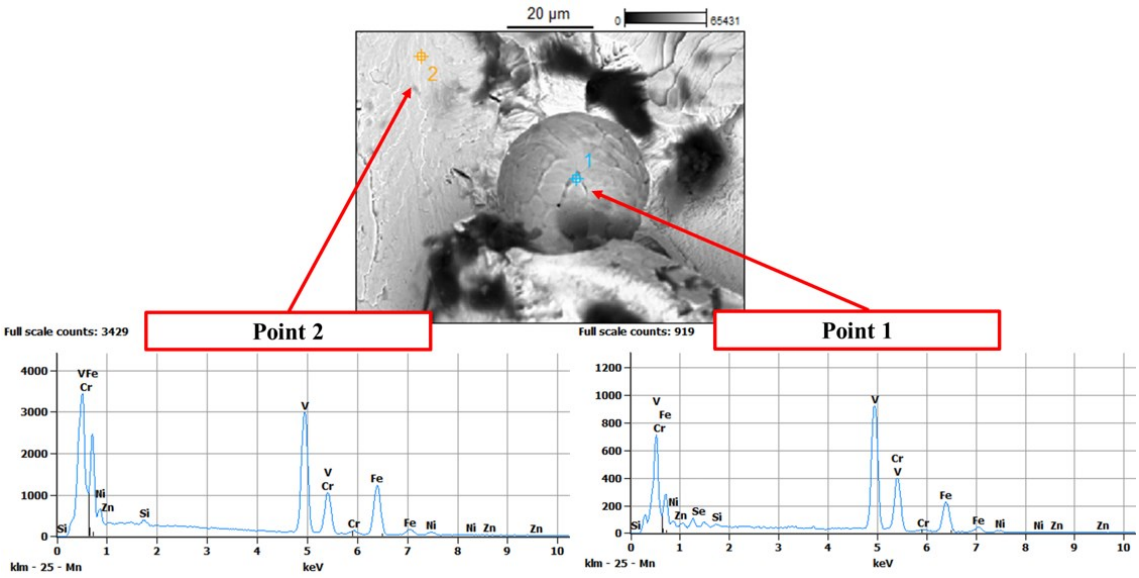

Figure 41. EDS of the specimen tested at $\Delta\sigma$ = 200 MPa and failed at 192,951 cycles (specimen 7) [97].

The specimens subjected to $\Delta\sigma$ = 220 MPa experienced very different fatigue lives (Table 15). In this case, the fracture mode is ductile for the Ti-V interface and brittle for the V-SS.

Table 15. Fracture details for specimens 8 and 9.

Specimen	$\Delta\sigma$ [MPa]	$N_{fracture}$	Fracture Zone	Fracture Mode
8	220	67,000	Ti-V	ductile (striations)
9	220	149,345	V-SS	brittle (micro-cleavage)

In specimen 8, the fracture initiation occurred near the surface of the wider side, where some pores were detected by SEM analysis (Figure 42(a)). The fracture surface is characterized by a ductile mode, with fatigue striations, visible also at a magnitude of 2000X, corroborating the assumption that the crack initiation occurred

as a result of notch effect due to the defects. Nevertheless, the crack propagation was triggered by some discontinuities, about 30 mm wide, found on the fracture surface (Figure 42(b)). EDS spectrum supported the hypothesis that crack path was affected only by defects, as the elemental composition is stable, highlighting elements belonging mainly to the Vanadium phase, considering that its Ka second peak is higher than the Titanium (Figure 42(b)). The first peaks (L_{a1}) are superimposed, due to their proximity in the periodic table of the elements. According to both the shape and the chemical composition of the spherical void, it follows that the void is derived from a gas bubble trapped during the welding process and it is not a slag inclusion that flew out during failure.

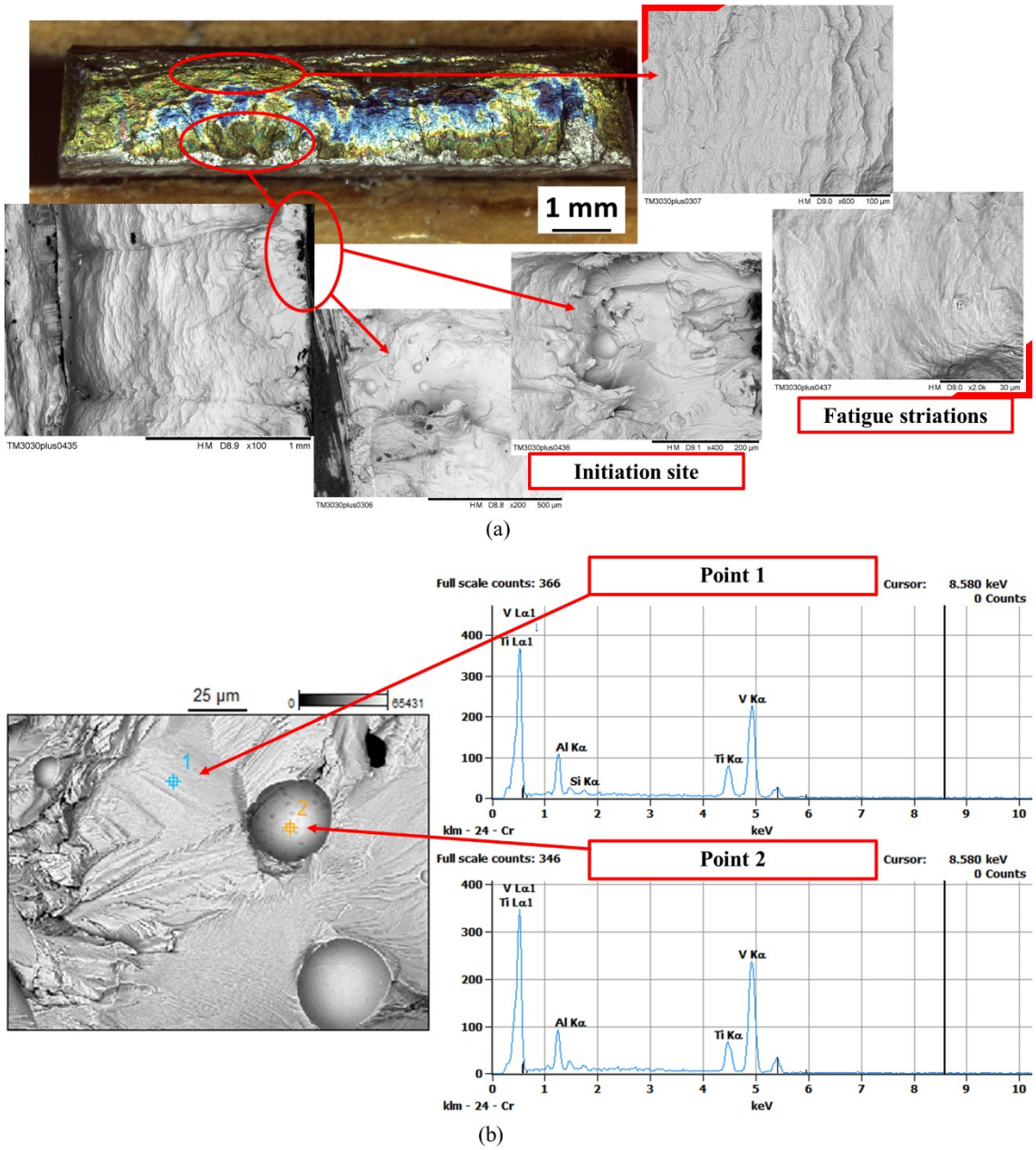

Figure 42. Fracture surface of the specimen tested at $\Delta\sigma$ = 220 MPa and failed at 67,000 cycles (specimen 8): (a) Fractographies and (b) EDS [97].

Specimen 9 experienced similar brittle behavior of specimen 7. The fracture surface is characterized by the presence of an initiation site due to a wide notch effect near the external surface of the specimen. Crack initiation started in a ductile/shear mode on the Vanadium phase. A transition zone follows, in which the crack path became fast and flat (tensile mode), experiencing sub-cracks and river marks, that are the evidence of a brittle and fast rupture phase (Figure 43).

As shown in Figure 38, the stress value which represented the boundary between runout and finite cycles to fracture is $\Delta\sigma$ = 170 MPa (specimen 3). The fracture occurred at the V-SS interface, with an interesting mixed mode (Figure 44).

The macroscopic appearance of the fracture surface is brittle, but, at higher magnitude observed by SEM, it is possible to highlight the presence of slip bands pile-up and micro-voids coalescence (ductile mode), followed by a fast micro-cleavage mechanism (brittle mode).

This complex mechanism can be explained by analyzing the findings of EDS (Figure 45). The initiation site is on the Vanadium phase, which has lower mechanical strength than steel. The change in crack path was triggered by the presence of intermetallic phases, that enriched the area in which the ductile mode was modified in the brittle one. The latter occurred on the steel interface, which, as reported above, is subjected to very high tensile residual stresses due to the welding process.

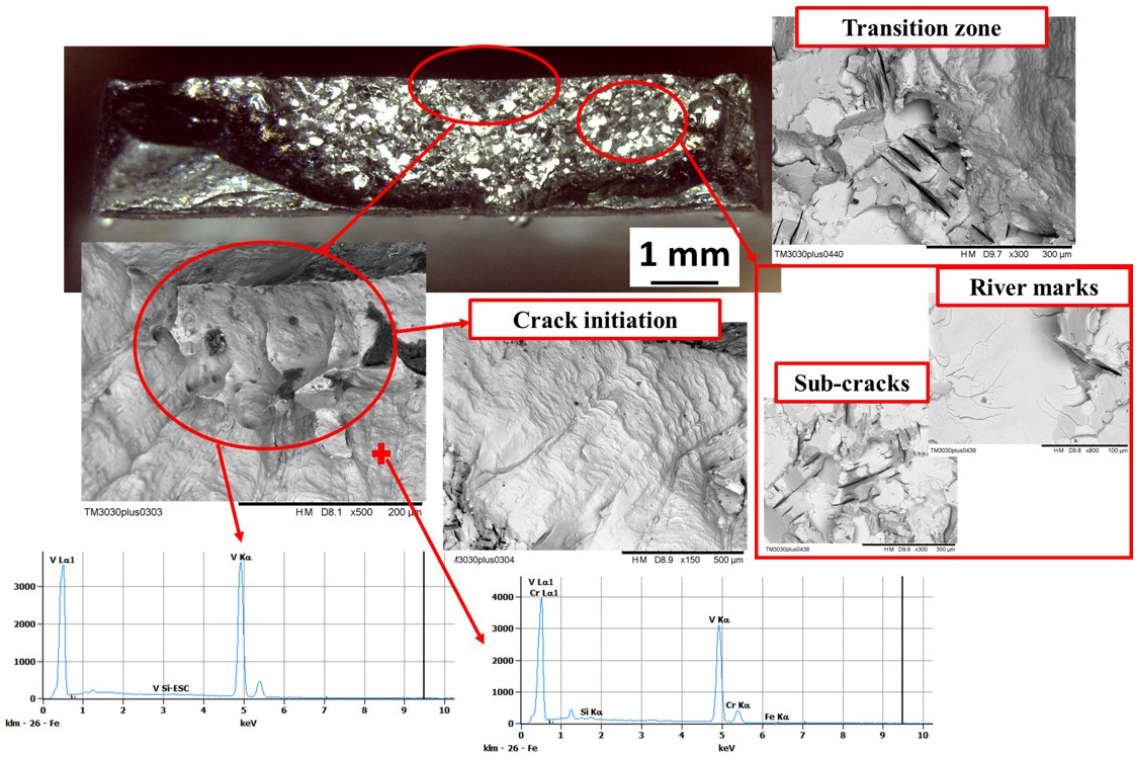

Figure 43. Fracture surface and EDS of the specimen tested at $\Delta\sigma$ = 220 MPa and failed at 149,345 cycles (specimen 9) [97].

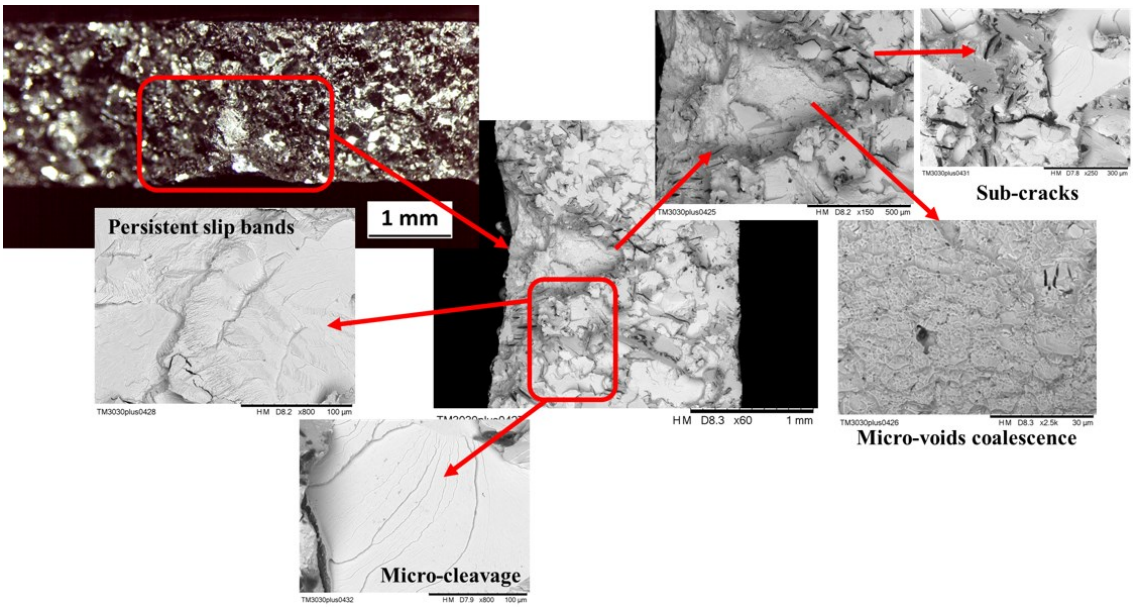

Figure 44. Fracture surface of the specimen tested at $\Delta\sigma$ = 170 MPa and failed at 114,8109 cycles (specimen 3) [97].

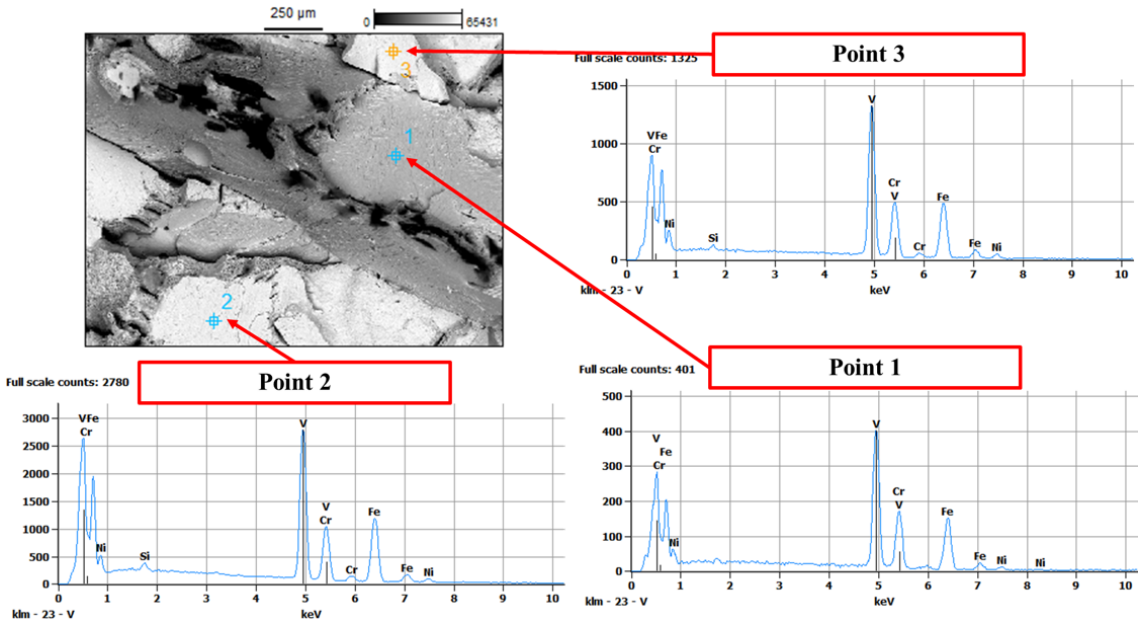

Figure 45. EDS of the specimen tested at $\Delta\sigma$ = 170 MPa and failed at 1,148,109 cycles (specimen 3) [97].

The variation in the crack path due to instable phases is testified by the presence in the same spectrum of Vanadium and Chromium, Iron, Nickel, and traces of Silicon. The analyses of all failed specimens are summarized in Table 16. It is evident how the residual stress field severely influenced the fracture mode of the fatigue-tested specimens, predominantly causing brittle fracture where the residual stresses were higher [102].

The chemical composition of a runout specimen (specimen 1) was analyzed by recording the line-scan of the longitudinal side and the map on the whole lateral

side (Figure 46).

Table 16. Summary of fracture modes.

Specimen	Δσ [MPa]	$N_{fracture}$	Fracture Zone	Fracture Mode
1	140	5,000,000	runout	-
2	160	5,000,000	runout	-
3	170	1,148,109	V-SS	mixed (PSB, micro-voids coalescence, micro-cleavage)
4	180	1,011,176	Ti-V	ductile (striations)
5	180	2,885,345	Ti-V	ductile (striations)
6	200	440,740	Ti-V	brittle and flat (affected by voids, does not change fracture interface but fracture mode and fatigue life)
7	200	192,951	V-SS	brittle (micro-cleavage)
8	220	67,000	Ti-V	ductile (striations)
9	220	14,9345	V-SS	brittle (micro-cleavage)

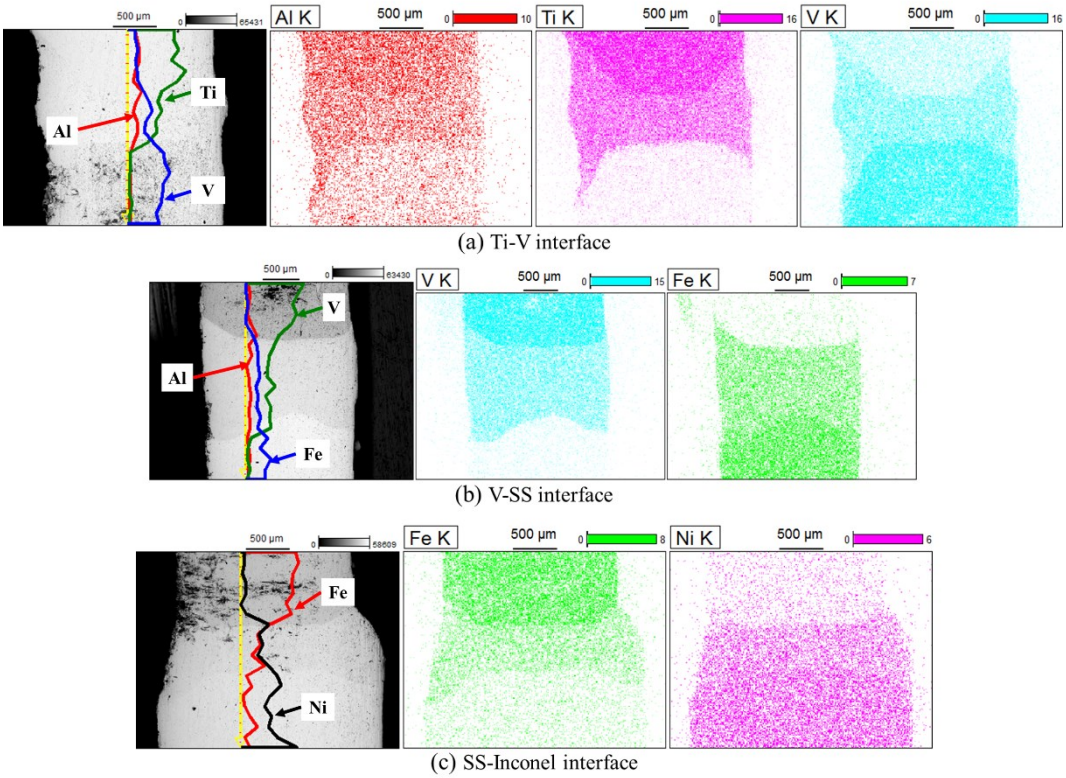

Figure 46. EDS maps of the specimen tested at Δσ = 140 MPa and runout (specimen 1) [97].

2.2.6 Conclusions

The above described piece of study proposed an experimental methodology to assess the mechanical quality of dissimilar joints by investigating the fatigue

behavior, the residual stress field and the fracture modes, highlighting the intrinsic correlation of all the information collected.

First, a comprehensive evaluation of the residual stress state was carried out on a Ti6Al4V/Inconel 625 dissimilar welded joint by measuring it at both surface and depth, exploiting X-ray diffraction and multiple-cut contour method, respectively.

Measurements revealed that harmful tensile longitudinal stresses are located in the three-welds region, balanced by compression in the base metals. The most critical area, exhibiting the highest tensile residual stresses, was the interface between AISI 304 and Vanadium, where the greatest difference in the CTEs occurred. Furthermore, Vanadium was found to be the most critical material, where the fracture was more likely to occur being affected by high tensile residual stresses and has the lowest mechanical strength.

The fatigue tests, performed at load ratio R = 0.1, confirm the location of the fracture zone, predicted by the analysis of the residual stress and the thermographic images; the fracture zone is related to the presence of Vanadium. However, no direct correlation was found between the applied stress range and the residual stresses. This emphasizes that the fatigue failure mechanisms of dissimilar joints are not dependent on a single factor, but on a set of concurrences. The value of the fatigue strength, obtained by the S-N curve, is particularly promising and confirms the good quality of the proposed dissimilar joints with the two intermediate inserts.

Failure analysis was performed to evaluate the fracture modes of specimens tested at the same $\Delta\sigma$. These specimens experienced different modalities and fatigue lives. It was found that the brittle fracture was mainly due to the high residual stresses on the stainless steel side, which exhibited micro-cleavage mechanism, with the presence of Persistent Slip Band, sub-cracks, and river marks. At the optical microscope, the appearance of fracture surface is the typical rock candy one. In these cases, the crack initiation is due to voids (pores).

Persistent slip bands were detected at stress range $\Delta\sigma$ values of 170 and 200 MPa on the specimens that showed brittle fractures. Therefore, fatigue life could be related to the presence of this mechanism, due to the high local plastic deformation. At higher value of stress range $\Delta\sigma$ (220 MPa), the fatigue life seems to be not related to the fracture mode but to a large number of pores cluster on the crack path.

Although the fatigue results showed high mechanical performance, it is worth mentioning that the studied welding process needs to be further optimized to reduce the occurrence of defects. Nevertheless, by means of the proposed comprehensive experimental analysis, which involves careful evaluation of residual

stresses and fracture surfaces, it is evident that the components produced by this technology need to be subjected to treatments that promote stress relief by a thermal or mechanical process (shot peening).

2.3 Residual stress evaluation in innovative layer-level continuous functionally graded materials produced by Powder Bed Fusion-Laser Beam

2.3.1 Introduction

The production of advanced multi-material metal components through additive manufacturing (AM) provides an opportunity to overcome the limitations of traditional materials by combining different and tailored properties in a single structure while maintaining a high degree of design freedom [103,104]. In particular, additively manufactured functionally graded materials (FGMs), which provide a smooth transition between the two dissimilar materials, are increasingly emerging [105]. In this way, issues related to a sharp interface between the two materials with different physical properties are minimized, including the formation of brittle intermetallic compounds, solidification cracking, and more severe residual stress formation due to the sudden change in thermal properties [103,106]. FGMs are distinguished as either discontinuous or continuous. In the former, the spatial variation in composition and properties follows a discrete stepwise pattern, while in the latter this occurs continuously (cFGMs) [105,107]. Directed Energy Deposition – Laser Beam (DED-LB) and Powder Bed Fusion-Laser Beam (PBF-LB) are the most widely employed powder-based AM technologies for the fabrication of multi-material structures [104,108]. Furthermore, because additive manufacturing typically involves layer-by-layer construction, most research has focused on structures where the spatial variation of the composition is along the build direction, especially using DED-LB, while studies where this is within the layer and utilizing PBF-LB are less common and have only recently been realized [104,108–111].

PBF-LB exploits a laser source that melts the powder in a highly localized manner into a melt pool, which then undergoes rapid solidification to build a three-dimensional part in a layer-by-layer strategy. However, due to the extremely steep thermal gradients generated and the repeated thermal cycles to which the material is subjected, a complex and large residual stress field is developed, which can also cause the manufacturing process to fail [112,113]. Residual stresses, if not properly analyzed and controlled, cause cracking during the process, detachment from the

build platform, and significant distortion in the final part [104,112–114]. They also have a major influence on the fatigue properties of AM parts, so that post-process machining or heat treatments are often required to improve their mechanical behavior [115–117].

The onset of residual stresses in AM is due to two mechanisms: the temperature gradient mechanism (TGM) and the cool-down phase, as defined by Mercelis and Kruth in [118]. The TGM defines the formation of residual stresses as a result of the large thermal gradients that occur around the laser spot. After laser passage, the irradiated area is characterized by tensile stresses and surrounded by a compressive region. The cool-down phase, on the other hand, is associated with the shrinkage of the molten top layer, which is constrained by the underlying solid material during solidification, thereby producing tensile stresses in the upper layer and compression in the layers below. In addition, the process parameters used, as well as the material properties, size and geometry, are critical not only to the manufacture of the part, but also to the complexity and magnitude of the residual stresses [10,112,113,119–125]. Laser power, scan speed and scan strategy must be optimized to achieve a fully dense part while minimizing residual stresses and are also material dependent [112,123,126].

Notwithstanding the steady growth of studies on the fabrication of FGM structures, the analysis of the contextual residual stresses generated is scarce, even considering all metallic AM technologies. In particular, residual stress measurements on FGM specimens are poorly reported in the literature. Woo et al. measured the through-thickness residual stress field in five different DED-LB discontinuous between-layer FGM ferritic-austenitic steel specimens using various techniques [110]. They found that by using a bidirectional scanning strategy, the stress trend took on a sinusoidal shape as the number of interlayers increased. In addition, due to the large change in the thermal expansion coefficient observed between the fully austenitic composition and the 50% austenitic and 50% ferritic composition, a significant change from tension to compression is measured, up to 950 MPa. However, by modifying the scanning strategy to orthogonal or island scanning, the residual stress range drops significantly to about 430 MPa and the stress profile across the thickness (direction of composition change) returns to a smoother trend. In a subsequent study, Shan et al. developed a multiscale framework based on the inherent strain method to predict residual stresses and distortion in FGMs fabricated by DED-LB [127]. The authors extended the previous study [110] with a numerical model and found that increasing the number of interlayers to nine mitigated residual stress oscillations and reduced distortion in

the final part. This suggests that moving towards continuous composition variation, i.e. cFGMs, makes the residual stress field more uniform. Furthermore, coupling this effect with the use of an island scanning strategy also leads to a reduction in the residual stress range through the thickness. Ghanavati et al. [128] found similar results, where mitigating sharp changes in residual stress was achieved by adopting a smoother compositional change in a between-layer multi-material SS316L-IN718 structure realized by DED-LB. Li et al. found that implementing buffer layers of AISI 316L and Inconel 718 in multi-material depositions of Cu on AISI 304L by using DED-LB resulted in lower maximum tensile residual stress and defect-free copper [129]. In their investigation, Shin et al. measured only surface residual stresses by X-ray diffraction in steel FGM specimens produced by DED-LB, in which the composition changed from fully ferritic to austenitic along the build direction, by exploiting 3 interlayers of 5 mm each [130]. Zhao et al. have developed a numerical model for residual stress analysis of between-layer TC4-Inconel 718 FGMs [131]. However, their work did not take into account the typical process parameters of PBF-LB, which generate different residual stress fields, and in particular did not consider within-layer FGMs. Rodrigues et al. used wire and arc additive manufacturing to build a AISI 316L stainless steel to Inconel 625 FGM, with a smooth transition along the build direction in steps of 5% composition changes [132]. Compared to a direct transition between the two materials, the FGM specimen exhibited higher residual stresses as measured by neutron diffraction. This result was caused by the greater formation of detrimental precipitates in FGM, which created volumetric mismatches that ultimately generated higher residual stresses. Bodner et al. fabricated a between-layer AISI 316L-Inconel 625 cFGM specimen using a novel deposition technique called liquid dispersed metal PBF [133]. The authors observed that the residual stresses exhibited a C-shaped profile through the thickness of the specimen with superimposed fluctuations at the interfaces between the materials. Subsequently, the same authors measured residual stresses in a multi-material structure fabricated using the same technology, with both between-layer and intra-layer variations of these materials [134]. Extremely high residual stresses, even exceeding 900 MPa, developed as a result of the process. In addition, stress concentrations were observed at transitions between materials, both between- and intra-layer. However, to the authors' knowledge, there is no work that has measured residual stresses in FGMs made by PBF-LB. Furthermore, only Rodrigues et al. analyzed a structure with smooth composition variation, but due to the high number of precipitates, they obtained a counterintuitive result with a direct interface that performed better than FGM, therefore smooth variations in composition

certainly require further investigation [132]. In addition, only Bodner et al. analyzed residual stresses in an intra-layer multi-material structure [134]. In fact, the feasibility of manufacturing such layer-level FGMs by using PBF-LB has been only recently demonstrated, and the contextual residual stress characterization is still lacking in the literature. The mechanical properties of additively manufactured specimens are significantly influenced by the building direction [135,136]. This also applies to the direction in which the variation in material composition is made in FGMs. As a result, the quantification of residual stresses cannot be simply inferred from analogous studies on between-layer multi-material PBF-LB manufactured samples. Finally, none of the above studies analyzed the influence of material-specific process parameters on residual stresses in FGM structures.

In this framework we have decided to evaluate residual stresses in cFGM structures of AISI 316L steel and 18Ni Maraging 300 fabricated via PBF-LB, where the continuous variation in composition is within the same layer. To achieve this goal, the contour method approach was adopted, because of its previously mentioned insensitivity to microstructural gradients that makes it particularly suitable for AM components [14,97,110,137]. In addition, the effect on residual stresses of solution annealing and aging heat treatment, which are required to improve the mechanical properties of martensitic steel, was investigated. Finally, by varying the scanning speed, the impact of adopting material-differentiated process parameters on the residual stress field has been examined.

2.3.2 Experimental procedures and materials for sample preparation

The continuous and functional gradient was obtained between two steels with different metallurgical and mechanical properties. Specifically, the materials studied were AISI 316L austenitic steel and 18Ni Maraging 300 martensitic steel. Both powder materials are derived from a standard gas atomization process and therefore have a spherical shape, making them suitable with the PBF-LB process. Prior to printing, the powders were sieved to obtain a particle size in the range of 15-45 μm. The chemical composition of both, shown in Table 17, was provided by the manufacturers. Additional information regarding the investigated materials can be found in the study [138].

Table 17. Nominal chemical compositions (wt.%) of the martensitic steel powder (18Ni Maraging 300) and austenitic stainless steel powder (AISI 316L) utilized to manufacture the cFGM samples.

Materials	Fe	Ni	Cr	Co	Mo	Mn	Ti	Si	C
18Ni Maraging 300	Balance	18.10	-	9.86	4.65	-	1.10	-	0.01
AISI 316L	Balance	12.60	17.15	-	2.30	1.20	-	0.70	0.01

To study the evolution of residual stresses in components made of cFGMs within the same layer, four parallelepiped-shaped specimens with dimensions of 75x10x12 mm were fabricated. The height of the specimens was chosen to reduce distortion after removal of the build platform [139,140]. The cFGM samples were produced on Concept Laser's traditional M1 machine, which was modified in-house to fabricate cFGM samples within the same layer [141]. The dimension of 75 mm was divided into three regions of 25 mm each, with the central section having a continuous graded transition from 18Ni Maraging 300 to AISI 316L.

The PBF-LB process for fabricating the samples was performed by keeping all process parameters constant except for the laser beam scanning speed, which was varied within the same sample, resulting in a total of three cases. As shown in Figure 47, specimen AM-1 was divided into two processing zones and manufactured with two different scanning speeds: V1, equal to 180 mm/s on the AISI 316L side and V3, equal to 120 mm/s on the 18Ni Maraging 300 side. For specimens AM-2 and AM-3, the scanning speed V1 was kept constant throughout the specimen. Finally, specimen AM-4 was divided into three processing zones and manufactured with three different scanning speeds: the AISI 316L region was produced with a scanning speed of V1, the 18Ni Maraging 300 region with a scanning speed of V3, and the continuous functionally graded region with an intermediate scanning speed of 150 mm/s (V2).The laser power of 80 W, laser beam diameter of 200 μm, layer thickness of 30 μm, and track spacing of 140 μm were consistent process parameters for all samples. Figure 47 displays the three distinct case studies obtained along with the replication for the second case (AM-2 and AM-3).

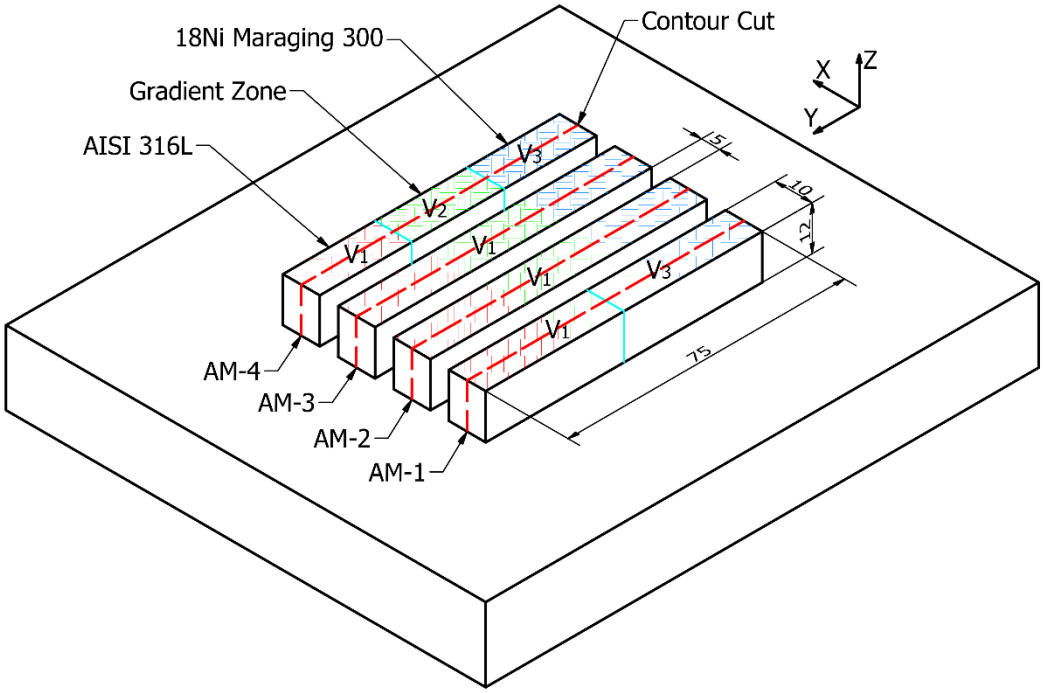

Figure 47. Schematic illustration of cFGM sample dimensions and the three case studies. The island strategy is visible on the specimens' surface with three colors identifying the three composition zones: light red for zones wholly composed of AISI 316L, light blue for those entirely composed of 18Ni Maraging 300, and light green for the composition gradient zones. Solid lines in cyan indicate the boundaries between zones produced at different laser scan speeds. The scanning speeds indicated by V_1, V_2 and V_3 are equal to 180 mm/s, 150 mm/s and 120 mm/s, respectively. Additionally, dashed red lines indicate the cutting planes along which the contour method was applied.

The process parameters chosen for the fabrication of the samples were optimized in previous works by the same authors on the same materials, resulting in a final density of the fabricated samples greater than 99% (tested by Archimedes' method) [142,143].

In addition, all samples were fabricated using Concept Laser's patented random island scanning strategy, which uses a square island size with one side equal to 5 mm. Furthermore, between the different layers, the islands undergo a variation in the XY plane with an offset of 1 mm in both directions. These solutions aim to reduce the thermal stresses generated during the PBF-LB process, as has been demonstrated in the literature [10,110,112,144].

All specimens produced, except for sample AM-2 (see Figure 47), were heat treated to improve the mechanical properties of the martensitic steel. In accordance with previous studies in the literature [138,145,146], a solution annealing treatment was performed at a temperature of 815°C for 1 hour followed by air cooling, and then an aging treatment was performed at a temperature of 480°C for 5 hours

followed by air cooling. Figure 48 shows a photograph of the specimens produced.

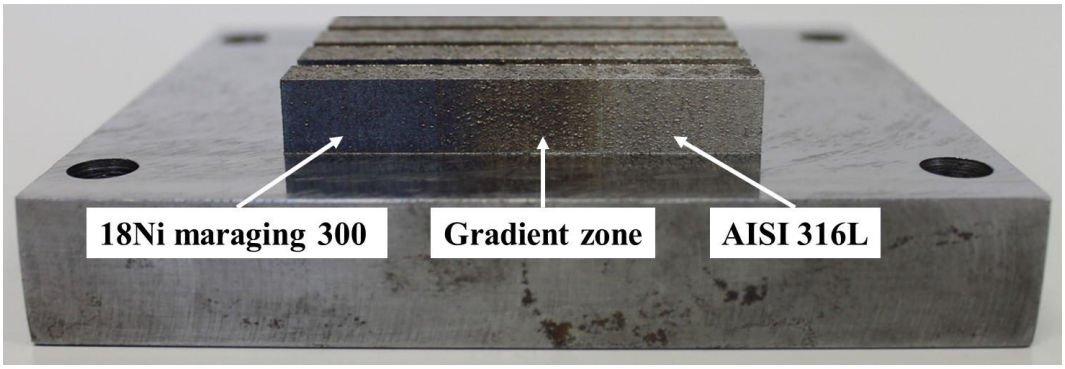

Figure 48. Image of cFGMs specimens fabricated by the PBF-LB process.

2.3.3 Metallographic characterization

In order to evaluate the quality of the joint obtained in the four samples produced, the latter were subjected to metallurgical analyses, such as macro- and microstructural analyses and chemical examinations. The metallographic characterization was performed on the cross sections (YZ plane) of each specimen. The specimens were prepared ad hoc to evaluate the distribution of defects, such as porosity, and to characterize the interface area by studying the possible presence of lack of fusion along the grading direction between the two materials, which could compromise the joint. The specimens were observed using an inverted optical microscope (Nikon Eclipse MA200, Nikon Corporation) with a digital camera. The analyses were carried out in image analysis software such as ImageJ and Matlab, with ad hoc algorithms developed to obtain the desired results.

Subsequently, a microstructural analysis was performed on the same samples by chemical etching in order to reveal the phases present in the different zones and especially in the gradient zone. The chemical reagent used to reveal the microstructure was composed of nitric acid, hydrochloric acid, and lactic acid in a ratio of 1:2:6.

Finally, the samples were chemically characterized to reveal the possible presence of contamination in the areas of pure materials and the gradual and continuous evolution of the chemical composition between the two materials. For this purpose, a microanalysis using an energy-dispersive X-ray spectroscopy (EDS) probe was performed to allow a quantitative pointwise analysis of the chemical composition of the cFGMs specimens fabricated. The chemical examination was conducted along the YZ plane. Characterization was performed using a scanning electron microscope (SEM, ZEISS GeminiSEM 500) coupled with an Oxford

Instruments X-Max Extreme EDS detector.

2.3.4 Contour Method residual stress measurement set-up and procedure

Prior to measurements, the cFGM specimens were removed from the build platform with a single WEDM cut and finishing cutting parameters. Detachment from the build platform can cause distortion in the component or alteration in residual stresses. Nevertheless, in [139,140] it has been shown that specimens with a thickness greater than 10 mm experience significantly reduced distortions compared to thinner specimens. In addition, it has been reported in [147–149] that for parallelepiped-shaped specimens residual stress relaxation subsequent to detachment is more pronounced in the longitudinal direction, while the stress component in transverse direction is minimally impacted and remains present even at high values. Furthermore, Clausen et al. in [150] stated that for samples without internal features, residual stress changes due to build platform removal decrease monotonically with increasing distance from the cut surface, in accordance with the St. Venant's principle [51].

In this research study, transverse residual stresses were measured by cutting the specimens along the YZ plane, as depicted by the dashed red lines in Figure 47. Consequently, the contour method allowed for the analysis of residual stresses along the plane with the composition gradient. At the same time, the stress component least affected by the build platform removal was measured. The material composition gradient, in fact, impacts on the level of residual stresses on such direction. Furthermore, as previously stated, the AM-2 sample was examined prior to heat treatment to investigate its effect on the residual stress state of the cFGM components.

Contour method cuts were performed with an Agiecut Classic 2S WEDM machine equipped with a 250 μm diameter brass wire. To reduce the stresses induced by cutting and prevent the formation of a recast layer, the specimens were immersed in deionized water, clamped symmetrically as close to the cutting plane as possible, and skim cut settings were used. Before measuring the deformed surfaces, the sectioned specimens were held for several hours in a temperature-controlled laboratory to ensure thermal equilibrium. Displacements in the direction perpendicular to the cut surfaces were measured by means of fringe projection [92]. The schematic set-up representation is displayed in Figure 49. A sequence of sinusoidal fringe patterns is projected onto the surface to be acquired, consequently these fringes are modulated in phase by the height distribution of the surface itself

and acquired by a camera with a resolution of 2 MPix (1624 × 1234 pixels). By analyzing the images, the 3D coordinates of the sample surface are reconstructed from the acquired phase map [43,44,92]. For each specimen analyzed, the point clouds measured on the two sides of the cut were aligned and averaged to eliminate the contribution of shear stresses. The peak-to-valley range of the averaged contour was between 30 and 40 μm for all samples, with no significant variation in the displacement profile across all examined specimens. To reduce the effect of noise on the calculated stresses, cubic bivariate splines were employed. The fitting splines' parameters were chosen by minimizing the residual stress uncertainty, following the procedure outlined by Prime et al. in [25]. Afterwards, the experimentally measured perimeter of the deformed surface was utilized to generate a three-dimensional elastic finite element model of the cut part using ABAQUS software. The model mesh was generated using linear brick elements with reduced integration C3D8R, with dimensions of 0.1 mm x 0.1 mm x 0.1 mm on the cut plane and becoming coarser away from it. The regions completely composed of AISI 316L and those entirely made of 18Ni Maraging 300 were assigned elastic moduli and Poisson's ratios of 217 GPa and 0.3, and 203 GPa and 0.3, respectively. These elastic moduli were experimentally measured in a previous study [111] by static tensile tests on single-material specimens. On the other hand, the continuous functional gradient zone from austenitic to martensitic steel was divided into nine discrete parts and assigned the corresponding elastic properties derived by the rule of mixtures. Finally, the smoothed displacements were changed in sign and imposed on the finite element model as boundary conditions, and a static analysis was conducted.

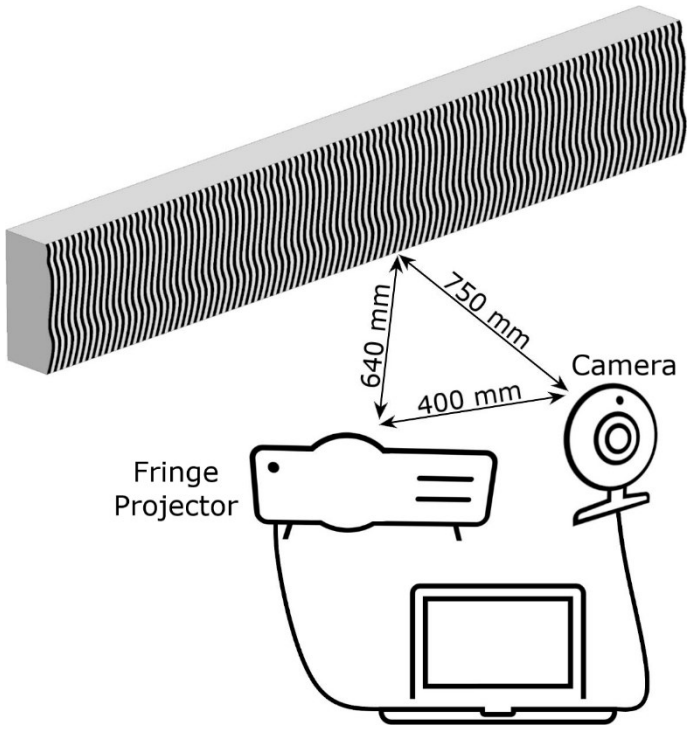

Figure 49. Fringe projection set-up for surface contour measurements.

2.3.5 Results and discussion

Observation of the polished samples using an optical microscope revealed the presence of discontinuities within the fabricated volume. For each specimen, an area with a height of 3.5 mm and a width of 35 mm centered on the transition zone between the two materials was photographed and subsequently examined by image analysis. A binary filter (threshold) was applied to the images to maximize the contrast between the discontinuities and the material surrounding them.

Figure 50(a-d) shows the analyzed images after the application of the threshold and the results of the analysis. The discontinuities detected can all be classified as porosity or lack of fusion based on their shape and no cracks were observed. The porosities were characterized according to their quantity (Figure 50(e)) and their area (Figure 50(f)). Using a bin width of 5 mm for both graphs, the first and last bins represent the results obtained in 18Ni Maraging 300 and AISI 316L, respectively. The remaining five central bins, on the other hand, show the trend of porosity within the mixing zone and are an indication of its gradualness. On the left vertical axis of Figure 50(e) are the percentages of the number of discontinuities for each bin compared to the total number of discontinuities for each sample, which can be read from the bar graph, while on the right vertical axis are the quantities for each bin, represented by the line graph. The same type of representation has been used in the

graph in Figure 50(f). All trends show that there is a gradual reduction in the number of discontinuities and their extent as one moves from 18Ni Maraging 300 to AISI 316L. The only exception is specimen AM-1, which has a high concentration of discontinuities in the area where the process parameters change, in the middle of the mixing zone. It is also important to note that unlike the AM-1 specimen, the AM-4 specimen does not show any peaks in the pore distribution, even though it was produced using variable process parameters.

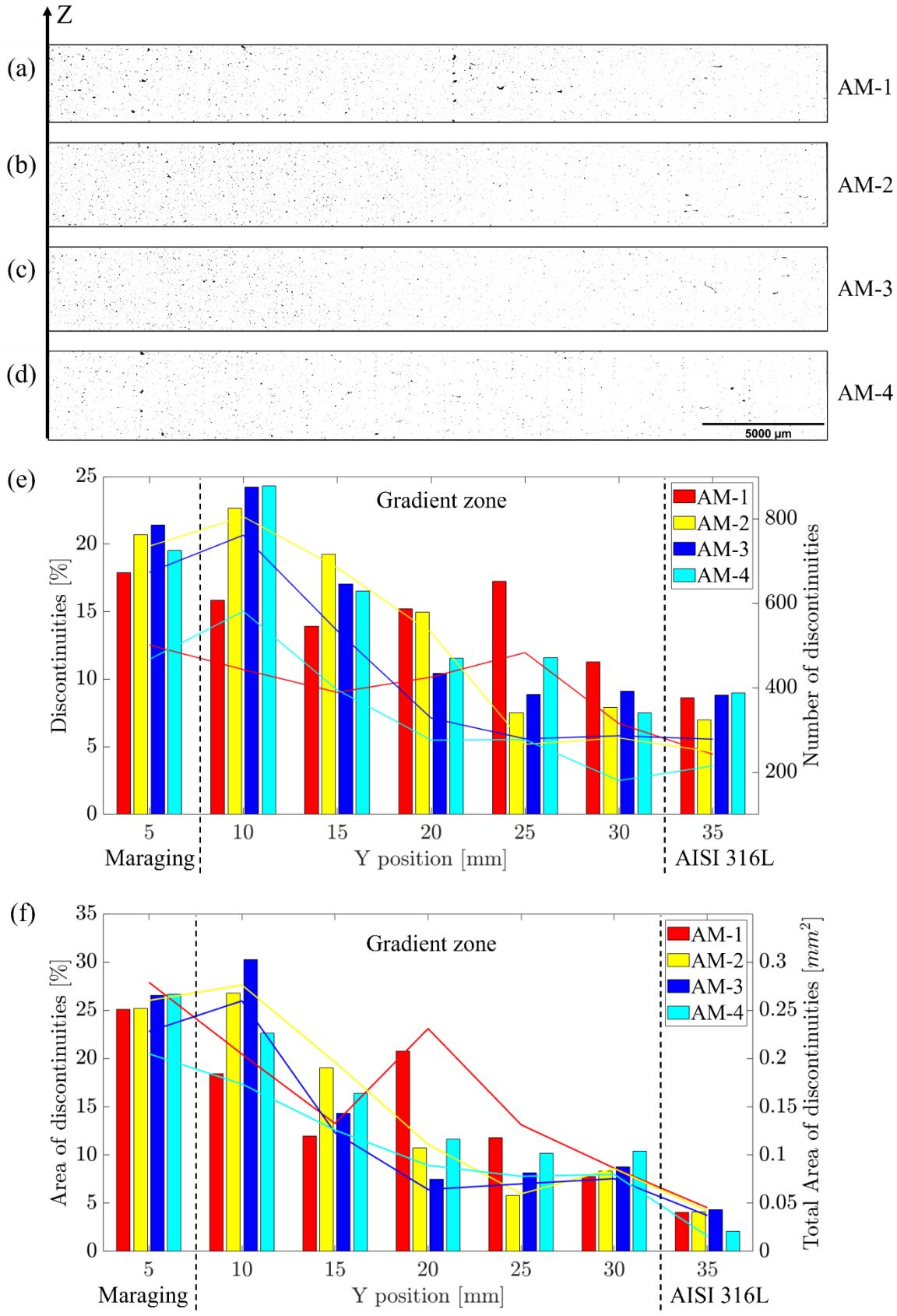

Figure 50. Discontinuity analysis: (a-d) Appearance of the metallographic specimens after threshold application; trend of discontinuities (e) and their extent (f) detected in the metallographic specimens along the Y-direction with 5 mm interval. The bars indicate the

percentage for each interval of the total for each specimen, the lines indicate the absolute amount for each interval.

Information about the different phases can also be deduced by analyzing the chemical concentrations of the elements in the two materials involved. Figure 51 shows the chemical composition determined in the central region of samples AM-1, AM-3 and AM-4. The analysis was conducted on the cross sections (YZ plane) of each sample. The study area is equal to 30 mm along the Y-direction and includes within it the graded interface equal to 25 mm between the two materials. From the results of the chemical analysis by Energy Dispersive Spectroscopy (EDS), it is possible to confirm the existence of a gradual and continuous transition of chemical properties between the two materials, which is very similar to the desired transition in the process of powder separation. In particular, by analyzing the evolution of the concentrations of chromium (for AISI 316L) and cobalt (for 18Ni Maraging 300), a transition can be observed from maximum values corresponding to the zones of each material (on opposite sides of the area studied) to zero values at the end, where these elements are absent. This result is significant because it shows that the equipment developed in this work can prevent contamination in the different single material zones. Contamination is a well-known problem in the literature [151,152] that hinders the fabrication of functionally graded material components at the layer level using a traditional PBF-LB system (with a powder platform from below) and a blade/roller powder distribution method. In addition, as shown in Figure 51, the concentrations of these elements gradually diffuse within the transition zone created by the powder separation system, contributing to the strengthening of the interface [153]. The results of the EDS analysis shown in Figure 51, confirm a firm and favorable bond between the two materials, in agreement with what has been reported in the studies of Wei et al. [154] and Tan et al. [155]. Finally, it is important to note that the measurement values obtained from the three different samples overlap, indicating a uniform distribution of the different phases in the different samples prepared.

		Y position [mm]											
		Maraging		Gradient zone								AISI 316L	
		0 ÷ 2.5		2.5 ÷ 5	5 ÷ 7.5	7.5 ÷ 10	10 ÷ 12.5	12.5 ÷ 15	15 ÷ 17.5	17.5 ÷ 20	22.5 ÷ 25	25 ÷ 27.5	27.5 ÷ 30	
Cr wt%	AM-1	0.00	0.00	0.20	2.88	3.98	9.22	13.79	15.15	15.66	16.08	17.17	17.22	17.15
	AM-3	0.00	0.43	0.88	2.34	4.59	9.03	13.20	15.03	15.75	16.15	16.72	17.11	17.15
	AM-4	0.00	0.02	0.64	2.54	4.15	9.00	12.88	14.95	15.15	16.00	17.02	17.10	17.22
Mean		0.00	0.15	0.57	2.59	4.24	9.08	13.29	15.04	15.52	16.08	16.97	17.14	17.17
Co wt%	AM-1	9.89	9.91	9.66	7.77	7.57	4.91	2.33	1.80	1.33	1.25	0.70	0.10	0.00
	AM-3	9.80	9.67	9.54	8.43	7.15	4.97	2.87	1.79	1.54	1.17	0.85	0.32	0.00
	AM-4	9.55	9.50	9.52	8.22	7.22	5.00	2.55	1.89	1.25	1.22	0.66	0.15	0.00
Mean		9.75	9.69	9.57	8.14	7.31	4.96	2.58	1.83	1.37	1.21	0.74	0.19	0.00

Figure 51. Chemical composition analysis of the cross section of samples AM-1, AM-3 and AM-4, within the restricted area of the YZ plane.

Figure 52 depicts the transverse residual stress map of the non-heat-treated AM-2 specimen as measured by the contour method. Dashed lines indicate separating planes between different materials and the composition gradient zone. To aid in the visualization of residual stress trends throughout the specimen's thickness and in different material composition zones, five vertical scan lines were extracted from the residual stress map. Measurements were collected from specific longitudinal lengths in different zones of the specimen: 12 mm for the fully maraging zone, 24.5 mm for the interface between the maraging and composition gradient zones, 37 mm at the center of the gradient zone, 49.5 mm for the interface between the gradient zone and AISI 316L, and 62 mm for the fully AISI 316L zone (Figure 52(b)). The two-dimensional transverse stress map reveals tensile stress concentrations at the top and bottom of the specimen, balanced by compression in the center. Notably, the Maraging zone displays the highest tensile stresses, surpassing 800 MPa. Similarly elevated residual stress levels were reported by Bodner et al. in [134] in an intra-layer multi-material structure of Inconel 625 and AISI 316L. Furthermore, the upper region of the map exhibits tensile stresses that initiate from the left edge of the Maraging, extend throughout the gradient zone, and reduce approximately halfway towards the AISI 316L area, where a decrease to a stress-free region is found at the right edge of the specimen. The reduced residual

stresses in the austenitic steel may result from utilizing process parameters that were optimized for AISI 316L and applied uniformly throughout the AM-2 specimen [142]. Figure 52(b) clearly illustrates the C-shaped distribution of residual stresses along the thickness of the specimen. In addition, it can be seen that the 18Ni Maraging 300 is characterized by the most significant change from tensile at the surface to compressive at the center, from approximately 850 MPa to almost -200 MPa. The generation of residual stresses in the maraging steel using the PBF-LB method significantly depends on the process parameters used, which can also affect a partial transformation from austenite to martensite. De Baere et al. in [156] noted that for a nominal power density similar to that used in this work, an effective laser power of about 50 W, which is defined as the product of the nominal laser power and the laser absorption coefficient (between 0.3 and 0.5 for 18Ni Maraging 300 [157,158]), results in the development of a tensile stress field on the surface. Consequently, a subsequent heat treatment is necessary to induce the austenite-martensite transformation, which enhances the surface hardness [138] and modifies the residual stress state of the component.

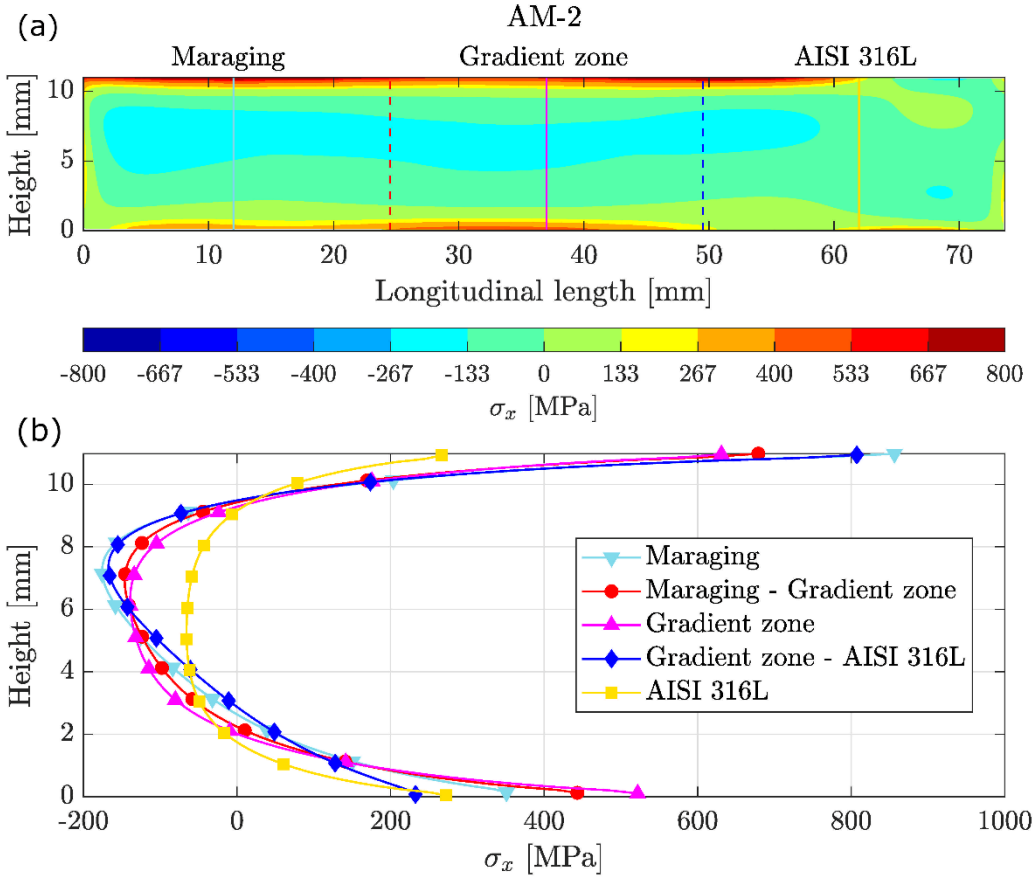

Figure 52. (a) Transverse residual stress map of sample AM-2. Dashed vertical lines indicate the separation planes between the materials. (b) Residual stresses throughout the height of the specimen extracted along the vertical scan lines in (a), respectively located at longitudinal lengths of 12 mm (Maraging), 24.5 mm (Maraging-Gradient zone), 37 mm (Gradient zone), 49.5 mm (Gradient zone-AISI 316 L) and 62 mm (AISI 316L).

The transverse residual stress map for the AM-3 sample, produced using a single scan speed of 180 mm/s throughout the whole specimen and then subjected to heat treatment, is shown in Figure 53. The maximum stress is now localized at the interface between the 18Ni Maraging 300 and the gradient zone, and is approximately 800 MPa after heat treatment. Moreover, the tensile zone at the specimen's top has reduced in size and is now concentrated in the mixed zone between the two materials. It extends about halfway across the base materials and gradually becomes stress-free towards the lateral edges. Additionally, the magnitude of the tensile zone in the lower section of the specimen has significantly decreased. Specifically, the highest local stress, which is observed in the gradient zone, has reduced from 520 MPa to nearly 280 MPa, resulting in a 45% decrease. After heat treatment, an overall reduction in peak residual stresses in the top surface of the specimen can be appreciated from Figure 53(b). Nevertheless, the 18Ni Maraging 300 base material displays the most significant relief in tensile residual

stresses, with surface compression now occurring up to 10 mm from the left lateral edge. Furthermore, as displayed in Figure 53(b), the residual stresses at the top surface of the maraging steel have decreased by almost 50 percent from 850 MPa to 450 MPa. Becker et al. [159] similarly reported decreased residual stress in maraging steel after solution annealing and subsequent precipitation age hardening heat treatments, as measured through hole drilling. Tensile residual stresses were reduced by as much as 70%.

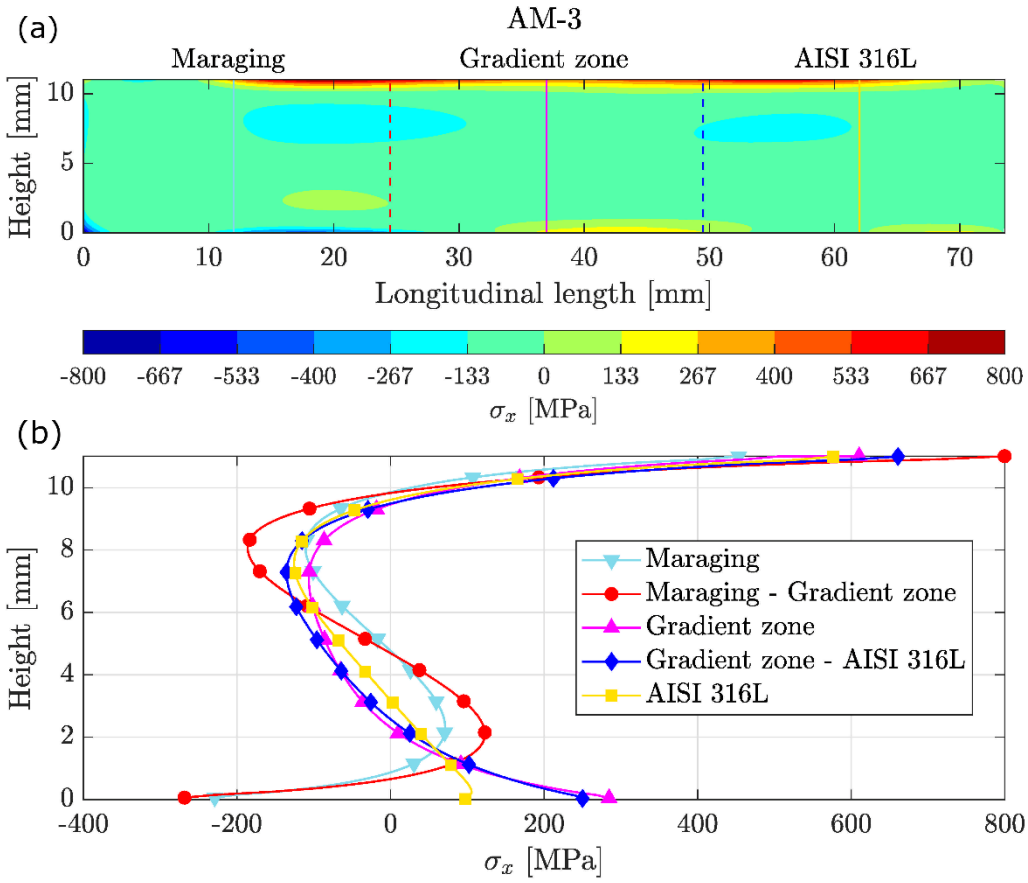

Figure 53. (a) Transverse residual stress map of sample AM-3. Dashed vertical lines indicate the separation planes between the materials. (b) Residual stresses throughout the height of the specimen extracted along the vertical scan lines in (a), respectively located at longitudinal lengths of 12 mm (Maraging), 24.5 mm (Maraging-Gradient zone), 37 mm (Gradient zone), 49.5 mm (Gradient zone-AISI 316 L) and 62 mm (AISI 316L).

Figure 54 and Figure 55 display the transverse residual stress maps for AM-1 and AM-4 specimens, respectively. Figure 54 illustrates that specimen AM-1, produced with two scanning speeds (refer to Figure 47), exhibits slightly reduced residual tensile stresses on the upper surface compared to specimen AM-3, particularly in the section composed entirely of 18Ni Maraging 300. The highest stress seen in Figure 54(b) occurs at the intersection of the gradient zone and AISI

316L, measuring approximately 700 MPa. This value is 12% lower compared to the cFGM sample produced utilizing a single scanning speed for all regions with distinct material compositions, as shown in Figure 53(b). From the results presented in Figure 55(a), it is evident that utilizing area-specific scan speeds for the three regions, each with different material composition, leads to reduced residual stresses across the component. This is especially noticeable on the upper surface of the specimen, where the area with the highest level of tensile stress is now of lower magnitude, ranging between 400 MPa and 550 MPa, and is also significantly smaller in extension. The highest tensile stress of approximately 560 MPa occurs at the interface between the 18Ni Maraging 300 and the region of composition gradient. Thus, by using material differentiated process parameters, the maximum residual stress was reduced by 30 percent compared to the one-set condition, with even greater reductions in other areas of the specimen.

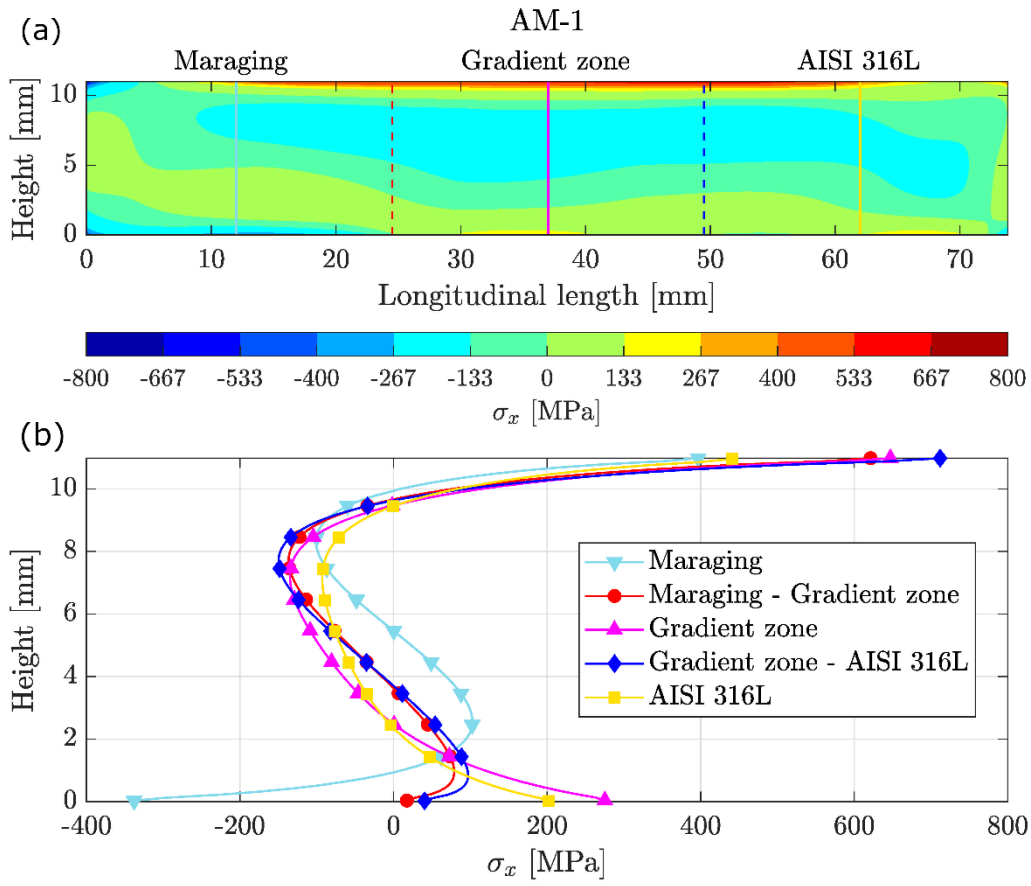

Figure 54. (a) Transverse residual stress map of sample AM-1. Dashed vertical lines indicate the separation planes between the materials. (b) Residual stresses throughout the height of the specimen extracted along the vertical scan lines in (a), respectively located at longitudinal lengths of 12 mm (Maraging), 24.5 mm (Maraging-Gradient zone), 37 mm (Gradient zone), 49.5 mm (Gradient zone-AISI 316 L) and 62 mm (AISI 316L).

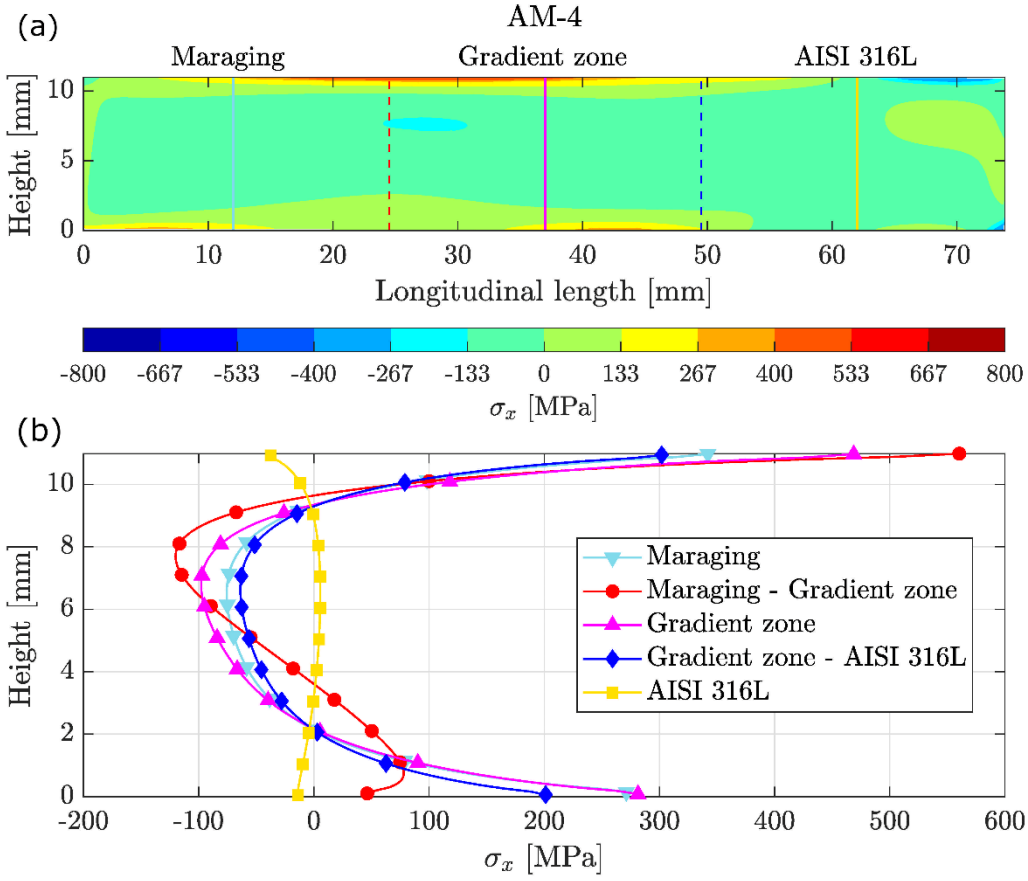

Figure 55. (a) Transverse residual stress map of sample AM-4. Dashed vertical lines indicate the separation planes between the materials. (b) Residual stresses throughout the height of the specimen extracted along the vertical scan lines in (a), respectively located at longitudinal lengths of 12 mm (Maraging), 24.5 mm (Maraging-Gradient zone), 37 mm (Gradient zone), 49.5 mm (Gradient zone-AISI 316 L) and 62 mm (AISI 316L).

Residual stress comparison along the lengthwise direction of the samples is shown in Figure 56. The data were obtained by analyzing contour method maps at locations of maximum stress. The measurements were extracted at a distance of 0.3 mm from the top surface of the specimen to eliminate any potential measurement errors that might occur in the surface area. It is acknowledged that the contour method is more susceptible to error than other measurement techniques in the perimetral region [14,29,97]. The residual stress fields in specimens AM-2 and AM-3, which were produced using a single scanning speed throughout, display fluctuations along the direction of variation in material composition, as depicted in Figure 56. Woo et al. found a similar oscillatory residual stress pattern along the composition change direction as a result of inadequate scanning strategies [110]. In their research work, since the material composition varied along the specimen's build direction, the intrinsic "cool-down phase" phenomenon in AM exacerbated this oscillatory pattern. Lastly, Figure 56 clearly shows that implementing material-

specific process parameters for the three composition zones, coupled with the appropriate heat treatment for the austenite-to-martensite transformation in 18Ni Maraging 300, leads to the AM-4 specimen having the least tensile residual stresses. Furthermore, the residual stress field exhibits a smoother and less oscillating pattern along the direction of the material's compositional change compared to using the same process parameters for the entire sample.

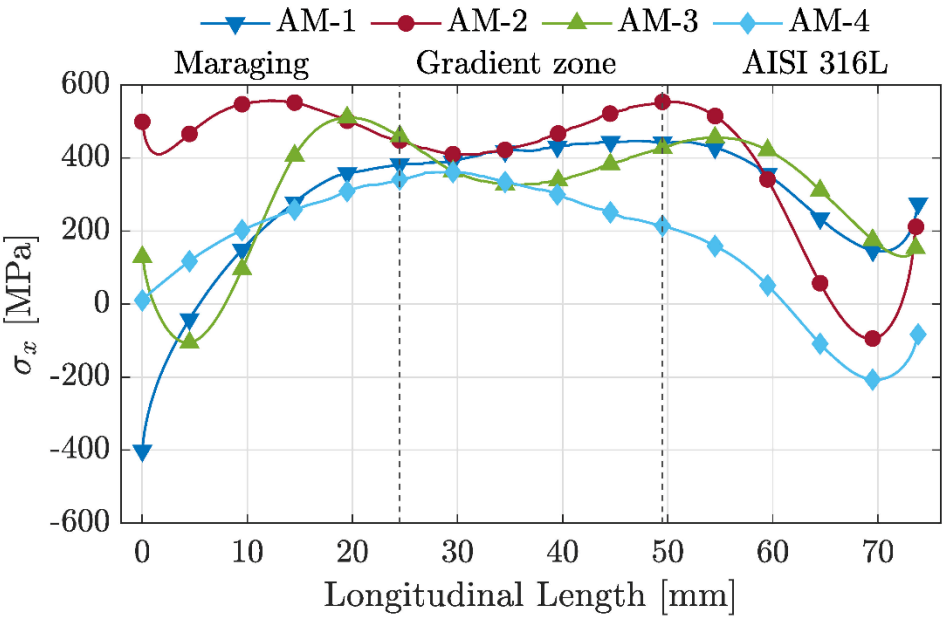

Figure 56. Comparison of residual stresses throughout the longitudinal length of the four specimens, extracted from the contour method stress maps along a horizontal line at 0.3 mm below the top surface.

2.3.6 Conclusions

In this study, the transverse residual stress field was measured in cFGM specimens composed of AISI 316L and 18Ni Maraging 300 by employing the contour method. These samples were manufactured via PBF-LB and the continuous variation in composition was realized within the same build layer. Furthermore, the study analyzed the influence of solution annealing and aging heat treatments on residual stresses. Finally, this research investigated the impact of adjusting the process parameters for each composition region, namely 18Ni Maraging 300, AISI 316L, and the continuous gradient zone between them, on the residual stress field, the discontinuities distribution and the chemical composition.

Optical microscopy revealed a gradual reduction in the number and extent of discontinuities from 18Ni Maraging 300 to AISI 316L. However, specimen AM-1, divided into two processing zones and fabricated utilizing different scanning

speeds, exhibited a significant concentration of porosity in the region where the processing parameters were changed. In contrast, specimen AM-4, which was manufactured with differentiated process parameters for each of the three composition zones, did not exhibit any concentration of discontinuities in regions where scan speeds varied.

The results of EDS analysis at the interface confirmed the high quality of metallurgical bonding between the two materials. Moreover, the trends in the transition region were gradual and continuous for all the different samples produced, exhibiting overlapping distributions.

Residual stress analysis, utilizing the contour method, indicated that in specimen AM-2, produced with a single scanning speed of 180 mm/s and without heat treatment, the residual stress field revealed tensile stress concentrations situated at the top and bottom surfaces. These were counterbalanced by compression at the center, and the most significant stress was identified on the top surface of 18Ni Maraging 300, measuring 850 MPa. Moreover, the utilization of heat treatment resulted in a decrease of peak residual stresses observed on the specimen's upper surface. And specifically, the base material 18Ni Maraging 300 experienced the largest stress relaxation, resulting in a nearly 50% decrease in maximum tensile stress, from 850 MPa to 450 MPa. Additionally, the use of two different scan speeds in case AM-1 resulted in a reduction of the maximum tensile stress to 700 MPa. Furthermore, in specimen AM-4, the maximum tensile stress was further lowered to approximately 560 MPa. Notably, a decrease in residual stresses throughout the component was observed. This was achieved through the utilization of three different process parameters for each of the three composition zones, along with appropriate heat treatment.

Chapter 3. Development of a Gaussian Process Regression based methodology for uncertainty estimation in hole drilling measurements

3.1 Introduction

In order to control residual stresses and introduce compression it is well known that surface treatments such as shot peening and laser shock peening (LSP) can be adopted[160,161]. Notably, LSP is increasingly employed in the aeronautical and aerospace industries as it produces deeper compressive residual stresses and has less impact on surface integrity with respect to conventional shot peening [161].

The relevance and the complexity of performing an accurate experimental analysis of the residual stresses within a material has led to the emergence of several measurement techniques. At the present time, incremental hole drilling (IHD) and X-ray diffraction (XRD) are well-established techniques for measuring surface and sub-surface residual stresses and are also ruled by standards [17,50]. As described in Chapter 1, material is removed through incremental drilling in the IHD process. Subsequently, when exploiting destructive methods, the measured strains and the residual stresses are related by an integral equation, thus an elastic inverse solution is needed to compute the residual stress field [162,163]. This integral relationship occurs due to the fact that the stresses are calculated in locations different from where released strains are measured. The integral method is by far the predominant calculation method [164–173]. It exploits calibration coefficients, determined by FE calculation and tabulated in ASTM E837-20 [17], which are related to hole diameter, strain gage rosette geometry and drilling depth.

However, the integral method is very sensitive to errors in measured data for two main reasons. The first is physical in nature, as strains are being measured only at the surface. Therefore, IHD is limited by the Saint Venant's Principle, which states that surface deformation response becomes insensitive to the relaxation of residual stresses as hole depth increases. Accordingly, at large hole depths, the difference in measured strains at successive depths becomes progressively smaller, hence the impact of strain measurements errors is amplified [164]. The second reason is related to the numerical instability of the inverse problem. For a high number of calculation steps, the calibration matrices become numerically ill conditioned, so for small errors in the measured strains there are much larger error in the calculated residual stresses [166,167].

Over the past three decades, a number of researchers have investigated the influence of errors on IHD measurements carried out using the integral method. Vangi studied the influence of strain and hole diameter errors on the uncertainties associated to the calculated residual stresses [168]. Schajer and Altus presented a method for estimating probability bounds associated to the computed residual stresses for both the integral and power series methods. In their methodology, they considered the uncertainties related to errors on strains, hole depth, hole diameter and material constants. Then, they identified errors on measured strains as the main source of uncertainty with the largest probability bounds [169]. Zuccarello found that the numerical conditioning of the calibration matrices is minimized by adopting a calculation step distribution in such a way that diagonal elements of the matrices are constant in magnitude. Therefore, strain measurement errors have less effect on residual stress magnitudes and accordingly stress uncertainty is lower [167]. Peral et al. [170] carried out a detailed uncertainty analysis, taking into account many sources of error, performing a Monte Carlo simulation to propagate uncertainties to residual stresses and corroborating results with the more conservative approach proposed by Schajer in [169]. Uncertainty propagation to residual stresses through Monte Carlo simulation was subsequently applied in several other papers, reaffirming that one of the main contributors to uncertainties in stresses was noise in measured strains, especially using the integral method [171,174,175]. Recently, Olson et al. [176] developed an uncertainty estimator that considers two crucial sources of uncertainties. The first is strain uncertainty, where errors arise owing to instrumentation errors, thermally induced strains and residual stresses induced by the drilling process itself [163,169]. Whereas the second uncertainty source originates from the selection of the regularization parameters, which can significantly influence the calculated stresses.

Nevertheless, another source of uncertainty associated with the numerical manipulation of experimentally measured strain data should be considered. Generally, the drilling steps where the strains are measured do not match the calculation steps of the integral method. Therefore, Vangi proposed to interpolate the measured or the transformed strains using a polynomial, such that the maximum deviation from experimental values is lower than the measurement error [168]. Thus, it is now common practice to smooth the strain data using a polynomial or a spline [171–174,177–180]. However, this process is hugely influenced by the user's experience in choosing the degree of the fitting polynomial or the amount of smoothing given by the spline. Consequently, the fit procedure has an impact on the calculated residual stresses due to the sensitivity of the integral method.

In this research investigation, a tool based on the Gaussian Process Regression (GPR) is implemented to assess the uncertainty associated with the strain fitting procedure [181]. A Gaussian process model is a probabilistic supervised machine learning framework, which provides uncertainty measures over the predictions. It describes a probability distribution over possible functions that fit a dataset, by assuming that these functions are jointly Gaussian distributed [182]. GPR is an emerging framework among machine learning practitioners, nonetheless it has also recently been applied in the field of experimental mechanics by Tognan et al. to model the uncertainty over the residual stresses when employing the contour method [183].

The present section of the thesis is focused on developing a methodology to quantify the strain uncertainty in IHD, taking into account the uncertainty associated to strain fitting. Moreover, strain uncertainties were propagated to the calculated residual stresses by exploiting Monte Carlo simulation [184]. To validate this methodology, a three-point bending calibration test was first used and then a laser shock peened AA 7050-T7451 specimen was considered as a case study [185]. Furthermore, the results were compared to those obtained using traditional polynomial fitting procedures and also to XRD measurements on an analogous LSP sample. The ability of the proposed probabilistic method to discriminate two different strain signal sources was also investigated. Finally, the developed methodology was used to investigate the impact of various laser shock peening process parameters on the residual stress of AA 7050-T7451 specimens.

3.2 Gaussian Process Regression and propagation of uncertainties in hole drilling

As already mentioned above, a GPR model can make predictions on input data and deliver measurements of uncertainty on those predictions. In IHD strain fitting, the incremental drilling depths can be considered as input training data, whereas the output are the measured strains by the three strain gauges. Given a dataset $D = \{(x_i, y(x_i), i \in \{1, \dots, n\})\}$, where n is the total number of samples in the dataset, x_i are the depth increments that can be aggregated in a vector of inputs X, and $y(x_i)$ are the noisy strain measurements of an unknown function $f(x)$ sampled at x_i. The measured strains $y(x_i)$ can be modelled as follows:

$$y(x_i) = f(x_i) + \epsilon, \qquad \epsilon \sim N(0, \sigma_n^2) \tag{14}$$

where $\epsilon \sim N(0, \sigma_n^2)$ is the noise in the measured strain data, which is modelled as a Gaussian distribution with zero mean and variance σ_n^2. A GPR is defined as a random distribution of functions such that any finite samples of functions have a joint Gaussian distribution [181]. A Gaussian process is completely specified by its mean function $m(x)$ and its covariance function $k(x, x')$, also called kernel function:

$$f \sim GP(m(x), k(x, x')) \tag{15}$$

Therefore in GPRs there is the possibility to explicitly model a mean function, which can offer advantages such as interpretability of the model, convenience of expressing prior information and analytical limitations. However, if no prior information is available, it is common to set the mean function $m(x) = 0$, considering that this is not a drastic limitation, since the mean of the posterior process is not constrained to be zero [181]. In GPR models, after selecting the prior mean and covariance, this prior information is updated in light of the training data by defining the posterior, which is used to make predictions on unseen data.

Considering the case in which the mean function of the GP is zero and that the y observations are affected by noise (equation (14)), in order to make predictions we need to compute the conditional probability distribution of f_* given y, where f_* is a set of function values corresponding to new unseen test set of inputs X_*. Exploiting the closure property of Gaussians, we obtain that the conditional distribution is still Gaussian. This is called posterior GP, having mean and variance given by:

$$\overline{f_*} = K_*^T [K + \sigma_n^2 I]^{-1} y \tag{16}$$

$$cov(f_*) = K_{**} - K_*^T [K + \sigma_n^2 I]^{-1} K_* \tag{17}$$

where K refers to training set covariances, K_* refers to training-test set covariances, K_{**} refers to test set covariances and I is the identity matrix. It can be noted that $cov(f_*)$ models the uncertainty regarding the predictions at X_*. Besides, the confidence intervals on the GPR predictions can also be obtained through this.

Figure 57(a) reports a visual representation of a prior GP not conditioned by any data point, where the black line indicates the mean function, initialized as $m(x) = 0$, the different shades of red are the deciles of the confidence interval of the GP distribution, and with solid colored lines are indicated 10 sample functions of

the GP distribution. Figure 57(b)-(d) displays posterior GPs conditioned on an increasing number of training data points, corresponding to the strains measured by the strain gauge rosette in the IHD measurement.

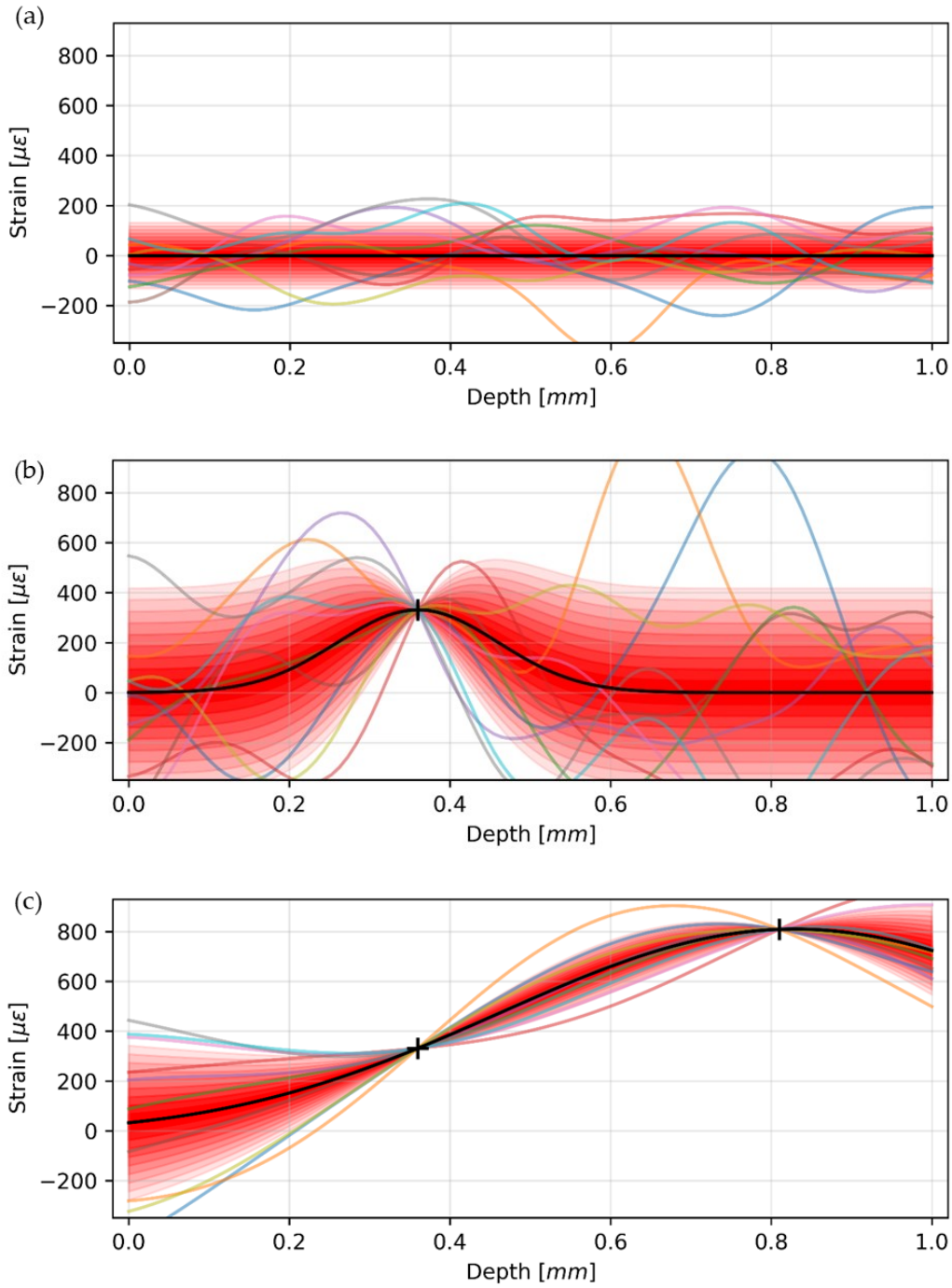

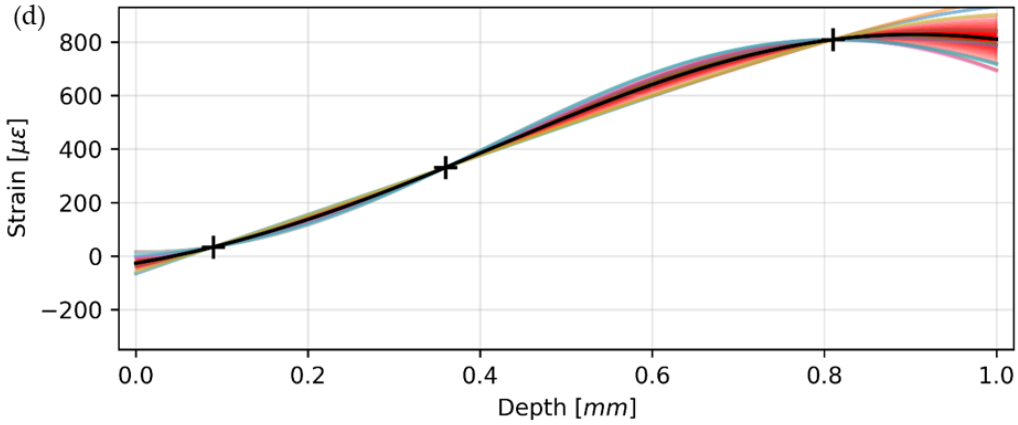

Figure 57. Visual representation of a Gaussian process modeling a one-dimensional function with increasing number of training data. With black line is indicated the mean, with different shades of red the deciles of the confidence interval of the GP distribution, and with colored solid lines are indicated 10 sample functions of the distribution. (a) Prior GP not conditioned on any data point; (b) Posterior GP with one training data point; (c) Posterior GP with two training data points; (d) Posterior GP with three training data points.

In this research investigation, the kernel function used to model the GPR is the radial basis function, also known as squared exponential kernel:

$$k_{SE}(x_i, x_j) = \sigma_f^2 \exp\left(-\frac{(x_i - x_j)^T (x_i - x_j)}{2l^2}\right) \quad (18)$$

where σ_f and l are hyperparameters. The vertical scale σ_f represents the vertical span of the function f, whereas, the horizontal scale l describes the correlation between the points x_i and x_j as a result of the decrease in their distances. The squared exponential kernel is broadly used and is a universal approximator, capable of approximating any arbitrary continuous function on any compact set of the input space [186].

In this work, since the additive noise ϵ present in the measured data depends on various factors as for instance instrumentation errors, thermally induced strains and residual stresses induced by the drilling process, the noise variance σ_n^2 was estimated by adding to the squared exponential kernel a white kernel [187]. It makes the assumption that the noise in the signal is independent and identically normally distributed, and it is defined as follows:

$$k_W(x_i, x_j) = \sigma_n^2 I \quad (19)$$

where σ_n^2 is the variance of the noise and I is the identity matrix. Therefore σ_n is another hyperparameter. Then we can define the total kernel function used as $K_T = k_{SE} + k_W$ and we can collect the hyperparameters in a column vector $\theta = [\sigma_f, l, \sigma_n]$.

The optimal hyperparameters are automatically determined by maximizing the log marginal likelihood [181]:

$$\log p(y \mid X, \theta) = -\frac{1}{2} y^T K_T^{-1} y - \frac{1}{2} \log|K_T| - \frac{n}{2} \log 2\pi \quad (20)$$

The GPR algorithm was implemented using the Python module scikit-learn [188]. To facilitate the search for optimal hyperparameters, the input dataset of depth increments and measured strains was given with measurement units of mm and $m\epsilon$, respectively. In the proposed methodology, by exploiting the posterior GPR, the strains were predicted for the points of the linear depth increments corresponding to the calculation steps of the integral method. Then the residual stress magnitudes were calculated following [17], without additional Tikhonov regularization. The GPR uncertainties, associated with each calculation depth, of the three strain measurements were propagated to the residual stress magnitudes through the use of Monte Carlo simulations [184]. Ten thousand trials were simulated, where for each trial the strain values were randomly drawn from the specific uncertainty distributions of each calculation depth.

3.3 Three-point bending calibration test

To evaluate the proposed methodology a preliminary three-point bending calibration test was conducted.

An annealed aluminum specimen ($E = 70\ GPa,\ \nu = 0.32$) was loaded in a three-point bending loading frame specially designed (Figure 58) in order to generate a known stress distribution. Annealing was performed in order to eliminate the residual stress state resulting from the manufacturing process. The specimen was supported at both ends, with a 50 mm overhang on each side, and was loaded in the center between the two supports. The distance l between the supports was 400 mm and the rectangular cross section dimensions were 25mm×10mm ($h \times b$). Thus, the normal stress varied linearly from compression to tension along the cross section dimension h of 25 mm, being zero at the neutral axis. A type B strain gauge rosette was installed at the central region of the upper surface,

in alignment with the applied load. The center of the rosette was positioned 3.3 mm away from the longitudinal axis of the sample, ensuring that the nearest edge was more than 1.5 times the diameter of the rosette gage circle ($D = 5.13mm$) [17].

The load was imposed by a load screw and was evaluated from the deflection of the beam, according to the formula:

$$f_{max} = \frac{FL^3}{48\,E\,I} = \frac{FL^3}{48\,E\left(\frac{bh^3}{12}\right)} \quad (21)$$

Where f_{max} is the deflection imposed to the beam, F is the load, L is the distance of the supports and I is the moment of inertia of the rectangular cross section equal to $bh^3/12$. The load screw, with a screw pitch of 1.25mm, was turned 12 times, resulting in a deflection of approximately 15 mm. Then, using the Navier bending formula, the normal stress is defined by:

$$\sigma = \frac{M}{I}y = \frac{\left(\frac{FL}{4}\right)}{\left(\frac{bh^3}{12}\right)}y = \frac{3FL}{bh^3}y \quad (22)$$

Where M is the bending moment on the cross section and y is the perpendicular distance to the neutral axis.

In the calibration test $y = 3.3\,mm$, therefore $\sigma \cong 250\,MPa$. This stress was constant along the depth from the surface $h \times l$, where IHD was performed.

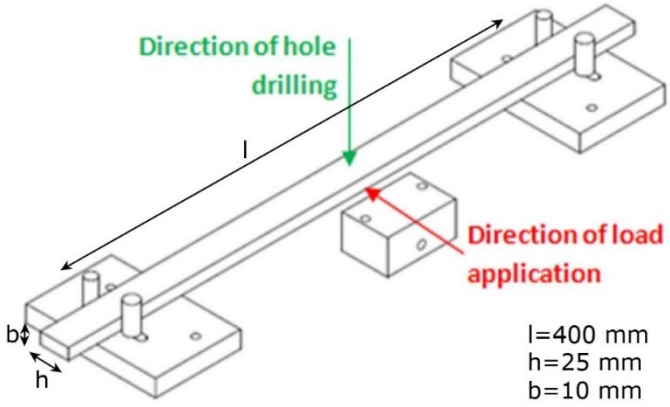

Figure 58. Three-point bending loading frame.

IHD was performed using the Sint Technology Hole Drilling system Restan MTS 3000 equipped with a compressed air unit controlling a pneumatic turbine

which achieves a rotation speed of 400000 rpm. Seven steps were drilled through increments of 0.05 mm using a tungsten carbide mill.

Figure 59 shows the strains measured by the three strain gauges. Figure 60 illustrates the GPR predictions over the measured strain data along with the associated uncertainties. Figure 61 reports the residual stress results calculated following [17] and with the strain uncertainties propagated to the stresses using Monte Carlo simulations. To provide better context for the obtained result, Figure 62 presents a comparison with the analytical solution, with results obtained without performing any fitting of the raw strains, and with results obtained using a fitting polynomial that minimizes the residuals between the fit itself and the measured strains. Figure 62 demonstrates the superior ability of the GPR method to match the analytical solution simulated in the laboratory.

However, after this initial calibration test to assess the feasibility of the GPR method, further validation is carried out in the following section on a real, rather than simulated, case study.

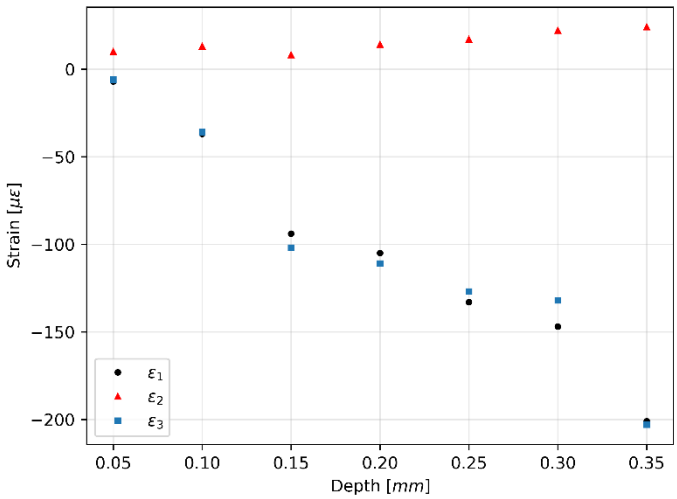

Figure 59. Measured strain variation with depth in the three strain gauges directions.

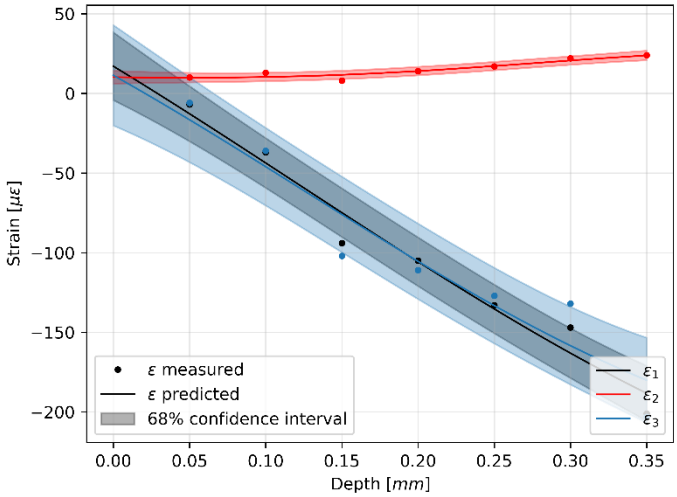

Figure 60. GPR fit of the measured strain data, with associated uncertainties shown as $\pm\mathbf{1}\boldsymbol{\sigma}$.

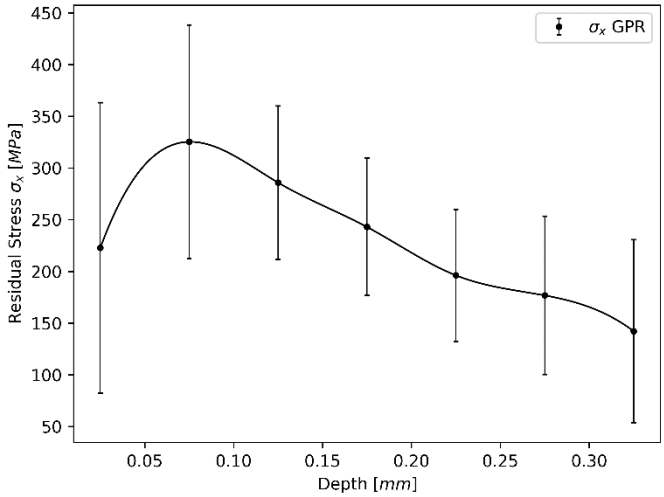

Figure 61. Residual stress distribution calculated using GPR, with the propagated uncertainties shown as $\pm\mathbf{1}\boldsymbol{\sigma}$.

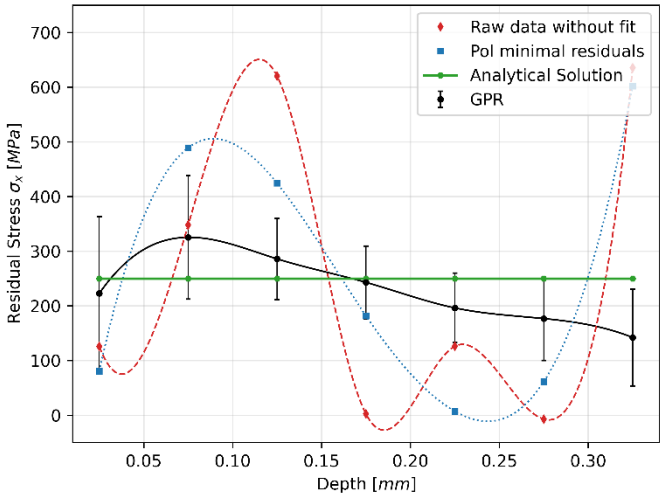

Figure 62. Comparison of residual stresses obtained by GPR method with the analytical solution, results obtained without smoothing the raw data, results obtained by using the fitting polynomial which minimized the residuals.

3.4 Case study: Laser shock peened sample

3.4.1 Specimen and laser shock peening process parameters

Squared samples 65 mm × 65 mm of aluminum alloy 7050-T7451 were machined from a rolled plate with a thickness of 30 mm. To achieve T7451 temper, the metal is solution heat-treated, stress relieved by controlled stretching and then stabilized by artificial overaging. The chemical composition and the mechanical properties of the material are given in Table 18 and Table 19, respectively. Prior to laser shock peening, the surface to be processed was ground. The LSP samples were realized using a YLF:Nd laser, the specification of which are reported in Table 20. The treatment was applied to an area of 35 mm × 35 mm placed in the middle of upper face of the specimens, as can be seen in Figure 63(a). Surfaces of the samples were laser shock peened setting the pulse frequency to 5 Hz, using a spot diameter of 3.5 mm attaining a nominal power density of 4.5 GW/cm^2. Prior to the peening process, a 30-40 μm thick commercial black paint layer and a film of 2 mm distilled water are used, respectively, as the sacrificial adhesive coating layer and the transparent confining layer. The sacrificial layer is limited to the surfaces of the treated areas only. An X-Y raster pattern was used as the peening strategy, where the LSP scan and step directions correspond to the x and y directions, respectively (Figure 63(b)). In the LSP process, an overlap of 30 percent was set between two adjacent laser spots, both along the scan and the step directions. Furthermore, 3

layers of peening were performed and an offset of 33 percent of a spot diameter was imposed between two consecutive layers.

Table 18. Chemical composition (wt%) of aluminum alloy 7050-T7451 [46].

Al	Cr	Cu	Fe	Mg	Mn	Si	Ti	Zn	Zr	Others
87.3 – 90.3	≤0.04	2.0 – 2.6	≤0.15	1.9 – 2.6	≤0.10	≤0.12	≤0.06	5.7 – 6.7	0.08 – 0.15	≤0.15

Table 19. Mechanical properties of aluminum alloy 7050-T7451 [46].

Young's Modulus (GPa)	Poisson's ratio	Yield strength (MPa)	Ultimate tensile strength (MPa)
71.7	0.33	469	524

Table 20. Laser specifications.

Laser source	Wavelength (nm)	Laser power (W)	Pulse energy range (J)	Pulse length range (nm)	Pulse frequency range (Hz)	Beam shape	Beam profile	Spot diameter range (mm)
YLF:Nd	1053	200	Up to 10	16 – 21	1 – 20	Round	Flattop	2 – 6

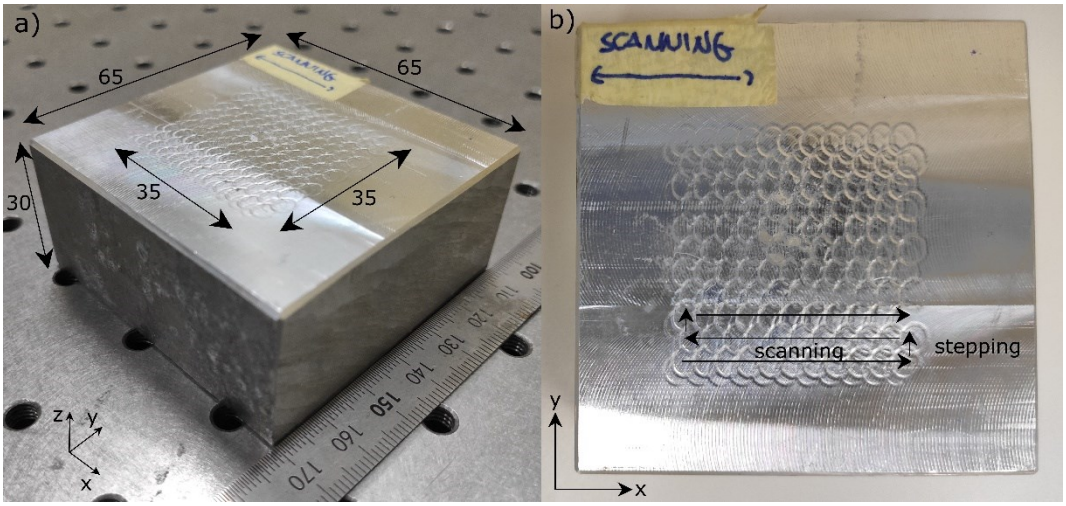

Figure 63. a) LSP samples dimensions; b) LSP scanning strategy. All dimensions are in mm.

3.4.2 Experimental set-up for incremental hole drilling measurements

IHD was performed using the Sint Technology Hole Drilling system Restan MTS 3000 equipped with a compressed air unit controlling a pneumatic turbine

which achieves a rotation speed of 400000 rpm. The strain evolutions during the IHD process are measured using a type B counterclockwise strain gauge rosette. This was installed in the center of the surface treated area, such that the "a" and the "c" grids were aligned to the LSP scan and step directions, respectively. The roughness, introduced by the LSP process, was evaluated within the limits specified by the rosette manufacturer for proper installation of the strain gauge rosette. TiAlN coated tungsten carbide with higher durability and toughness was used as the mill. The inverted cone end mill of 1.6 mm diameter was employed to cut the hole, which had a precise final diameter of 1.98 mm. A total of 20 drilling steps with a polynomial distribution were executed at a speed of 0.2 mm/min to attain a final hole depth of 1 mm. The IHD experimental set-up is shown in Figure 64.

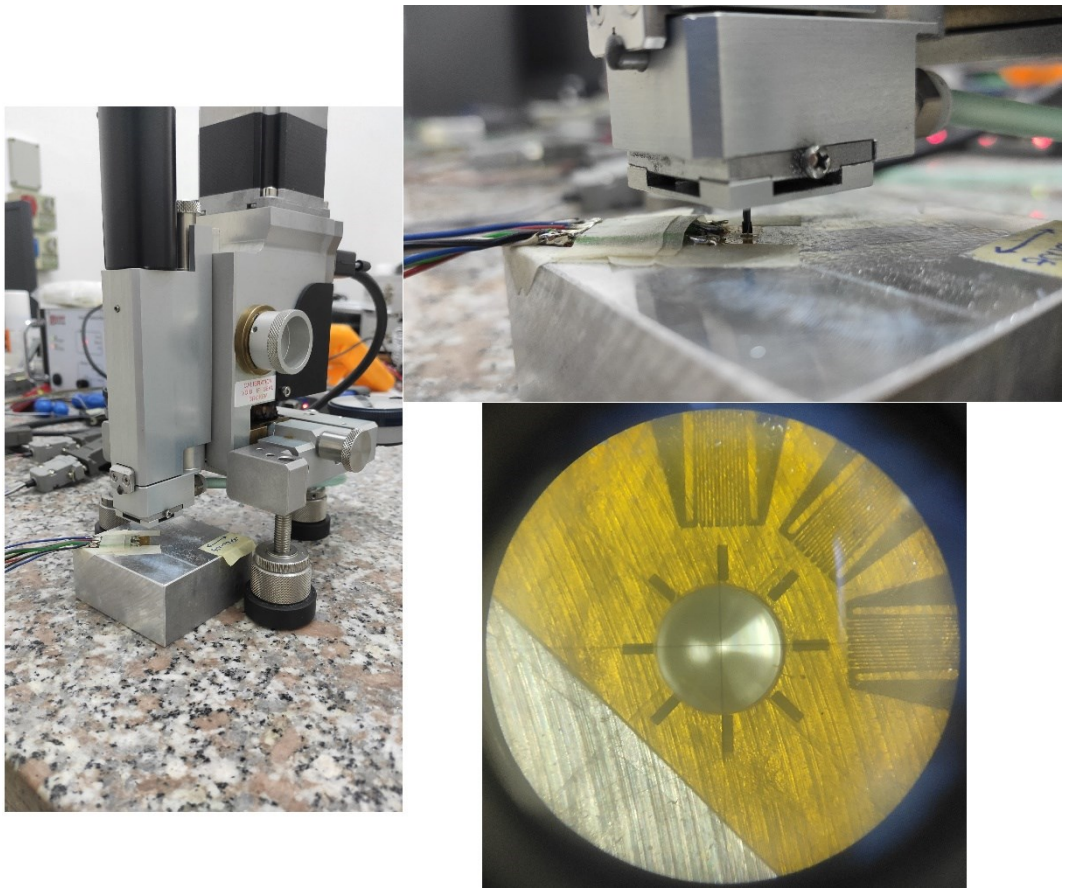

Figure 64. Incremental Hole Drilling set-up.

3.4.3 Validation of GPR method

To validate the proposed methodology, GPR residual stresses were compared with conventional approaches exploiting the integral method, in particular: results obtained by a strain fitting 4th degree polynomial; residual stresses derived from a 12th degree polynomial which minimized the residuals between the fit and the

measured strains, which is the degree of smoothing suggested by the Sint Technology commercial software; residual stresses measured by XRD on an analogous specimen conducted in [185].

Furthermore, to verify the ability of the proposed method to discriminate two different IHD measurements, two new sets of data were created by adding normal random noise with zero mean to the original strain measurements given by the three strain gauges. Then residual stress magnitudes were evaluated by exploiting GPR. First, a Gaussian noise with a standard deviation of 5 με was added, representing a signal within the strain measurement error. Secondly, a Gaussian noise with a 15 με standard deviation was added to the original data, representing an IHD measurement outside of the strain measurement error and that should lie outside of residual stress uncertainty bounds.

3.4.4 Results and discussion

Figure 65 shows the strain measurements by the three strain gauges. Whereas, Figure 66 illustrates the GPR predictions over the measured strain data along with the associated uncertainties, reported with a confidence level of 99.7% for visual clarity.

Table 21 reports the mean, minimum and maximum values of the uncertainties estimated by the GPR. It can be seen that the average uncertainty value between the three strain gauges is around 6 με. Furthermore, the minimum values of uncertainty, which are very close to the respective averages, for all the measured strains are located in the range of 0.1 to 0.85 mm of depth. Conversely, higher uncertainty values occur at the surface and the maximum is always found at depths greater than 0.85 mm. This could be attributed to the smaller number of measured strain data present in these two regions. Indeed, due to the polynomial distribution of the drilling depth increments, as the depth increases, the drilling step becomes larger, thus there are less measured strains in the deepest region of the hole. Therefore, in Figure 66 can be seen that GPR successfully fitted the outer data but with higher uncertainty.

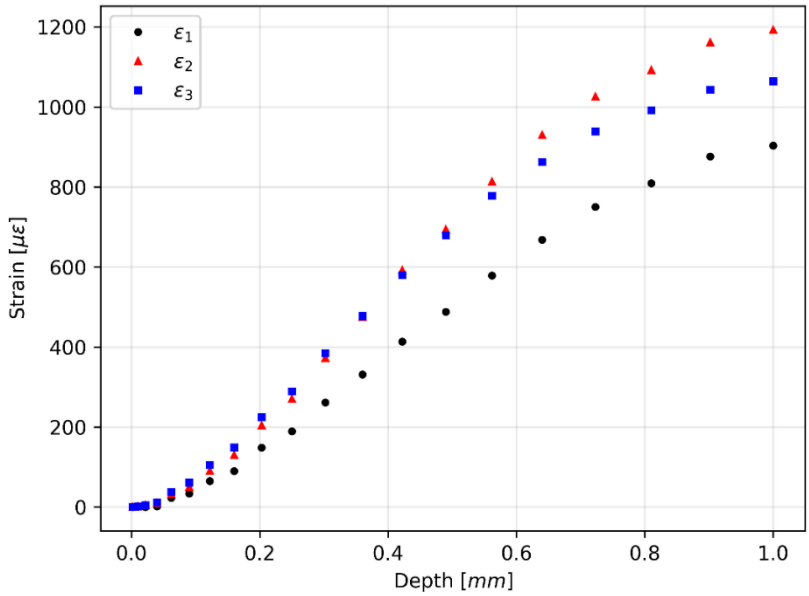

Figure 65. Measured strain variation with depth in the three strain gauges directions.

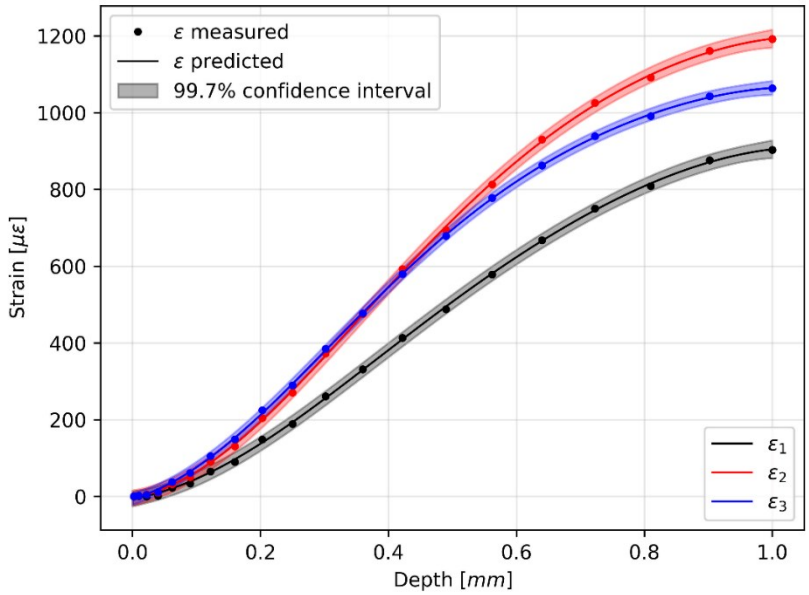

Figure 66. GPR fit of the measured strain data, with associated uncertainties shown as ±3σ.

Table 21. Mean, minimum and maximum values of uncertainties estimated by the GPR.

Mean σ_{ϵ_1} ($\mu\epsilon$)	Mean σ_{ϵ_2} ($\mu\epsilon$)	Mean σ_{ϵ_3} ($\mu\epsilon$)	Min σ_{ϵ_1} ($\mu\epsilon$)	Min σ_{ϵ_2} ($\mu\epsilon$)	Min σ_{ϵ_3} ($\mu\epsilon$)	Max σ_{ϵ_1} ($\mu\epsilon$)	Max σ_{ϵ_2} ($\mu\epsilon$)	Max σ_{ϵ_3} ($\mu\epsilon$)
6	6	5	6	6	5	8	8	6

Thereafter, the strain uncertainties were propagated to residual stresses through Monte Carlo simulations. Figure 67 depicts residual stresses along scan and

step directions, denoted as σ_x and σ_y, respectively. Stress uncertainties are reported with a confidence level of 68%. Figure 67 shows that an X-Y raster peening strategy induced compressive residual stresses which are slightly different in the two directions, especially for the first 0.4 mm from surface. Indeed, the compression along the step direction is greater than in the scan direction, reaching – 400 MPa at 0.3 mm deep. This behavior is also reported in [172] and by Correa et al. in [189], where it was found that residual stress magnitudes exhibit differences in perpendicular directions in LSP samples peened using a raster strategy, compared to those induced by adopting a random LSP pattern strategy. Furthermore, as can be seen in Figure 67, for both stress components, between 0.15 mm and 0.85 mm depth the uncertainty is below 19 MPa, notably in the middle depth range it reaches a minimum of 5 MPa. On the other hand, at the surface the uncertainty increases due to the higher strain uncertainty. As mentioned earlier, the strain uncertainty also takes into account errors related to the drilling process and, more generally, the strain measurement process, which are particularly critical at the surface. For this reason, a greater uncertainty on stresses is observed at surface [163,169,176]. In addition, in the deeper region of the hole, stress uncertainty increases significantly due to a combination of factors. Since twenty calculation steps are used, this uncertainty increase is due to the ill conditioning of the inverse problem in the integral method and is exacerbated by higher strain uncertainty detected by the GPR.

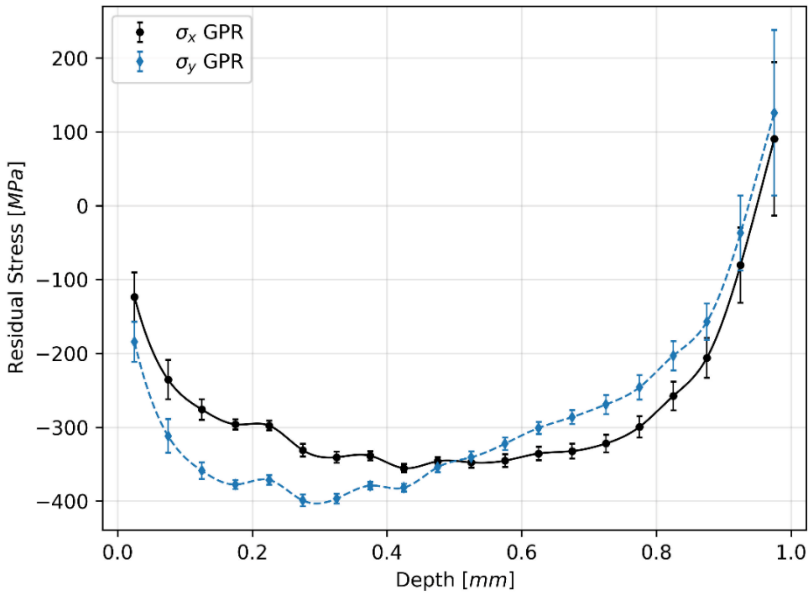

Figure 67. Residual stress distribution in scan (x) and step (y) directions, calculated using GPR, with propagated stress uncertainties shown as ± 1σ.

Furthermore, as shown in Figure 67, in the depth region between 0.275 mm and 0.425 mm, the magnitude of residual stresses along the step direction σ_y exceeds the ASTM limit of 80% of the material yield strength, under which plasticity effects around the hole are prevented, reaching a maximum of 85% [17]. It is worth noting that mechanical processes, like shot peening and laser shock peening, produce large local plastic strains and then induce material work-hardening which increases the local yield stress with respect to the nominal yield stress, as reported in [190]. In addition, in [190], where it is defined the limit for plasticity effect also adopted in the ASTM standard [17], it is reported that for shallower holes ($Z/D \leq 0.2$, where Z is the hole depth and D is the diameter of the gauge circle) the error of the elastic solution is less than 3-5 percent for residual stresses up to 90 percent of the material yield stress. These small errors can be neglected since similar errors are also due to the material yield stress uncertainty and errors in the measurement process. However, the correction procedure to include the effect of plasticity reported in [190] was applied, under the conservative assumption of uniform residual stresses equal to the maximum σ_y and the correspondent σ_x at a depth 0.51 mm, i.e., greater than the depth at which the last exceeding residual stress was measured. To apply the correction procedure the following data are used:

$$\sigma_y = -399\ MPa \tag{23}$$

$$\sigma_x = -331\ MPa \tag{24}$$

$$\sigma_{Yield} = 469\ MPa \tag{25}$$

$$R = 0.01 \tag{26}$$

$$\delta = \frac{D_0}{D} = \frac{1.98\ mm}{5.1\ mm} = 0.388 \tag{27}$$

$$\frac{Z}{D} = 0.1$$

(28)

where R is the strain-hardening ratio, δ is ratio between drilled hole and gauge circle diameters and Z/D is the ratio between stress depth and gauge circle diameter.

The biaxiality ratio is calculated as:

$$\Omega = \frac{\sigma_x}{\sigma_y} = 0.829$$

(29)

The equivalent residual stress at the plasticity onset is expressed as a function of the biaxiality ratio:

$$\sigma_{eq,i} = \sigma_{Yield} \frac{\sqrt{1 - \Omega + \Omega^2}}{3 - \Omega} = 200\ MPa$$

(30)

The elastically evaluated equivalent stress is defined as:

$$\sigma_{eq,el} = \sqrt{\sigma_{x,el}^2 + \sigma_{y,el}^2 - \sigma_{x,el}\,\sigma_{y,el}} = 370\ MPa$$

(31)

Where $\sigma_{x,el}$ and $\sigma_{y,el}$ are equal to σ_x and σ_y, which are the stresses calculated assuming that the material is linear elastic.

Then the related elastically-evaluated plasticity factor is obtained by:

$$f_{el} = \frac{\sigma_{eq,el} - \sigma_{eq,i}}{\sigma_{Yield} - \sigma_{eq,i}} = 0.63$$

(32)

The plasticity factor can be evaluated by the following function:

$$f_{el} = f + Wf^{\mu}$$

(33)

Where W and μ are functions of the dimensionless ratios δ and Ω, and of coefficients w_i, m_i $(i = 1, \dots, 12)$, which are dependent on the type of rosette, the strain hardening ratio and stress depth. Therefore with $\delta = 0.388$, $\Omega = 0.829$, $R = 0.01$ and $Z / D = 0.1$:

$$W = w_1\,\Omega^3\,\delta^2 + w_2\,\Omega^2\,\delta^2 + w_3\,\Omega\delta^2 + w_4\,\delta^2 + w_5\,\Omega^3\,\delta + w_6\,\Omega^2\,\delta + w_7\,\Omega\delta + w_8\,\delta + w_9\,\Omega^3 + w_{10}\,\Omega^2 + w_{11}\,\Omega + w_{12} = 0.413$$

(34)

$$\mu = m_1\,\Omega^3\,\delta^2 + m_2\,\Omega^2\,\delta^2 + m_3\,\Omega\delta^2 + m_4\,\delta^2 + m_5\,\Omega^3\,\delta + m_6\,\Omega^2\,\delta + m_7\,\Omega\delta + m_8\,\delta + m_9\,\Omega^3 + m_{10}\,\Omega^2 + m_{11}\,\Omega + m_{12} = 5.447$$

(35)

The plasticity factor can be then calculated as:

$$f_{el} = f + Wf^{\mu} \rightarrow \hat{f} = 0.6035$$

(36)

And the estimated equivalent residual stress $\hat{\sigma}_{eq}$ is obtained from the plasticity factor:

$$\hat{\sigma}_{eq} = \sigma_{eq,i} + \hat{f}\left(\sigma_{Yield} - \sigma_{eq,i}\right) = 362\ MPa$$

(37)

Finally the estimated principal stress components are:

$$\hat{\sigma}_y = \hat{\sigma}_{eq}\ \frac{1}{\sqrt{1 - \Omega + \Omega^2}} = -\,392\ MPa$$

(38)

$$\hat{\sigma}_x = \Omega\hat{\sigma}_y = -325\ MPa$$

(39)

The differences from the purely elastic estimated residual stresses are:

$$\frac{\sigma_y - \hat{\sigma}_y}{\sigma_y} \times 100 = 1.75\% \quad (40)$$

$$\frac{\sigma_x - \hat{\sigma}_x}{\sigma_x} \times 100 = 1.81\% \quad (41)$$

The error of the elastic solution, under conservative assumptions, is below 2 percent for both components of stresses, therefore it can be considered negligible [190].

Figure 68 and Figure 69 show comparisons of residual stresses measured by using: GPR methodology; a 4th degree fitting polynomial; a 12th degree fitting polynomial which minimized residuals; XRD [185]. The XRD results in [185] go down to 2.5 mm depth, but in Figure 68 and Figure 69 they are reported at the same depth as IHD measurements for visual clarity. XRD measurements, up to the depth of 1 mm, exhibit maximum errors in the scan and step directions equal to ±34.1 MPa and ±35 MPa, respectively [185]. It can be seen that, for both residual stress components, GPR results are smooth and do not need additional regularization. Conversely, using the higher degree polynomial, which minimized residuals, residual stress magnitudes exhibit a highly oscillating behavior and always lay outside of GPR uncertainty boundaries. Furthermore, the 4th degree fitting polynomial is in good agreement with GPR results, indeed it falls within uncertainty limits until 0.675 mm deep. Figure 68 shows an excellent agreement between GPR and XRD measurements with a maximum difference of less than 80 MPa until a depth of 0.875 mm. Conversely, in Figure 69 residual stresses along step direction measured by XRD exhibit a decrease of compression from 0.175 mm, increasing the difference with IHD measurements. However, an overall agreement occurs between the two different measurement methods, which further corroborates the GPR methodology, especially in the scan direction.

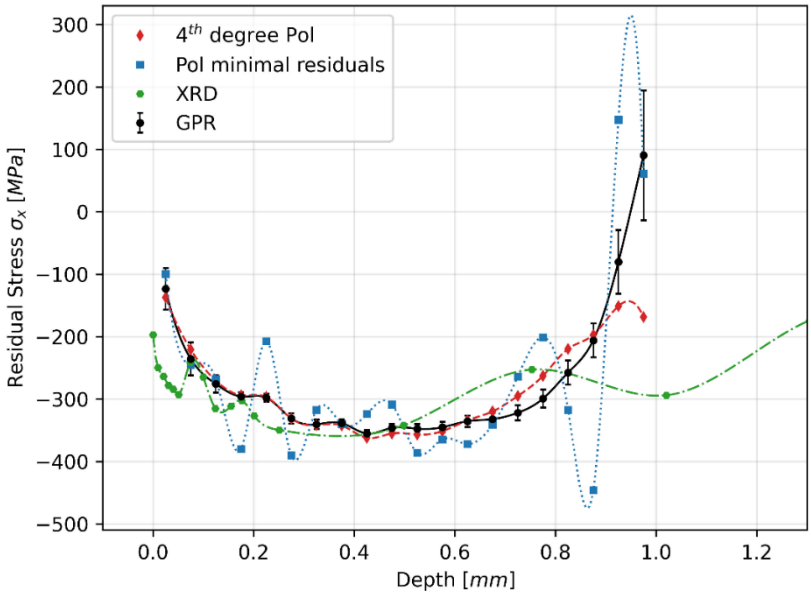

Figure 68. Comparison of residual stresses in scan (x) direction obtained by GPR method, by a 4th degree fitting polynomial, by a fitting polynomial of 12th degree which minimized the residuals, and by XRD [185].

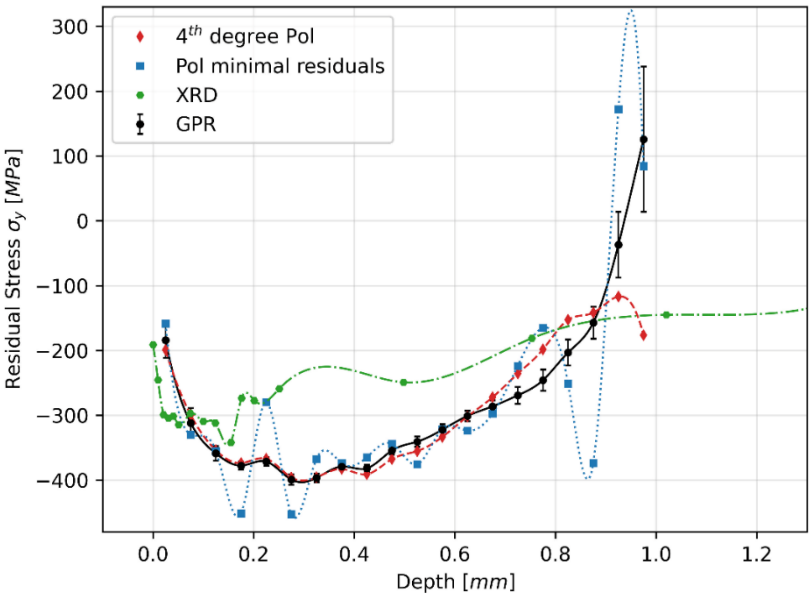

Figure 69. Comparison of residual stresses in step (y) direction obtained by GPR method, by a 4th degree fitting polynomial, by a fitting polynomial of 12th degree which minimized the residuals, and by XRD [185].

Figure 70 and Figure 71 illustrate the ability of the GPR methodology to correctly discriminate two different strain signal sources. They show residual stresses in scan and step directions, respectively. On the one hand, the original strain

signal with an added Gaussian noise with zero mean and a standard deviation of 5 με correctly lies within stress uncertainty bounds given by the GPR method. On the other hand, the strain signal with a noise of 15 με standard deviation falls outside of the uncertainty limits for almost every calculation step. Therefore, the GPR method properly identifies a strain signal that is within the strain measurement error as equal to the original strain signal, and correctly discriminate a strain signal that exceed this limit as different. Consequently, the GPR based approach does not introduce a level of smoothing that distorts the underlying stress solution, but successfully discriminate between different solutions.

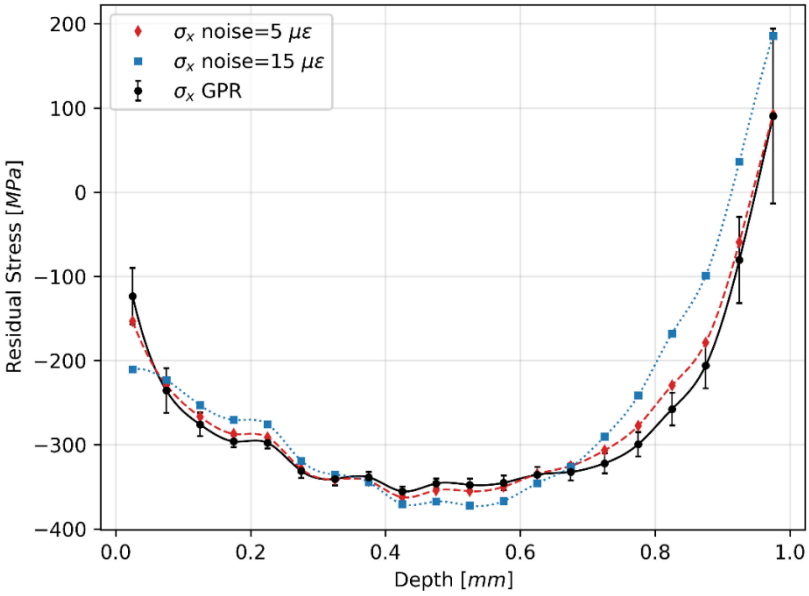

Figure 70. Comparison of GPR residual stresses in scan (x) direction with two different strain signal sources with Gaussian additive noise of 5 με and 15 με standard deviations.

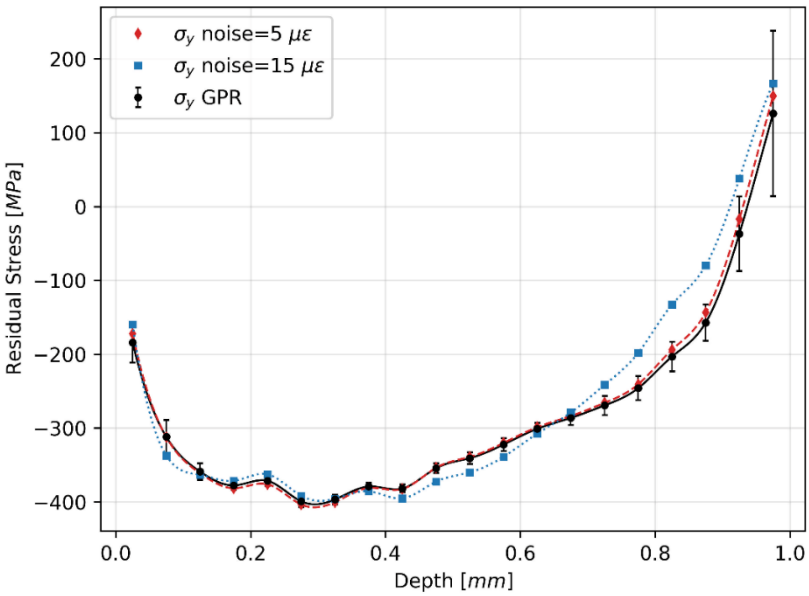

Figure 71. Comparison of GPR residual stresses in step (y) direction with two different strain signal sources with Gaussian additive noise of 5 με and 15 με standard deviations.

3.4.5 Conclusions

Generally, in IHD measurements with integral approach the drilling steps where strains are measured do not correspond to the stress calculation steps. Therefore, practitioners perform a fit of strain measurements using polynomials or splines introducing a source of uncertainty, associated with this fitting procedure (e.g. degree of polynomial or spline parameters), to the calculated stresses.

In this research work, a tool based on GPR was developed, which served two purposes. One is to fit the experimental strains during the IHD process and two is to estimate the uncertainties arising from this procedure. Moreover, GPR has the advantage that the optimal hyperparameters are automatically determined by maximizing the log marginal likelihood. Hence, the user's influence on the calculated residual stresses is minimized. Furthermore, GPR not only inferred uncertainty related to the fitting procedure, but also incorporated error sources connected to strain measurement procedure, e.g. instrumentation errors and drilling induced strains, by exploiting a compound kernel consisting of a squared exponential and a white kernel. In addition, a Monte Carlo simulation was carried out in order to propagate GPR uncertainties to the calculated residual stresses.

The GPR proposed methodology successfully fitted strain data of a laser shock peened AA 7050-T7451 specimen. From 0.15 mm to 0.85 mm deep residual stress magnitudes reported uncertainties between 5 MPa and 19 MPa. At the surface results exhibited a slightly higher level of uncertainty, whereas in the deeper region

of the hole stress uncertainties significantly increased both owing to higher strain uncertainty and to the ill conditioning of the inverse problem.

To corroborate the proposed methodology, the obtained residual stress magnitudes were compared to traditional polynomial fitting procedures for both scan and step directions. The GPR-based approach yielded smooth residual stress results without the need for further regularization. In addition, results were consistent with XRD measurements on a similar specimen, especially along scan direction. Nevertheless, for noncontinuous residual stress fields exhibiting discontinuities, such as those observed in composite materials, the proposed methodology may necessitate adaptation to accommodate the distinctive characteristics of such materials.

Finally, the proposed method demonstrated its ability to successfully discriminate between different strain signal sources that yield different stress solutions.

3.5 Case study: Effect of laser shock peening on residual stress of AA 7050-T7451

3.5.1 Materials and methods

In this case study the effect of laser shock peening on residual stress of AA 7050-T7451 was investigated by exploiting the methodology developed in the previous sections of the thesis. Twelve squared samples 65 mm × 65 mm were obtained from a rolled plate, consisting of seven samples that were 10 mm thick and five samples that were 30 mm thick. The chemical composition and the mechanical properties of the material are the same given in Table 18 and Table 19, respectively. The LSP treatment was performed on the same surface region using the same procedure as in the previous section's specimen, and the same YLF:Nd laser (Table 20). However, a series of parameters, namely nominal power density (NPD), laser spot diameter and the number of peening layers, were varied to investigate their influence on the final residual stress state of specimens with varying thicknesses. As shown in Table 22, the twelve samples can be divided into four groups where a limited number of parameters were varied, enabling a more direct comparison of the results.

Table 22. Thickness and LSP process parameters used for each specimen.

Sample	Thickness (mm)	Nominal power density $\left(\frac{GW}{cm^2}\right)$	Laser spot diameter (mm)	Number of layers
01	10	2.00	3.5	3
02	10	3.50	3.5	3
03	10	4.50	3.5	3
04	10	0.80	6.0	4
05	10	0.80	6.0	12
06	10	0.80	6.0	20
07	10	1.50	6.0	8
08	30	2.00	3.5	3
09	30	3.50	3.5	3
10	30	4.50	3.5	3
11	30	1.00	6.0	3
12	30	1.50	6.0	4

IHD was performed using the previously described Sint Technology Hole Drilling system Restan MTS 3000, achieving a rotation speed of 400000 rpm. Type B counterclockwise strain gauge rosettes were used to acquire the strain evolution for all the specimens. The rosettes were installed in the center of the LSP treated area, aligning "a" and "c" grids to the scan (x) and step (y) directions of the LSP strategy. TiAlN coated tungsten carbide mills were used for each test. A total of 20 drilling steps with a polynomial distribution were executed at a speed of 0.2 mm/min to attain a final hole depth of 1 mm.

After the IHD tests, the measured strains were fitted using the GPR methodology previously developed. Thus, the strains required for the integral method calculation for a 1 mm deep hole, corresponding to 20 linear depth increments, were predicted by utilizing the posterior GPR. The residual stress was computed according to [17]. The strain uncertainties provided by the GPR were propagated to the residual stress using Monte Carlo simulations, with a total of ten thousand trials.

3.5.2 Results and discussion

Figure 72 shows with filled circles the strain measurements by the three strain gauges of every rosette for specimens 01, 02 and 03 in panels (a), (c) and (e), respectively. The GPR predictions are indicated with a continuous colored line along with the associated uncertainties, reported with a confidence level of 99.7% for visual clarity. Table 23 reports the minimum, maximum and mean values of strain uncertainties for each of the three strain gauges in the installed rosettes. Sample 01 showed higher uncertainties in strains, which resulted in higher stress uncertainties, particularly for the last three measurement depths, compared to the other two samples. The residual stresses induced by laser shock peening are compressive in nature. However, as reported in Section 3.4 of the thesis, the field is not strictly equibiaxial in the scanning and stepping directions. This is due to the X-Y raster pattern strategy used, which generates a slight difference in the two residual stress components, compared to a random LSP pattern strategy [172,189]. Figure 73 presents a comparison of the residual stress induced by LSP in scan and step directions with varying NPD. Considering the scan direction, the maximum compressive stress is achieved when using an NPD of $2\ GW/cm^2$, resulting in $-350\ MPa$. However, at these LSP parameters, the depth at which the residual stress becomes zero is only $0.825\ mm$, whereas it is deeper than $1\ mm$ for higher NPD values. Furthermore, utilizing higher NPD values causes the maximum compressive residual stress to shift to greater depths. Meanwhile, residual stresses at the surface gradually decrease. This decrease can be attributed to a reverse plasticity effect resulting from over-peening, which causes a reduction in the magnitude of compressive residual stresses near the surface for thinner specimens [191,192]. Regarding the step direction, Figure 73 (b) shows residual stress fields that exhibit similar trends to those in the scan direction. However, in this case the effect of over-peening is more pronounced when using an NPD of $4.5\ GW/cm^2$. Indeed, once the maximum residual stress is reached, the slope of the rising part of the curve becomes steeper and is likely to reach the zero stress condition more rapidly.

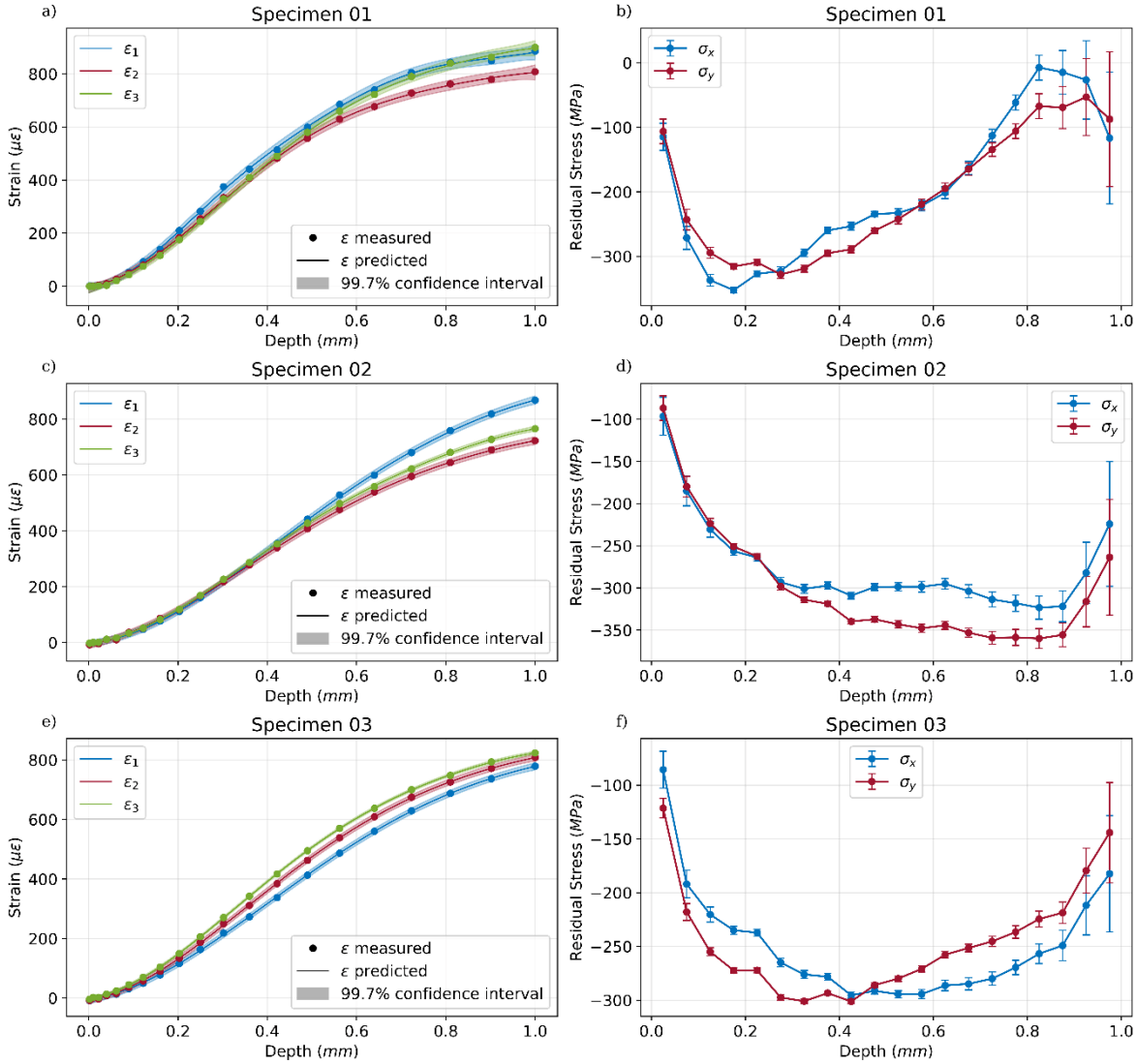

Figure 72. GPR fit of the measured strain data, with associated uncertainties shown as ±3σ for specimen 01 (a), specimen 02 (c) and specimen 03 (e). Residual stress distribution in scan (x) and step (y) directions, calculated using GPR, with propagated stress uncertainties shown as ±1σ for specimen 01 (b), specimen 02 (d) and specimen 03 (f).

Table 23. Minimum, maximum and mean values of strain uncertainties estimated by the GPR for each strain gauge in the installed rosettes. Standard deviation values are indicated in $\boldsymbol{\mu\epsilon}$.

Sample	Min σ_{ϵ_1}	Min σ_{ϵ_2}	Min σ_{ϵ_3}	Max σ_{ϵ_1}	Max σ_{ϵ_2}	Max σ_{ϵ_3}	Mean σ_{ϵ_1}	Mean σ_{ϵ_2}	Mean σ_{ϵ_3}
01	4	4	4	10	9	9	6	5	5
02	4	4	2	5	5	3	4	4	2
03	3	3	1	4	4	2	3	3	2
04	10	12	3	13	15	4	11	13	4
05	2	2	2	5	5	5	3	3	2
06	2	4	2	3	5	3	3	4	2
07	2	2	2	3	3	3	2	2	2
08	3	3	3	8	8	8	4	4	4
09	3	4	4	9	9	9	5	5	5
10	6	6	5	8	8	6	6	6	5
11	10	7	6	12	8	8	10	7	7
12	11	8	9	13	10	11	11	9	10

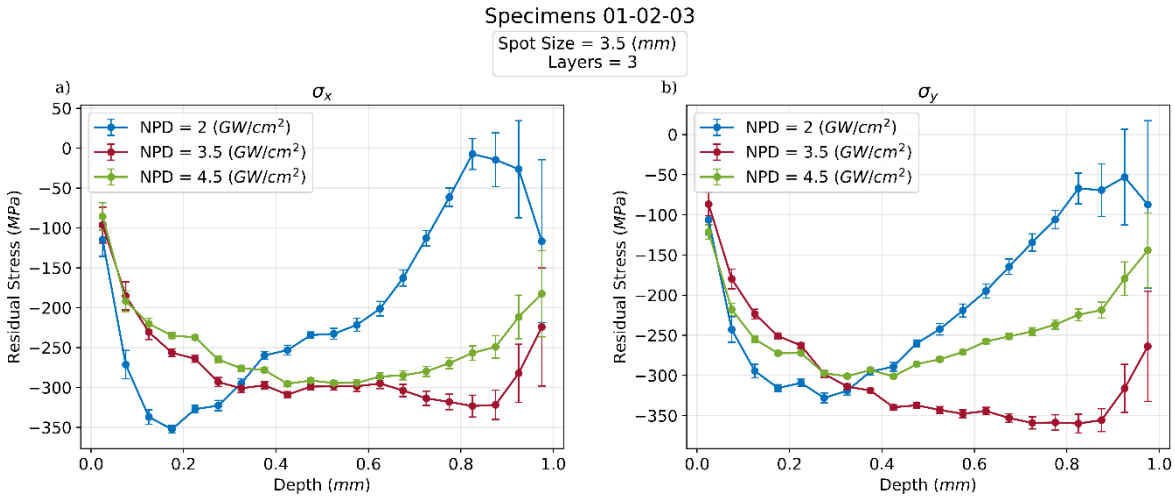

Figure 73. Comparison of the residual stress induced in 10 mm thick specimens with varying NPD; residual stress in scan direction (a) and in step direction (b).

Figure 74 displays the strain measurements and the GPR predictions for the second group of samples (04 to 07) with varying number of layers, in panels (a), (c), (e) and (g), respectively. The strain uncertainties predicted by the GPR are higher for specimen 04, as also reported in Table 23. This results in an overall higher uncertainty in the stresses (Figure 74(b)), particularly at the shallower depths where the residual stresses induced by the LSP process are of low magnitude. Additionally, this specimen experiences a difference in strain uncertainty between the three strain gages. In fact, along the strain gauge ϵ_3, which is aligned with the LSP step direction,

the average uncertainty is one third of the other two extensimeters (Table 23). This leads to a lower stress uncertainty in the step direction, even in the shallower depths. The residual stress measurements obtained using the GPR are presented in panels (b), (d), (f) and (h). By imposing a low NPD value of 0.8 GW/cm^2 for specimens 04, 05 and 06, and increasing the number of layers compared to specimens 01, 02 and 03, a lower compressive residual stress field is obtained. The maximum compression is $-240\ MPa$ in sample 06. Nevertheless, when compared to specimen 01, which was not subject to over-peening at the surface, the residual stresses in the specimens with a higher number of LSP layers show a less steep rise to zero. Or, in the case of specimen 04, an almost constant trend of residual stresses down to a depth of about 0.825 mm. This steady trend of the residual stress field is better observed in sample 07, where the number of layers is increased to 8 and the NPD value is raised from 0.8 to 1.5 GW/cm^2. Figure 75 illustrates a comparison of the residual stress induced by LSP in the scan and step directions for different number of layers, with the exception of sample 07 colored in light blue, which also has a higher NPD value. When examining specimens 04, 05, and 06, increasing the number of layers from 4 to 20 resulted in a higher maximum compressive residual stress. On the one hand, the maximum stress increased from $-150\ MPa$ to $-230\ MPa$ in the scan direction and from $-140\ MPa$ to $-240\ MPa$ in the step direction. On the other hand, the deeper part of the field exhibits a higher derivative, losing its steady nature. However, when both the NPD and number of layers are increased to 1.5 GW/cm^2 and 8 layers, respectively, the specimen (07) exhibits high maximum compressive residual stress, equal to $-240\ MPa$ in scan direction, and a steady trend along the depth up to 0.875 mm.

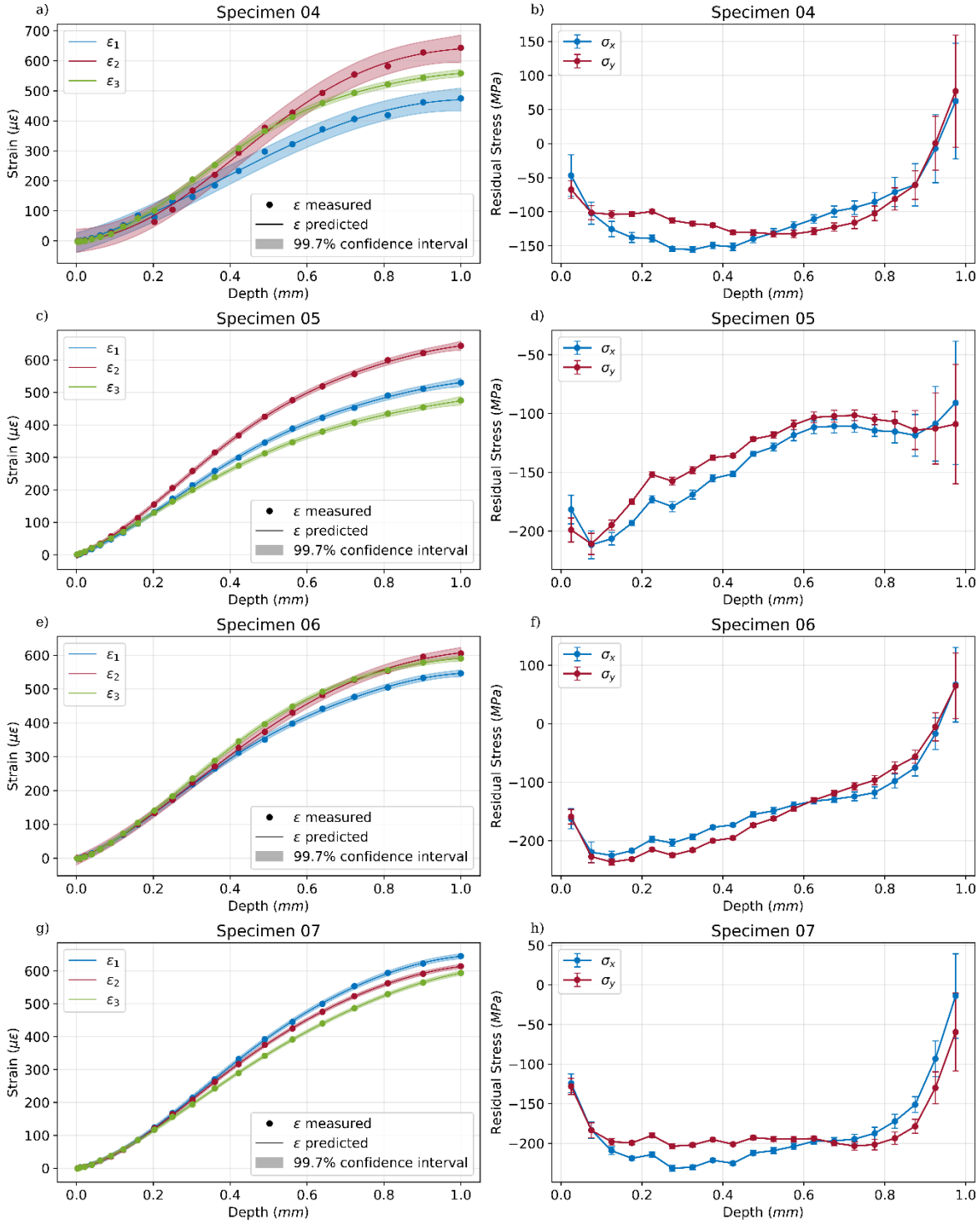

Figure 74. GPR fit of the measured strain data, with associated uncertainties shown as ±3σ for specimen 04 (a), specimen 05 (c), specimen 06 (e) and specimen 07 (g). Residual stress distribution in scan (x) and step (y) directions, calculated using GPR, with propagated stress uncertainties shown as ±1σ for specimen 04 (b), specimen 05 (d), specimen 06 (f) and specimen 07 (h).

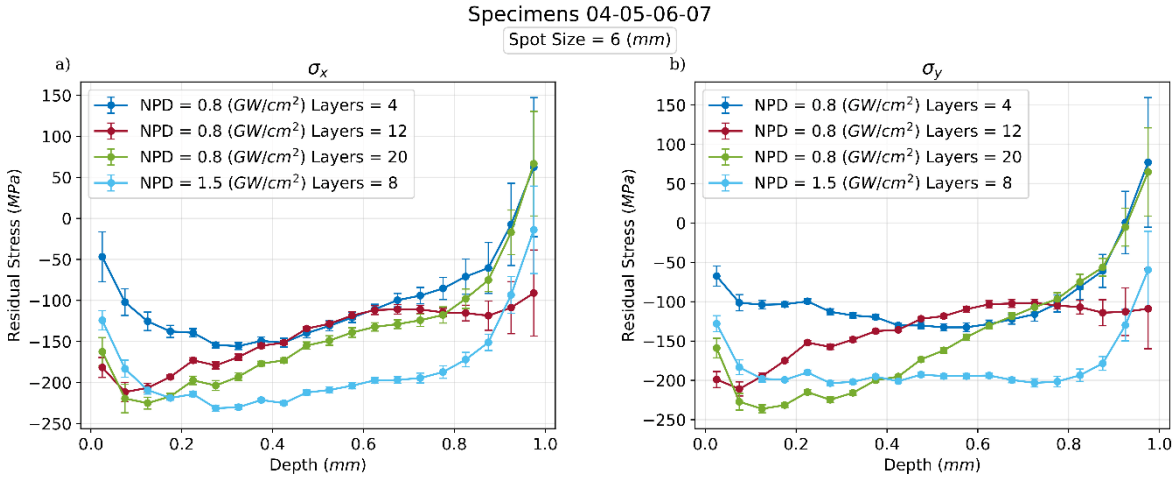

Figure 75. Comparison of the residual stress induced in 10 mm thick specimens with varying number of layers; residual stress in scan direction (a) and in step direction (b).

Figure 76 illustrates the strain measurements and the GPR predictions for the third group of samples (08, 09 and 10), with a thickness of 30 mm and increasing NPD, in panels (a), (c) and (e), respectively. The residual stress results along with the propagated uncertainties are reported in panels (b), (d), and (f). Also in this group of specimens, the equibiaxial residual stress state was not achieved, with differences in scan and step directions that are minor for specimen 08, but more significant for specimens 09 and 10. Figure 77 presents a comparison of the residual stress induced by LSP in scan and step directions with varying NPD. In contrast to the results obtained for the 10 mm thick specimens, the maximum compressive residual stress increased as NPD increased in this case. It reached $-400\ MPa$ along the step direction when NPD was imposed at 4.5 GW/cm^2. Additionally, the depth trend of residual stresses remained approximately constant up to 0.825 mm for all specimens.

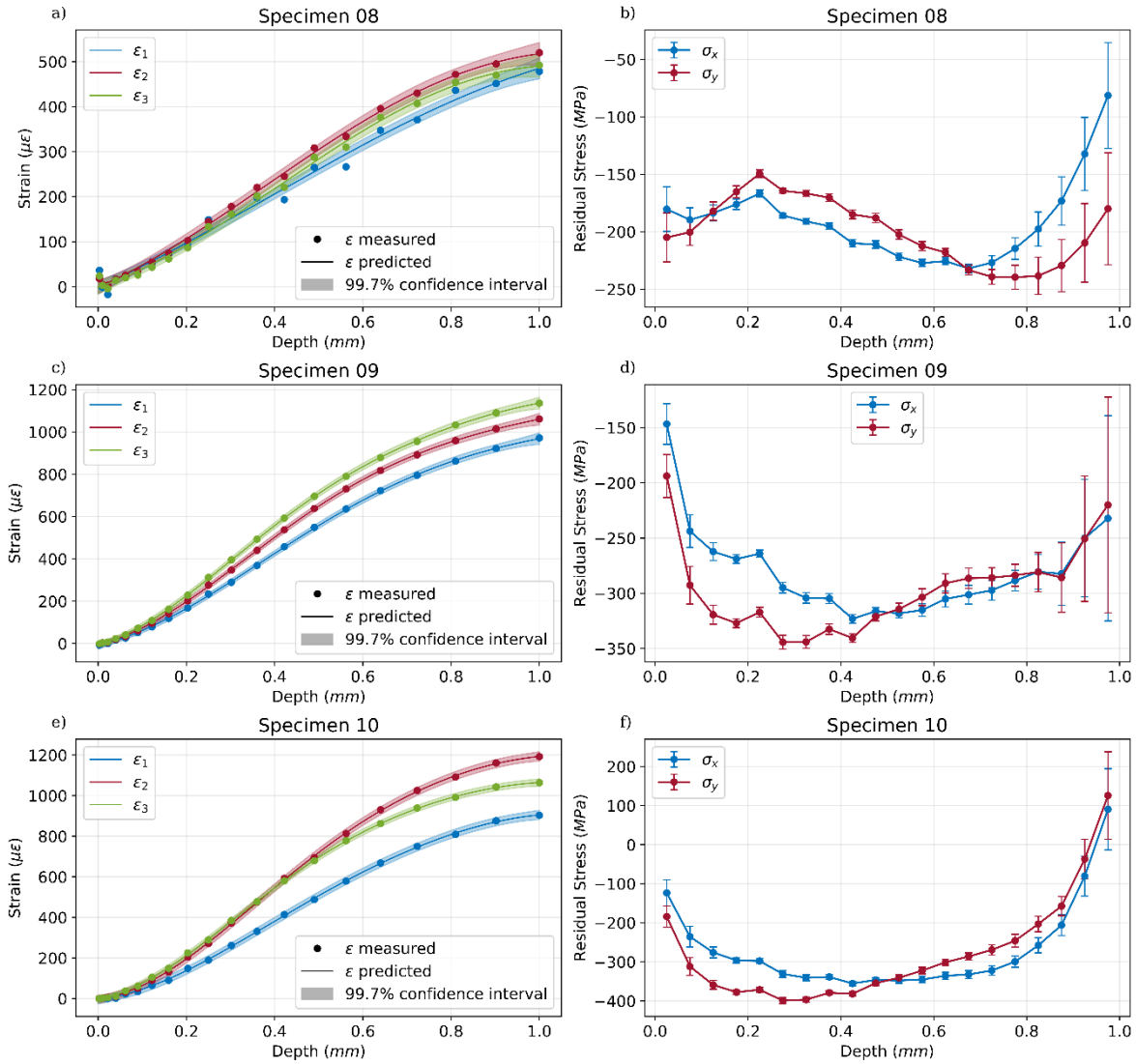

Figure 76. GPR fit of the measured strain data, with associated uncertainties shown as ±3σ for specimen 08 (a), specimen 09 (c) and specimen 10 (e). Residual stress distribution in scan (x) and step (y) directions, calculated using GPR, with propagated stress uncertainties shown as ±1σ for specimen 08 (b), specimen 09 (d) and specimen 10 (f).

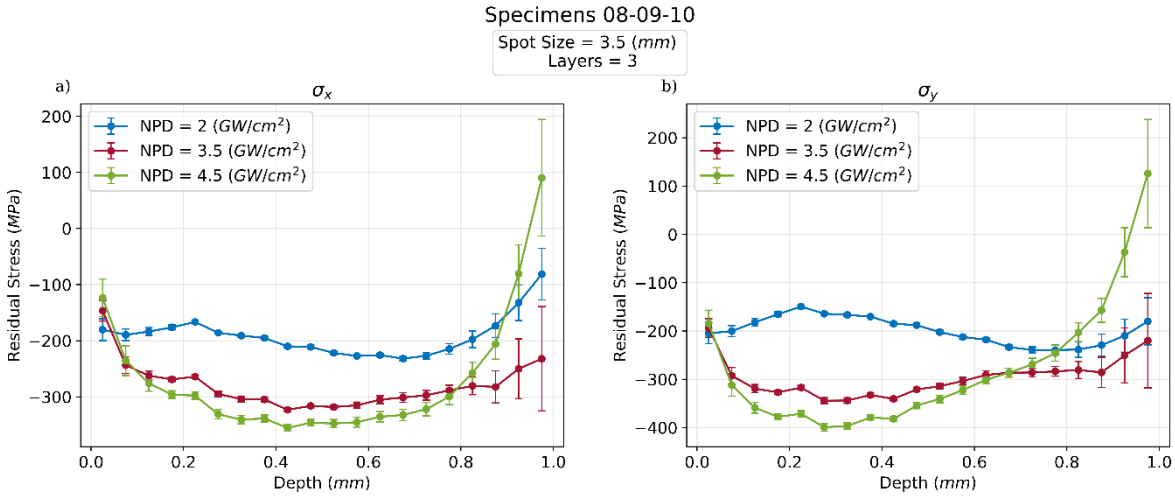

Figure 77. Comparison of the residual stress induced in 30 mm thick specimens with varying NPD; residual stress in scan direction (a) and in step direction (b).

For samples 11 and 12, which had a thickness of 30 mm, a lower NPD range of $1 - 1.5\ GW/cm^2$ was used. The LSP strategy was repeated for 3 and 4 layers, respectively. Figure 78 (a) and (c) and Table 23 show that both samples exhibited high strain uncertainty, resulting in higher stress uncertainty in the first measurement depths compared to other IHD tests (Figure 78 (b)-(d)), especially considering the low level of compressive residual stress field achieved using these LSP parameters. Specimen 11 is characterized by low compressive residual stresses, with a maximum of approximately $-100\ MPa$, exhibiting a constant trend up to $0.8\ mm$. By increasing the NPD value to $1.5\ GW/cm^2$ and repeating the LSP strategy for a 4th layer, the same residual stress trend is achieved in depth, but with a higher maximum compressive value of $-200\ MPa$, as shown in Figure 79. However, beyond a depth of $0.8\ mm$, the residual stresses become tensile with a steeper slope.

This is in line with the observations made on the previous samples. Increasing the number of layers results in higher maximum compression, but at the expense of achieving a constant residual stress field in depth. Similarly, increasing the NPD value leads to a more compressive residual stress field throughout the depth investigated with incremental hole drilling, but over-peening can occur, as observed in specimens 01, 02, and 03. Therefore, to achieve a constant compressive field for a depth of approximately $1\ mm$, it is necessary to properly couple the number of layers with the NPD values.

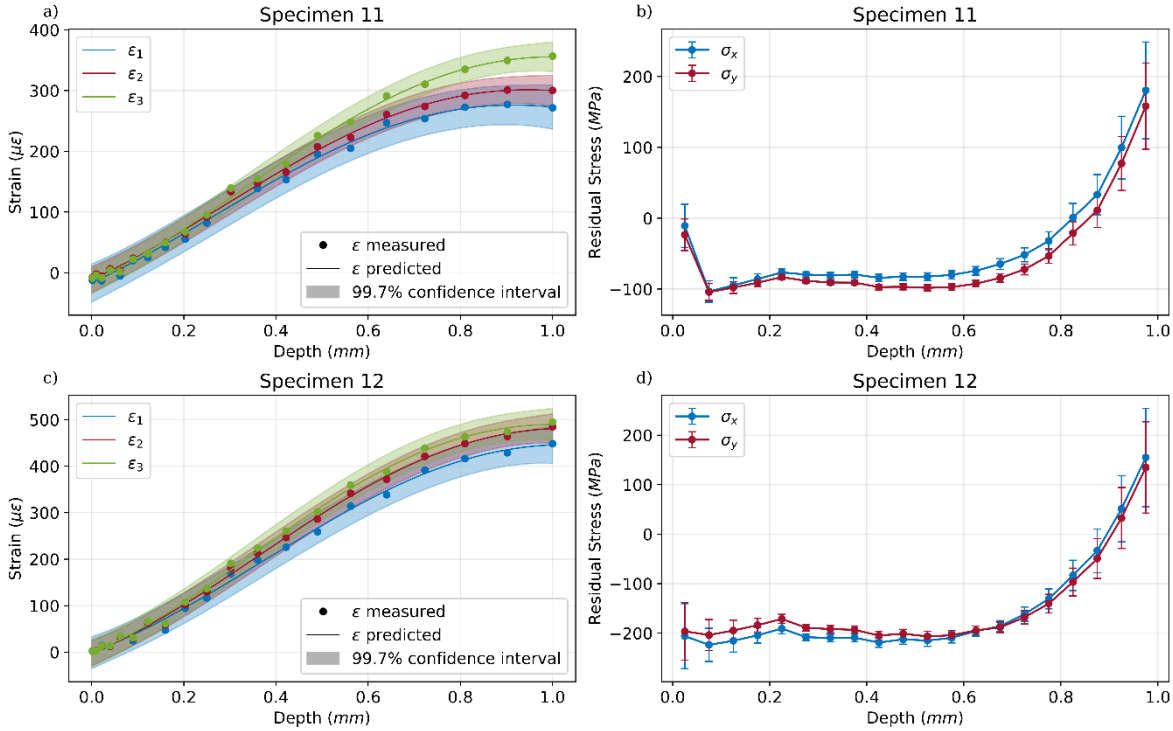

Figure 78. GPR fit of the measured strain data, with associated uncertainties shown as ±3σ for specimen 11 (a) and specimen 12 (c). Residual stress distribution in scan (x) and step (y) directions, calculated using GPR, with propagated stress uncertainties shown as ±1σ for specimen 11 (b) and specimen 12 (d).

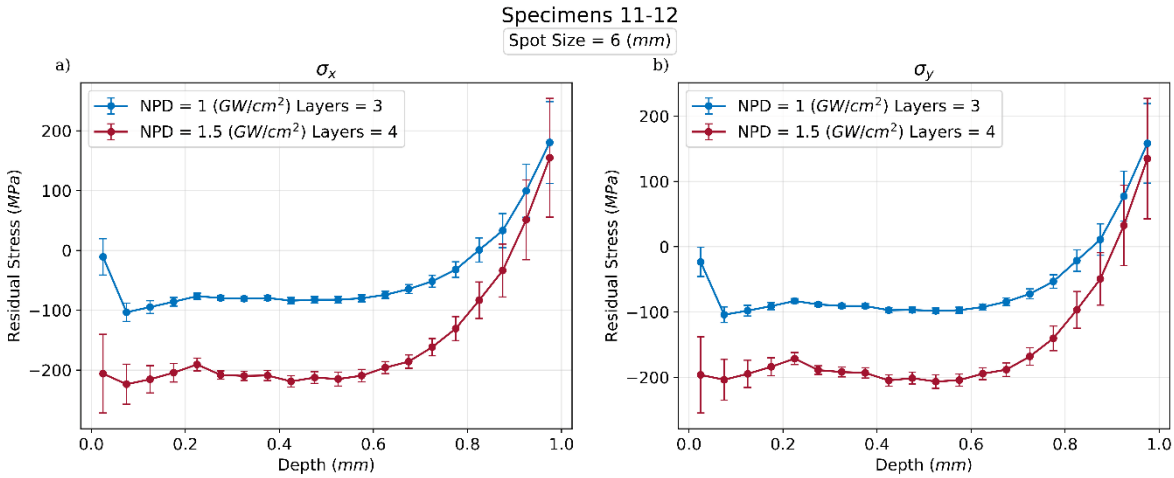

Figure 79. Comparison of the residual stress induced in 30 mm thick specimens with increasing both NPD and number of layers; residual stress in scan direction (a) and in step direction (b).

Finally, Figure 80 illustrates the influence of specimen thickness on residual stresses when using the same LSP process parameters. By employing a lower NPD value of 2 GW/cm^2, a spot size of 3.5 mm and repeating the LSP strategy for 3 layers, higher maximum compressive residual stress is obtained for a 10 mm thick specimen, reaching -350 MPa along scan direction. However, when applying these parameters to a 30 mm thick specimen, a maximum of less than -250 MPa is

achieved. This result could be attributed to a greater involvement of bulk material in the propagation of the LSP generated shock wave for the 30 mm thick specimen, which resulted in a lower maximum compressive residual stress, but for a greater depth. By increasing the NPD value to 3.5 GW/cm^2 and then to 4.5 GW/cm^2, the compressive residual stresses in the 10 mm thick specimen gradually decreased due to over-peening. Meanwhile, the 30 mm thick specimen exhibited a gradual increase in compressive residual stress (refer to Figure 80 (e) and (f)). Ultimately, it was characterized by more compression than the 10 mm thick specimen when subjected to 4.5 GW/cm^2. Therefore, to optimize the generated compressive residual stresses, lower NPD values should be used for thinner specimens and higher NPD values should be used for thicker specimens.

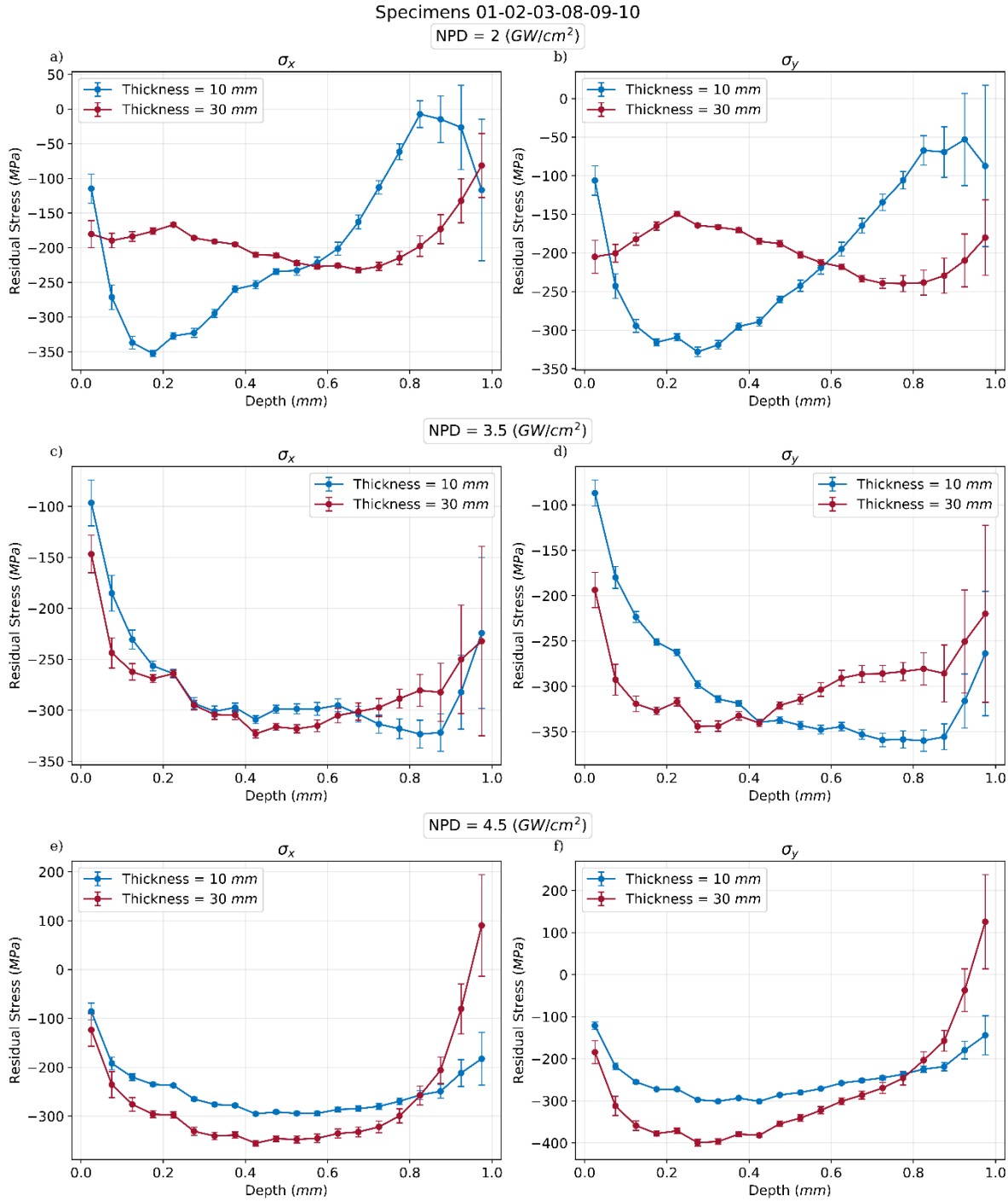

Figure 80. Comparison of the residual stress induced by using the same LSP parameters on specimens of varying thickness. Residual stresses generated along the scan (a, c, e) and step (b, d, f) directions using different NPD values. The NPD values used were $\mathbf{2\ GW/cm^2}$ for (a) and (b), $\mathbf{3.5\ GW/cm^2}$ for (c) and (d), and $\mathbf{4.5\ GW/cm^2}$ for (e) and (f).

3.5.3 Conclusions

In this section, the GPR based incremental hole drilling was successfully applied to investigate the effect of various LSP parameters on the residual stress

field generated in AA 7050-T7451 specimens.

The methodology based on GPR allowed for less conditioned measurements by the strain fitting procedure, and thus provided a measure of the uncertainty in the measured stresses. This revealed larger error bars in some of the measurements performed, especially in the very early incremental drilling steps, where IHD is more critical.

The experimental campaign studied the influence of NPD on the residual stress field for specimens of different thicknesses. The results showed that to optimize the compressive residual stress field, lower NPD values should be used for thinner specimens, while higher NPD values should be used for thicker specimens. This is because over-peening can occur in thinner specimens, causing a reduction in the magnitude of compressive stresses near the surface. Additionally, the study examined the impact of the number of layers for which the LSP strategy is repeated. Results showed that in 10-mm-thick specimens, increasing the number of layers while using a lower NPD (0.8 GW/cm^2) led to higher compressive values on the surface. Moreover, a compressive residual stress range of about $-200\ MPa$ constant to more than 0.825 mm depth was achievable by using an NPD of 1.5 GW/cm^2, which does not induce over-peening, and an intermediate layer number of 8. Finally, the same effect was observed for the 30 mm thick specimens. To achieve a constant compressive field for a depth of approximately 1 mm, it is necessary to appropriately match the number of layers with the NPD values.

Conclusions

This thesis work focuses on the development of residual stress measurement methodologies in advanced materials.

Initially, the measurement technique known as the contour method has been the subject of investigation. In this technique, accurate measurement of the contours of newly formed surfaces resulting from cutting is necessary to trace the residual stresses originally present in the part. Coordinate measuring machines are mainly used for this step of the contour method, but they are particularly slow and can significantly increase the time required to apply the contour method to large parts. To tackle this issue, a full-field optical technique known as fringe projection was used in this thesis work to measure the deformed surfaces. This technique reduced the time required for this phase to just a few seconds.

The contour method was then utilized to analyze various types of advanced multi-material joints.

At first, the technique was employed to measure the longitudinal residual stress field in three distinct thin laser-welded dissimilar joints. The aim was to identify the configuration with the lowest harmful tensile residual stresses. This configuration consisted of Ti-6Al-4V and Inconel 625 plates welded with two intermediate Vanadium and AISI 316L inserts. It was characterized by lower tensile residual stresses at the surface compared to the other two configurations.

Afterwards, a comprehensive experimental approach was developed to characterize the fatigue behavior of a laser welded joint consisting of Ti-6Al-4V and Inconel 625 plates with Vanadium and AISI 304 inserts. The surface residual stresses were evaluated initially using non-destructive X-ray diffractometry. The residual stresses in depth were measured using the contour method, which involved successive asymmetrical cuts to evaluate the entire residual stress field of the complex dissimilar joint under study. Afterward, fatigue and fracture surface characterization were conducted. The results were analyzed in conjunction with the previous residual stress measurements to highlight the correlations between fatigue strength, residual stresses, and fracture modes in order to better evaluate the mechanical reliability of such innovative and complex joints. Using this comprehensive approach, it was possible to identify at an early stage the most critical area, where fatigue failure was most likely to occur. Additionally, it was possible to understand that these joints had several defects, allowing for further optimization of the welding process for fatigue behavior.

The contour method was further used to study novel joints, fabricated through

additive manufacturing. Residual stresses were measured in functionally graded materials, which were built using PBF-LB. The composition change between the two materials of the joint was realized within the same layer, rather than between different layers. The study investigated FGM structures in AISI 316L and 18Ni Maraging 300. The impact on residual stresses of the post-process heat treatment required to improve the maraging hardness properties was evaluated. Finally, the implementation of material-specific process parameters for the three composition zones in conjunction with the heat treatment resulted in a reduction in the maximum residual stress of 35% and also a significantly lower residual stress field throughout the specimen.

The final chapter of the thesis presents a probabilistic machine learning framework, Gaussian Process Regression, which was used to develop an approach for estimating the uncertainty associated with the strain fit procedure in the residual stress measurement technique of hole drilling. The approach was first developed on a three-point bending calibration test. The proposed method was validated on a laser shock peened specimen in AA 7050-T7451. Standard fit procedures were used for comparison, and the method's ability to accurately distinguish between two sources of different strain signals was evaluated. The proposed GPR-based approach has been tested and validated exclusively in the context of hole drilling measurements on metallic materials. Nevertheless, research on the application of hole drilling to composite materials, particularly those based on polymers, remains limited. Consequently, future development may be directed towards the application and improvement of the GPR-based incremental hole drilling method for composite materials. Lastly, the methodology was utilized to examine the impact of nominal power density, laser spot diameter, number of peening layers, and specimen thickness on the residual stresses generated in AA 7050-T7451 specimens.

References

[1] P.J. Withers, H.K.D.H. Bhadeshia, Residual stress. Part 2–Nature and origins, Mater. Sci. Technol. 17 (2001) 366–375. https://doi.org/10.1179/026708301101510087.

[2] G.S. Schajer, C.O. Ruud, Overview of residual stresses and their measurement, Pract. Residual Stress Meas. Methods. (2013) 1–27.

[3] Y.F. Kudryavtsev, Residual Stress BT - Springer Handbook of Experimental Solid Mechanics, in: W.N. Sharpe (Ed.), Springer US, Boston, MA, 2008: pp. 371–388. https://doi.org/10.1007/978-0-387-30877-7_15.

[4] N.S. Rossini, M. Dassisti, K.Y. Benyounis, A.-G. Olabi, Methods of measuring residual stresses in components, Mater. Des. 35 (2012) 572–588.

[5] M.T. Hutchings, P.J. Withers, T.M. Holden, T. Lorentzen, Introduction to the characterization of residual stress by neutron diffraction, CRC press, 2005.

[6] P.J. Withers, H.K.D.H. Bhadeshia, Residual stress part 1 - Measurement techniques, Mater. Sci. Technol. 17 (2001) 355–365. https://doi.org/10.1179/026708301101509980.

[7] N.S. Rossini, M. Dassisti, K.Y. Benyounis, A.G. Olabi, Methods of measuring residual stresses in components, Mater. Des. 35 (2012) 572–588. https://doi.org/10.1016/j.matdes.2011.08.022.

[8] C. Casavola, R. Nobile, C. Pappalettere, A local strain method for the evaluation of welded joints fatigue resistance: The case of thin main-plates thickness, Fatigue Fract. Eng. Mater. Struct. 28 (2005) 759–767. https://doi.org/10.1111/j.1460-2695.2005.00909.x.

[9] C. Barile, C. Casavola, G. Pappalettera, C. Pappalettere, Remarks on residual stress measurement by hole-drilling and electronic speckle pattern interferometry, Sci. World J. 2014 (2014). https://doi.org/10.1155/2014/487149.

[10] Y. Lu, S. Wu, Y. Gan, T. Huang, C. Yang, L. Junjie, J. Lin, Study on the microstructure, mechanical property and residual stress of SLM Inconel-718 alloy manufactured by differing island scanning strategy, Opt. Laser Technol. 75 (2015) 197–206. https://doi.org/10.1016/j.optlastec.2015.07.009.

[11] C.E. Murray, I.C. Noyan, Applied and Residual Stress Determination Using X-ray Diffraction, in: G.S. Schajer (Ed.), Pract. Residual Stress Meas. Methods, First Edit, John Wiley & Sons, Ltd, Hoboken, NJ, USA, 2013: pp. 139–161.

[12] G.S. Schajer, P.S. Whitehead, Hole Drilling and Ring Coring, in: Pract. Residual Stress Meas. Methods, 2013: pp. 29–64.

[13] M.B. Prime, Cross-sectional mapping of residual stresses by measuring the surface contour after a cut, J. Eng. Mater. Technol. Trans. ASME. 123 (2001) 162–168. https://doi.org/10.1115/1.1345526.

[14] M.B. Prime, A.T. DeWald, The contour method, Pract. Residual Stress Meas. Methods. (2013) 109–138.

[15] G. Johnson, Residual stress measurements using the contour method, PhD

Dissertation, University of Manchester (United Kingdom), 2008.
[16] M.J. Roy, N. Stoyanov, R.J. Moat, P.J. Withers, pyCM: An open-source computational framework for residual stress analysis employing the Contour Method, SoftwareX. 11 (2020) 0–6. https://doi.org/10.1016/j.softx.2020.100458.
[17] ASTM E837-20, Standard Test Method for Determining Residual Stresses by the Hole-Drilling Strain-Gage Method, ASTM International, West Conshohocken, PA., (2020).
[18] M.B. Prime, A.L. Kastengren, The contour method cutting assumption: error minimization and correction, in: Exp. Appl. Mech., Springer, 2011: pp. 233–250. https://doi.org/10.1007/978-1-4419-9792-0_40.
[19] B. Ahmad, M.E. Fitzpatrick, Minimization and mitigation of wire EDM cutting errors in the application of the contour method of residual stress measurement, Metall. Mater. Trans. A. 47 (2016) 301–313. https://doi.org/10.1007/s11661-015-3231-7.
[20] F. Hosseinzadeh, P. Ledgard, P.J. Bouchard, Controlling the cut in contour residual stress measurements of electron beam welded Ti-6Al-4V alloy plates, Exp. Mech. 53 (2013) 829–839.
[21] Y.L. Sun, M.J. Roy, A.N. Vasileiou, M.C. Smith, J.A. Francis, F. Hosseinzadeh, Evaluation of errors associated with cutting-induced plasticity in residual stress measurements using the contour method, Exp. Mech. 57 (2017) 719–734. https://doi.org/10.1007/s11340-017-0255-5.
[22] Y. Traore, P.J. Bouchard, J. Francis, F. Hosseinzadeh, A novel cutting strategy for reducing plasticity induced errors in residual stress measurements made with the contour method, in: Press. Vessel. Pip. Conf., 2011: pp. 1201–1212. https://doi.org/10.1115/PVP2011-57509.
[23] F. Hosseinzadeh, Y. Traore, P.J. Bouchard, O. Muránsky, Mitigating cutting-induced plasticity in the contour method, part 1: experimental, Int. J. Solids Struct. 94 (2016) 247–253. https://doi.org/10.1016/j.ijsolstr.2015.12.034.
[24] Y. Traoré, F. Hosseinzadeh, P.J. Bouchard, Plasticity in the contour method of residual stress measurement, in: Adv. Mater. Res., 2014: pp. 337–342. https://doi.org/10.4028/www.scientific.net/amr.996.337.
[25] M.B. Prime, R.J. Sebring, J.M. Edwards, D.J. Hughes, P.J. Webster, Laser surface-contouring and spline data-smoothing for residual stress measurement, Exp. Mech. 44 (2004) 176–184. https://doi.org/10.1007/BF02428177.
[26] M.B. Toparli, M.E. Fitzpatrick, S. Gungor, Improvement of the contour method for measurement of near-surface residual stresses from laser peening, Exp. Mech. 53 (2013) 1705–1718. https://doi.org/10.1007/s11340-013-9766-x.
[27] M.D. Olson, A.T. DeWald, M.B. Prime, M.R. Hill, Estimation of uncertainty for contour method residual stress measurements, Exp. Mech. 55 (2015) 577–585. https://doi.org/10.1007/s11340-014-9971-2.
[28] M.B. Toparli, M.E. Fitzpatrick, Development and application of the contour

method to determine the residual stresses in thin laser-peened aluminium alloy plates, Exp. Mech. 56 (2016) 323–330. https://doi.org/10.1007/s11340-015-0100-7.

[29] F. Hosseinzadeh, J. Kowal, P.J. Bouchard, Towards good practice guidelines for the contour method of residual stress measurement, J. Eng. 2014 (2014) 453–468. https://doi.org/10.1049/joe.2014.0134.

[30] L. Shi, A.H. Price, W.N. Hung, Use of contour method for welding residual stress assessment, Procedia Manuf. 26 (2018) 276–285. https://doi.org/10.1016/j.promfg.2018.07.036.

[31] J. Kelleher, M.B. Prime, D. Buttle, P.M. Mummery, P.J. Webster, J. Shackleton, P.J. Withers, The Measurement of Residual Stress in Railway Rails by Diffraction and other Methods, J. Neutron Res. 11 (2003) 187–193. https://doi.org/10.1080/10238160410001726602.

[32] Y. Zhang, S. Ganguly, L. Edwards, M.E. Fitzpatrick, Cross-sectional mapping of residual stresses in a VPPA weld using the contour method, Acta Mater. 52 (2004) 5225–5232. https://doi.org/10.1016/j.actamat.2004.07.045.

[33] C. Liu, X. Yi, Residual stress measurement on AA6061-T6 aluminum alloy friction stir butt welds using contour method, Mater. Des. 46 (2013) 366–371. https://doi.org/10.1016/j.matdes.2012.10.030.

[34] C.R. D'Elia, M.R. Hill, M.E. Stender, C.W. San Marchi, Residual Stresses at Critical Locations in Additively-Manufactured Components, in: Residual Stress. Thermomechanics Infrared Imaging Inverse Probl., Springer, 2020: pp. 49–57. https://doi.org/10.1007/978-3-030-30098-2_8.

[35] G. Casalino, A. Angelastro, P. Perulli, C. Casavola, V. Moramarco, Study on the fiber laser/TIG weldability of AISI 304 and AISI 410 dissimilar weld, J. Manuf. Process. 35 (2018) 216–225. https://doi.org/10.1016/j.jmapro.2018.08.005.

[36] M.B. Prime, T. Gnäupel-Herold, J.A. Baumann, R.J. Lederich, D.M. Bowden, R.J. Sebring, Residual stress measurements in a thick, dissimilar aluminum alloy friction stir weld, Acta Mater. 54 (2006) 4013–4021. https://doi.org/10.1016/j.actamat.2006.04.034.

[37] H. Jafari, H. Mansouri, M. Honarpisheh, Investigation of residual stress distribution of dissimilar Al-7075-T6 and Al-6061-T6 in the friction stir welding process strengthened with SiO2 nanoparticles, J. Manuf. Process. 43 (2019) 145–153. https://doi.org/10.1016/j.jmapro.2019.05.023.

[38] P. Xie, H. Zhao, Y. Liu, Measuring residual stresses in linear friction welded joints composed by dissimilar titanium, Sci. Technol. Weld. Join. 21 (2016) 351–357. https://doi.org/10.1080/13621718.2015.1115158.

[39] C. Zhang, A.A. Shirzadi, Measurement of residual stresses in dissimilar friction stir-welded aluminium and copper plates using the contour method, Sci. Technol. Weld. Join. 23 (2018) 394–399. https://doi.org/10.1080/13621718.2017.1402846.

[40] H.C. Chen, A.J. Pinkerton, L. Li, Fibre laser welding of dissimilar alloys of Ti-6Al-4V and Inconel 718 for aerospace applications, Int. J. Adv. Manuf. Technol. 52 (2011) 977–987. https://doi.org/10.1007/s00170-010-2791-3.
[41] S.T. Auwal, S. Ramesh, F. Yusof, S.M. Manladan, A review on laser beam welding of titanium alloys, Int. J. Adv. Manuf. Technol. 97 (2018) 1071–1098. https://doi.org/10.1007/s00170-018-2030-x.
[42] M.M. Quazi, M. Ishak, M.A. Fazal, A. Arslan, S. Rubaiee, A. Qaban, M.H. Aiman, T. Sultan, M.M. Ali, S.M. Manladan, Current research and development status of dissimilar materials laser welding of titanium and its alloys, Opt. Laser Technol. 126 (2020). https://doi.org/10.1016/j.optlastec.2020.106090.
[43] S.S. Gorthi, P. Rastogi, Fringe projection techniques: Whither we are?, Opt. Lasers Eng. 48 (2010) 133–140. https://doi.org/10.1016/j.optlaseng.2009.09.001.
[44] Z. Wang, D.A. Nguyen, J.C. Barnes, Some practical considerations in fringe projection profilometry, Opt. Lasers Eng. 48 (2010) 218–225. https://doi.org/10.1016/j.optlaseng.2009.06.005.
[45] Metals Handbook, Vol.1 - Properties and Selection: Irons, Steels, and High-Performance Alloys, ASM International, 1990.
[46] Metals Handbook, Vol.2 - Properties and Selection: Nonferrous Alloys and Special-Purpose Materials, ASM International, 1990.
[47] A.T. DeWald, M.R. Hill, Multi-Axial Contour Method for Mapping Residual Stresses in Continuously Processed Bodies, Exp. Mech. 46 (2006) 473–490. https://doi.org/10.1007/s11340-006-8446-5.
[48] S. Zhang, High-Speed 3D Imaging with Digital Fringe Projection Techniques, CRC Press, 2018.
[49] P.J. Besl, N.D. McKay, A Method for Registration of 3-D Shapes, IEEE Trans. Pattern Anal. Mach. Intell. 14 (1992) 239–256. https://doi.org/10.1109/34.121791.
[50] European Committee for Standardization EN 15305:2008 E, Non-destructive Testing – Test Method for Residual Stress analysis by X-ray Diffraction, (2008).
[51] P. Pagliaro, M.B. Prime, J.S. Robinson, B. Clausen, H. Swenson, M. Steinzig, B. Zuccarello, Measuring Inaccessible Residual Stresses Using Multiple Methods and Superposition, Exp. Mech. 51 (2011) 1123–1134. https://doi.org/10.1007/s11340-010-9424-5.
[52] S. Kalpakjian, Manufacturing Engineering & Technology, Pearson Education India, 2001.
[53] C.T. Dawes, Laser Welding. A practical guide, Woodhead Publishing, 1992.
[54] A. Joseph, S.K. Rai, T. Jayakumar, N. Murugan, Evaluation of residual stresses in dissimilar weld joints, Int. J. Press. Vessel. Pip. 82 (2005) 700–705. https://doi.org/10.1016/j.ijpvp.2005.03.006.
[55] C.L. Jenney, A.O. Brien, eds., Welding Handbook, 9th ed., Woodhead Publishing, 2001. https://doi.org/10.1007/978-1-349-05561-6.

[56] C.H. Lee, K.H. Chang, Numerical analysis of residual stresses in welds of similar or dissimilar steel weldments under superimposed tensile loads, Comput. Mater. Sci. 40 (2007) 548–556. https://doi.org/10.1016/j.commatsci.2007.02.005.
[57] G. Totten, M. Howes, T. Inoue, Handbook of residual stress and deformation of steel, ASM International, 2002.
[58] Y. Fang, X. Jiang, D. Mo, D. Zhu, Z. Luo, A review on dissimilar metals' welding methods and mechanisms with interlayer, Int. J. Adv. Manuf. Technol. 102 (2019) 2845–2863. https://doi.org/10.1007/s00170-019-03353-6.
[59] T. Wu, Y. Ma, H. Xia, P. Geng, T. Niendorf, N. Ma, Measurement and simulation of residual stresses in laser welded CFRP/steel lap joints, Compos. Struct. 292 (2022) 115687. https://doi.org/10.1016/j.compstruct.2022.115687.
[60] N. Farabi, D.L. Chen, Y. Zhou, Microstructure and mechanical properties of laser welded dissimilar DP600/DP980 dual-phase steel joints, J. Alloys Compd. 509 (2011) 982–989. https://doi.org/10.1016/j.jallcom.2010.08.158.
[61] W. V. Vaidya, M. Horstmann, V. Ventzke, B. Petrovski, M. Koçak, R. Kocik, G. Tempus, Improving interfacial properties of a laser beam welded Dissimilar joint of aluminium AA6056 and titanium Ti6Al4V for aeronautical applications, J. Mater. Sci. 45 (2010) 6242–6254. https://doi.org/10.1007/s10853-010-4719-6.
[62] Z. Zhou, X. Gao, Y. Zhang, Research Progress on Characterization and Regulation of Forming Quality in Laser Joining of Metal and Polymer, and Development Trends of Lightweight Automotive Applications, Metals (Basel). 12 (2022). https://doi.org/10.3390/met12101666.
[63] V. Handa, P. Goyal, S. Sehgal, Low Cost Joining of Inconel 625 and Super Duplex Stainless Steel 2507 through Novel Technique, J. Mater. Eng. Perform. 32 (2023) 170–175. https://doi.org/10.1007/s11665-022-07092-w.
[64] V. Handa, P. Goyal, S. Sehgal, Application of graphite rods in producing Inconel 625 (UNS N06625) joints through the use of microwave radiation energy, Indian J. Eng. Mater. Sci. 29 (2022) 378–384. https://doi.org/10.56042/ijems.v29i3.65756.
[65] X. Hao, H. Dong, Y. Xia, P. Li, Microstructure and mechanical properties of laser welded TC4 titanium alloy/304 stainless steel joint with (CoCrFeNi)100-xCux high-entropy alloy interlayer, J. Alloys Compd. 803 (2019) 649–657. https://doi.org/10.1016/j.jallcom.2019.06.225.
[66] H. Liu, Y. Aoki, Y. Aoki, K. Ushioda, H. Fujii, Principle for obtaining high joint quality in dissimilar friction welding of Ti-6Al-4V alloy and SUS316L stainless steel, J. Mater. Sci. Technol. 46 (2020) 211–224. https://doi.org/10.1016/j.jmst.2019.10.037.
[67] G. Liu, X. Gao, C. Peng, Y. Huang, H. Fang, Y. Zhang, D. You, Z. Nanfeng, Optimization of laser welding of DP780 to Al5052 joints for weld width and lap-shear force using response surface methodology, Opt. Laser Technol. 126

(2020) 106072. https://doi.org/10.1016/j.optlastec.2020.106072.
[68] P. Corigliano, V. Crupi, Review of fatigue assessment approaches for welded marine joints and structures, Met. 2022, Vol. 12, Page 1010. 29 (2022) 1–34. https://doi.org/10.3390/MET12061010.
[69] Z. Zhu, K.Y. Lee, X. Wang, Ultrasonic welding of dissimilar metals, AA6061 and Ti6Al4V, Int. J. Adv. Manuf. Technol. 59 (2012) 569–574. https://doi.org/10.1007/s00170-011-3534-9.
[70] J. Seretsky, E.R. Ryba, Laser Welding of Dissimilar Metals: Titanium To Nickel., Weld. J. (Miami, Fla). 55 (1976) 208–211.
[71] S. Chatterjee, T.A. Abinandanan, K. Chattopadhyay, Microstructure development during dissimilar welding: Case of laser welding of Ti with Ni involving intermetallic phase formation, J. Mater. Sci. 41 (2006) 643–652. https://doi.org/10.1007/s10853-006-6480-4.
[72] S. Chatterjee, T.A. Abinandanan, K. Chattopadhyay, Phase formation in Ti/Ni dissimilar welds, Mater. Sci. Eng. A. 490 (2008) 7–15. https://doi.org/10.1016/j.msea.2007.12.041.
[73] Y. Zhang, X. Gao, D. You, X. Jiang, W. Ge, Investigation of Laser Butt Welding of AISI 304L and Q235 Steels Based on Numerical and Experimental Analyses, Metals (Basel). 12 (2022). https://doi.org/10.3390/met12050803.
[74] N.B. Pugacheva, A.M. Orishich, E.G. Volkova, A. V. Makarov, E.I. Senaeva, A.G. Malikov, Role of ultra-fine intermetallic particles and martensite in strengthening of AISI 321/Cu/Ti laser welded joint, Mater. Charact. 185 (2022) 111702. https://doi.org/10.1016/j.matchar.2021.111702.
[75] Y. Gao, L. Huang, Q. An, Y. Bao, X. Li, J. Zhang, L. Geng, Microstructure evolution and mechanical properties of titanium matrix composites and Ni-based superalloy joints with Cu interlayer, J. Alloys Compd. 764 (2018) 665–673. https://doi.org/10.1016/j.jallcom.2018.06.107.
[76] Y. Gao, L. Huang, Y. Bao, Q. An, Y. Sun, R. Zhang, L. Geng, J. Zhang, Joints of TiBw/Ti6Al4V composites- Inconel 718 alloys dissimilar joining using Nb and Cu interlayers, J. Alloys Compd. 822 (2020). https://doi.org/10.1016/j.jallcom.2019.153559.
[77] X.L. Gao, J. Liu, L.J. Zhang, Dissimilar metal welding of Ti6Al4V and Inconel 718 through pulsed laser welding-induced eutectic reaction technology, Int. J. Adv. Manuf. Technol. 96 (2018) 1061–1071. https://doi.org/10.1007/s00170-018-1633-6.
[78] J. Liu, H. Liu, X.L. Gao, H. Yu, Microstructure and mechanical properties of laser welding of Ti6Al4V to Inconel 718 using Nb/Cu interlayer, J. Mater. Process. Technol. 277 (2020). https://doi.org/10.1016/j.jmatprotec.2019.116467.
[79] T. Shehbaz, F.N. Khan, M. Junaid, J. Haider, Investigating nanoindentation creep behavior of pulsed-tig welded inconel 718 and commercially pure titanium using a vanadium interlayer, Metals (Basel). 11 (2021) 1492. https://doi.org/10.3390/met11091492.

[80] J. Wojewoda-Budka, M. Bugajska, J. Guspiel, S. Terlicka, A. Bigos, A. Wierzbicka-Miernik, Z. Szulc, On Selected Properties of Inconel 625/Ti6Al4V Explosively Welded Clad, J. Mater. Eng. Perform. 31 (2022) 7080–7087. https://doi.org/10.1007/s11665-022-06897-z.

[81] F. Gao, Z. Sun, S. Yang, P. Jiang, Z. Liao, Stress corrosion characteristics of electron beam welded titanium alloys joints in NaCl solution, Mater. Charact. 192 (2022) 112126. https://doi.org/10.1016/j.matchar.2022.112126.

[82] V. Crupi, E. Guglielmino, A. Risitano, D. Taylor, Different Methods for Fatigue Assessment of T Welded Joints Used in Ship Structures, J. Sh. Res. 51 (2007) 150–159. https://doi.org/10.5957/jsr.2007.51.2.150.

[83] L. Mujica, S. Weber, H. Pinto, C. Thomy, F. Vollertsen, Microstructure and mechanical properties of laser-welded joints of TWIP and TRIP steels, Mater. Sci. Eng. A. 527 (2010) 2071–2078. https://doi.org/10.1016/j.msea.2009.11.050.

[84] K.D. Ramkumar, P.S.G. Kumar, V.R. Krishna, A. Chandrasekhar, S. Dev, W.S. Abraham, S. Prabhakaran, S. Kalainathan, R. Sridhar, Influence of laser peening on the tensile strength and impact toughness of dissimilar welds of Inconel 625 and UNS S32205, Mater. Sci. Eng. A. 676 (2016) 88–99. https://doi.org/10.1016/j.msea.2016.08.104.

[85] M. Logesh, R. Selvabharathi, T. Thangeeswari, S. Palani, Influence of severe double shot peening on microstructure properties of Ti 6Al-4V and Titanium Grade 2 dissimilar joints using laser beam welding, Opt. Laser Technol. 123 (2020) 105883. https://doi.org/10.1016/j.optlastec.2019.105883.

[86] C. Du, X. Wang, L. Hu, Microstructure, mechanical properties and residual stress of a 2205DSS/Q235 rapidly formed LBW joint, J. Mater. Process. Technol. 256 (2018) 78–86. https://doi.org/10.1016/j.jmatprotec.2018.02.007.

[87] A. Scialpi, M. De Giorgi, L.A.C. De Filippis, R. Nobile, F.W. Panella, Mechanical analysis of ultra-thin friction stir welding joined sheets with dissimilar and similar materials, Mater. Des. 29 (2008) 928–936. https://doi.org/10.1016/j.matdes.2007.04.006.

[88] W. Zhang, W. Jiang, X. Zhao, S.T. Tu, Fatigue life of a dissimilar welded joint considering the weld residual stress: Experimental and finite element simulation, Int. J. Fatigue. 109 (2018) 182–190. https://doi.org/10.1016/j.ijfatigue.2018.01.002.

[89] H.W. Ahmad, J.H. Hwang, J.H. Lee, D.H. Bae, Welding residual stress analysis and fatigue strength assessment of multi-pass dissimilar materialwelded joint between alloy 617 and 12Cr steel, Metals (Basel). 8 (2018). https://doi.org/10.3390/met8010021.

[90] G. Janardhan, K. Kishore, G. Mukhopadhyay, K. Dutta, Fatigue Properties of Resistance Spot Welded Dissimilar Interstitial-Free and High Strength Micro-Alloyed Steel Sheets, Met. Mater. Int. 27 (2021) 3432–3448. https://doi.org/10.1007/s12540-020-00678-w.

[91] G. Meneghetti, A. Campagnolo, D. Berto, E. Pullin, S. Masaggia, Fatigue

strength of austempered ductile iron-to-steel dissimilar arc-welded joints, Weld. World. 65 (2021) 667–689. https://doi.org/10.1007/s40194-020-01058-z.
[92] S. Carone, V. Moramarco, G. Pappalettera, G. Barbieri, C. Casavola, Residual stress measurement on Titanium Grade 5 and Inconel 625 thin dissimilar welded joints by contour method, J. Mater. Sci. 57 (2022) 671–686. https://doi.org/10.1007/s10853-021-06581-y.
[93] P. Corigliano, V. Crupi, Fatigue analysis of TI6AL4V/INCONEL 625 dissimilar welded joints, Ocean Eng. 221 (2021) 2–8. https://doi.org/10.1016/j.oceaneng.2021.108582.
[94] A. Achouri, F. Hosseinzadeh, P.J. Bouchard, S. Paddea, O. Muransky, The incremental contour method using asymmetric stiffness cuts, Mater. Des. 197 (2021). https://doi.org/10.1016/j.matdes.2020.109268.
[95] P. Pagliaro, M.B. Prime, H. Swenson, B. Zuccarello, Measuring multiple residual-stress components using the Contour method and multiple cuts, Exp. Mech. 50 (2010) 187–194. https://doi.org/10.1007/s11340-009-9280-3.
[96] P. Corigliano, On the Compression Instability during Static and Low-Cycle Fatigue Loadings of AA 5083 Welded Joints: Full-Field and Numerical Analyses, J. Mar. Sci. Eng. 10 (2022) 212. https://doi.org/10.3390/jmse10020212.
[97] S. Carone, P. Corigliano, G. Epasto, V. Moramarco, G. Palomba, G. Pappalettera, C. Casavola, Innovative Approach for the Evaluation of the Mechanical Behavior of Dissimilar Welded Joints, Metals (Basel). 12 (2022). https://doi.org/10.3390/met12122039.
[98] P. Corigliano, V. Crupi, X. Pei, P. Dong, DIC-based structural strain approach for low-cycle fatigue assessment of AA 5083 welded joints, Theor. Appl. Fract. Mech. 116 (2021) 103090. https://doi.org/10.1016/j.tafmec.2021.103090.
[99] C.H. Lee, K.H. Chang, V.N. Van Do, Modeling the high cycle fatigue behavior of T-joint fillet welds considering weld-induced residual stresses based on continuum damage mechanics, Eng. Struct. 125 (2016) 205–216. https://doi.org/10.1016/j.engstruct.2016.07.002.
[100] F. Shen, B. Zhao, L. Li, C.K. Chua, K. Zhou, Fatigue damage evolution and lifetime prediction of welded joints with the consideration of residual stresses and porosity, Int. J. Fatigue. 103 (2017) 272–279. https://doi.org/10.1016/j.ijfatigue.2017.06.014.
[101] Y. Murakami, K. Miller, What is fatigue damage? A view point from the observation of low cycle fatigue process, Int. J. Fatigue. 27 (2005) 991–1005. https://doi.org/10.1016/j.ijfatigue.2004.10.009.
[102] T.L. Panontin, M.R. Hill, The effect of residual stresses on brittle and ductile fracture initiation predicted by micromechanical models, Int. J. Fract. 82 (1996) 317–333. https://doi.org/10.1007/BF00013236.
[103] C. Wei, Z. Zhang, D. Cheng, Z. Sun, M. Zhu, L. Li, An overview of laser-based multiple metallic material additive manufacturing: From macro: From micro-scales, Int. J. Extrem. Manuf. 3 (2021). https://doi.org/10.1088/2631-

7990/abce04.
[104] D.R. Feenstra, R. Banerjee, H.L. Fraser, A. Huang, A. Molotnikov, N. Birbilis, Critical review of the state of the art in multi-material fabrication via directed energy deposition, Curr. Opin. Solid State Mater. Sci. 25 (2021). https://doi.org/10.1016/j.cossms.2021.100924.
[105] C. Zhang, F. Chen, Z. Huang, M. Jia, G. Chen, Y. Ye, Y. Lin, W. Liu, B. Chen, Q. Shen, L. Zhang, E.J. Lavernia, Additive manufacturing of functionally graded materials: A review, Mater. Sci. Eng. A. 764 (2019). https://doi.org/10.1016/j.msea.2019.138209.
[106] J. Zhang, X. Wang, J. Gao, L. Zhang, B. Song, L. Zhang, Y. Yao, J. Lu, Y. Shi, Additive manufacturing of Ti–6Al–4V/Al–Cu–Mg multi-material structures with a Cu interlayer, Int. J. Mech. Sci. 256 (2023) 108477. https://doi.org/10.1016/j.ijmecsci.2023.108477.
[107] Z. Liu, M.A. Meyers, Z. Zhang, R.O. Ritchie, Functional gradients and heterogeneities in biological materials: Design principles, functions, and bioinspired applications, Prog. Mater. Sci. 88 (2017) 467–498. https://doi.org/10.1016/j.pmatsci.2017.04.013.
[108] C. Wei, L. Li, Recent progress and scientific challenges in multi-material additive manufacturing via laser-based powder bed fusion, Virtual Phys. Prototyp. 16 (2021) 347–371. https://doi.org/10.1080/17452759.2021.1928520.
[109] V. Errico, P. Posa, A. Fusco, A. Angelastro, S.L. Campanelli, Intralayer multi-material structure stainless-steel/nickel-superalloy fabricated via laser-powder bed fusion process, Manuf. Lett. 35 (2023) 11–15. https://doi.org/10.1016/j.mfglet.2022.11.004.
[110] W. Woo, D.K. Kim, E.J. Kingston, V. Luzin, F. Salvemini, M.R. Hill, Effect of interlayers and scanning strategies on through-thickness residual stress distributions in additive manufactured ferritic-austenitic steel structure, Mater. Sci. Eng. A. 744 (2019) 618–629. https://doi.org/10.1016/j.msea.2018.12.078.
[111] V. Errico, P. Posa, L. Liang, M. Maurizi, D. Wan, A. Angelastro, C. Gao, S.L. Campanelli, F. Berto, Layer-level AISI 316L-18Ni (300) Maraging multi-material fabrication via Laser-Powder Bed Fusion, Mater. Sci. Eng. A. 886 (2023) 145731. https://doi.org/10.1016/j.msea.2023.145731.
[112] J.L. Bartlett, X. Li, An overview of residual stresses in metal powder bed fusion, Addit. Manuf. 27 (2019) 131–149. https://doi.org/10.1016/j.addma.2019.02.020.
[113] Z.C. Fang, Z.L. Wu, C.G. Huang, C.W. Wu, Review on residual stress in selective laser melting additive manufacturing of alloy parts, Opt. Laser Technol. 129 (2020). https://doi.org/10.1016/j.optlastec.2020.106283.
[114] B. Ahmad, S.O. van der Veen, M.E. Fitzpatrick, H. Guo, Residual stress evaluation in selective-laser-melting additively manufactured titanium (Ti-6Al-4V) and inconel 718 using the contour method and numerical simulation,

Addit. Manuf. 22 (2018) 571–582. https://doi.org/10.1016/j.addma.2018.06.002.
[115] C.M. Smudde, C.W. San Marchi, M.R. Hill, J.C. Gibeling, Evaluation of residual stress reproducibility and orientation dependent fatigue crack growth in powder bed fusion stainless steel, Mater. Sci. Eng. A. 879 (2023) 145266. https://doi.org/10.1016/j.msea.2023.145266.
[116] M. Braun, E. Mayer, I. Kryukov, C. Wolf, S. Böhm, A. Taghipour, R.E. Wu, S. Ehlers, S. Sheikhi, Fatigue strength of PBF-LB/M and wrought 316L stainless steel: effect of post-treatment and cyclic mean stress, Fatigue Fract. Eng. Mater. Struct. 44 (2021) 3077–3093. https://doi.org/10.1111/ffe.13552.
[117] C. Shi, N. Nouri, V. Schulze, S. Dietrich, High cycle fatigue behaviour of AISI 4140 steel manufactured by laser-powder bed fusion, Int. J. Fatigue. 168 (2023). https://doi.org/10.1016/j.ijfatigue.2022.107469.
[118] P. Mercelis, J.P. Kruth, Residual stresses in selective laser sintering and selective laser melting, Rapid Prototyp. J. 12 (2006) 254–265. https://doi.org/10.1108/13552540610707013.
[119] J.P. Kruth, J. Deckers, E. Yasa, R. Wauthlé, Assessing and comparing influencing factors of residual stresses in selective laser melting using a novel analysis method, Proc. Inst. Mech. Eng. Part B J. Eng. Manuf. 226 (2012) 980–991. https://doi.org/10.1177/0954405412437085.
[120] A.S. Wu, D.W. Brown, M. Kumar, G.F. Gallegos, W.E. King, An Experimental Investigation into Additive Manufacturing-Induced Residual Stresses in 316L Stainless Steel, Metall. Mater. Trans. A Phys. Metall. Mater. Sci. 45 (2014) 6260–6270. https://doi.org/10.1007/s11661-014-2549-x.
[121] M. Strantza, R.K. Ganeriwala, B. Clausen, T.Q. Phan, L.E. Levine, D.C. Pagan, J.P.C. Ruff, W.E. King, N.S. Johnson, R.M. Martinez, V. Anghel, G. Rafailov, D.W. Brown, Effect of the scanning strategy on the formation of residual stresses in additively manufactured Ti-6Al-4V, Addit. Manuf. 45 (2021). https://doi.org/10.1016/j.addma.2021.102003.
[122] T. Simson, A. Emmel, A. Dwars, J. Böhm, Residual stress measurements on AISI 316L samples manufactured by selective laser melting, Addit. Manuf. 17 (2017) 183–189. https://doi.org/10.1016/j.addma.2017.07.007.
[123] T. Mishurova, K. Artzt, J. Haubrich, G. Requena, G. Bruno, New aspects about the search for the most relevant parameters optimizing SLM materials, Addit. Manuf. 25 (2019) 325–334. https://doi.org/10.1016/j.addma.2018.11.023.
[124] H. Ali, H. Ghadbeigi, K. Mumtaz, Effect of scanning strategies on residual stress and mechanical properties of Selective Laser Melted Ti6Al4V, Mater. Sci. Eng. A. 712 (2018) 175–187. https://doi.org/10.1016/j.msea.2017.11.103.
[125] C. Casavola, S.L. Campanelli, C. Pappalettere, Preliminary investigation on distribution of residual stress generated by the selective laser melting process, J. Strain Anal. Eng. Des. 44 (2009) 93–104. https://doi.org/10.1243/03093247JSA464.
[126] Y. Li, K. Zhou, P. Tan, S.B. Tor, C.K. Chua, K.F. Leong, Modeling temperature

and residual stress fields in selective laser melting, Int. J. Mech. Sci. 136 (2018) 24–35. https://doi.org/10.1016/j.ijmecsci.2017.12.001.

[127] Z. Shan, M.T. Tran, W. Woo, S.K. Hwang, H. Wang, V. Luzin, E.J. Kingston, M.R. Hill, A. DeWald, D.K. Kim, Multiscale framework for prediction of residual stress in additively manufactured functionally graded material, Addit. Manuf. 61 (2023) 103378. https://doi.org/10.1016/j.addma.2022.103378.

[128] R. Ghanavati, H. Naffakh-Moosavy, M. Moradi, E. Gadalińska, A. Saboori, Residual stresses and distortion in additively-manufactured SS316L-IN718 multi-material by laser-directed energy deposition: A validated numerical-statistical approach, J. Manuf. Process. 108 (2023) 292–309. https://doi.org/10.1016/j.jmapro.2023.11.018.

[129] L. Li, X. Zhang, W. Cui, F. Liou, W. Deng, W. Li, Temperature and residual stress distribution of FGM parts by DED process: modeling and experimental validation, Int. J. Adv. Manuf. Technol. 109 (2020) 451–462. https://doi.org/10.1007/s00170-020-05673-4.

[130] G. Shin, M. Ebrahimian, N.K. Adomako, H. Choi, D.J. Lee, J.H. Yoon, D.W. Kim, J.Y. Kang, M.Y. Na, H.J. Chang, J.H. Kim, Microstructural evolution and mechanical properties of functionally graded austenitic–low-carbon steel produced via directed energy deposition, Mater. Des. 227 (2023) 111681. https://doi.org/10.1016/j.matdes.2023.111681.

[131] H. Zhao, C. Gao, Z. Wang, Q. Wang, C. Liu, Y. Zhan, Residual stress analysis of TC4/Inconel718 functionally graded material produced by laser additive manufacturing based on progressive activation element method, Int. J. Adv. Manuf. Technol. 129 (2023) 1443–1453. https://doi.org/10.1007/s00170-023-12348-3.

[132] T.A. Rodrigues, F.W. Cipriano Farias, K. Zhang, A. Shamsolhodaei, J. Shen, N. Zhou, N. Schell, J. Capek, E. Polatidis, T.G. Santos, J.P. Oliveira, Wire and arc additive manufacturing of 316L stainless steel/Inconel 625 functionally graded material: Development and characterization, J. Mater. Res. Technol. 21 (2022) 237–251. https://doi.org/10.1016/j.jmrt.2022.08.169.

[133] S.C. Bodner, L.T.G. van de Vorst, J. Zalesak, J. Todt, J.F. Keckes, V. Maier-Kiener, B. Sartory, N. Schell, J.W. Hooijmans, J.J. Saurwalt, J. Keckes, Inconel-steel multilayers by liquid dispersed metal powder bed fusion: Microstructure, residual stress and property gradients, Addit. Manuf. 32 (2020) 101027. https://doi.org/10.1016/j.addma.2019.101027.

[134] S.C. Bodner, K. Hlushko, L.T.G. Van De Vorst, M. Meindlhumer, J. Todt, M.A. Nielsen, J.W. Hooijmans, J.J. Saurwalt, S. Mirzaei, J. Keckes, Graded Inconel-stainless steel multi-material structure by inter- and intralayer variation of metal alloys, J. Mater. Res. Technol. 21 (2022) 4846–4859. https://doi.org/10.1016/j.jmrt.2022.11.064.

[135] A. Alafaghani, A. Qattawi, M.A.G. Castañón, Effect of manufacturing parameters on the microstructure and mechanical properties of metal laser

sintering parts of precipitate hardenable metals, Int. J. Adv. Manuf. Technol. 99 (2018) 2491–2507. https://doi.org/10.1007/s00170-018-2586-5.
[136] I. Tolosa, F. Garciandía, F. Zubiri, F. Zapirain, A. Esnaola, Study of mechanical properties of AISI 316 stainless steel processed by "selective laser melting", following different manufacturing strategies, Int. J. Adv. Manuf. Technol. 51 (2010) 639–647. https://doi.org/10.1007/s00170-010-2631-5.
[137] R. Zhang, X. Li, X. Hou, J. Mo, J.A. de Oliveira, F. Wang, Y. Zhang, J. Li, S. Paddea, H. Dong, S. Zhang, Residual stress mapping in additively manufactured steel mould parts using asymmetric and multiple cuts contour method, J. Manuf. Process. 102 (2023) 1000–1009. https://doi.org/10.1016/j.jmapro.2023.08.019.
[138] V. Errico, P. Posa, M. Mazzarisi, A. Angelastro, S.L. Campanelli, Effects of Laser-Deposited Maraging Steel on L-PBF 316L Component, Metals (Basel). 12 (2022). https://doi.org/10.3390/met12101669.
[139] M. Ghasri-Khouzani, H. Peng, R. Rogge, R. Attardo, P. Ostiguy, J. Neidig, R. Billo, D. Hoelzle, M.R. Shankar, Experimental measurement of residual stress and distortion in additively manufactured stainless steel components with various dimensions, Mater. Sci. Eng. A. 707 (2017) 689–700. https://doi.org/10.1016/j.msea.2017.09.108.
[140] T. Yu, M. Li, A. Breaux, M. Atri, S. Obeidat, C. Ma, Experimental and numerical study on residual stress and geometric distortion in powder bed fusion process, J. Manuf. Process. 46 (2019) 214–224. https://doi.org/10.1016/j.jmapro.2019.09.010.
[141] A. Angelastro, P. Posa, V. Errico, S.L. Campanelli, A Systematic Study on Layer-Level Multi-Material Fabrication of Parts via Laser-Powder Bed Fusion Process, Metals (Basel). 13 (2023) 1588. https://doi.org/10.3390/met13091588.
[142] V. Errico, A. Fusco, S.L. Campanelli, Effect of DED coating and DED + Laser scanning on surface performance of L-PBF stainless steel parts, Surf. Coatings Technol. 429 (2022) 127965. https://doi.org/10.1016/j.surfcoat.2021.127965.
[143] G. Casalino, S.L. Campanelli, N. Contuzzi, A.D. Ludovico, Experimental investigation and statistical optimisation of the selective laser melting process of a maraging steel, Opt. Laser Technol. 65 (2015) 151–158. https://doi.org/10.1016/j.optlastec.2014.07.021.
[144] E. D.'Accardi, D. Palumbo, V. Errico, A. Fusco, A. Angelastro, U. Galietti, Analysing the Probability of Detection of Shallow Spherical Defects by Means of Pulsed Thermography, J. Nondestruct. Eval. 42 (2023) 1–16. https://doi.org/10.1007/s10921-023-00936-y.
[145] A. Ben-Artzy, A. Reichardt, J.P. Borgonia, R.P. Dillon, B. McEnerney, A.A. Shapiro, P. Hosemann, Compositionally graded SS316 to C300 Maraging steel using additive manufacturing, Mater. Des. 201 (2021) 109500. https://doi.org/10.1016/j.matdes.2021.109500.
[146] S.L. Campanelli, N. Contuzzi, P. Posa, A. Angelastro, Study of the aging

treatment on selective laser melted maraging 300 steel, Mater. Res. Express. 6 (2019) 66580. https://doi.org/10.1088/2053-1591/ab0c6e.
[147] I. Serrano-Munoz, A. Ulbricht, T. Fritsch, T. Mishurova, A. Kromm, M. Hofmann, R.C. Wimpory, A. Evans, G. Bruno, Scanning Manufacturing Parameters Determining the Residual Stress State in LPBF IN718 Small Parts, Adv. Eng. Mater. 23 (2021). https://doi.org/10.1002/adem.202100158.
[148] I. Serrano-Munoz, T. Fritsch, T. Mishurova, A. Trofimov, D. Apel, A. Ulbricht, A. Kromm, R. Hesse, A. Evans, G. Bruno, On the interplay of microstructure and residual stress in LPBF IN718, J. Mater. Sci. 56 (2021) 5845–5867. https://doi.org/10.1007/s10853-020-05553-y.
[149] T. Mishurova, S. Cabeza, T. Thiede, N. Nadammal, A. Kromm, M. Klaus, C. Genzel, C. Haberland, G. Bruno, The Influence of the Support Structure on Residual Stress and Distortion in SLM Inconel 718 Parts, Metall. Mater. Trans. A Phys. Metall. Mater. Sci. 49 (2018) 3038–3046. https://doi.org/10.1007/s11661-018-4653-9.
[150] B. Clausen, C.R. D'Elia, M.B. Prime, M.R. Hill, J.E. Bishop, K.L. Johnson, B.H. Jared, K.M. Allen, D.K. Balch, R.A. Roach, D.W. Brown, Complementary Measurements of Residual Stresses Before and After Base Plate Removal in an Intricate Additively-Manufactured Stainless-Steel Valve Housing, Addit. Manuf. 36 (2020). https://doi.org/10.1016/j.addma.2020.101555.
[151] D. Wang, L. Liu, G. Deng, C. Deng, Y. Bai, Y. Yang, W. Wu, J. Chen, Y. Liu, Y. Wang, X. Lin, C. Han, Recent progress on additive manufacturing of multi-material structures with laser powder bed fusion, Virtual Phys. Prototyp. 17 (2022) 329–365. https://doi.org/10.1080/17452759.2022.2028343.
[152] A. Reichardt, A.A. Shapiro, R. Otis, R.P. Dillon, J.P. Borgonia, B.W. McEnerney, P. Hosemann, A.M. Beese, Advances in additive manufacturing of metal-based functionally graded materials, Int. Mater. Rev. 66 (2021) 1–29. https://doi.org/10.1080/09506608.2019.1709354.
[153] C. Tan, D. Wang, W. Ma, K. Zhou, Ultra-strong bond interface in additively manufactured iron-based multi-materials, Mater. Sci. Eng. A. 802 (2021) 140642. https://doi.org/10.1016/j.msea.2020.140642.
[154] C. Wei, L. Liu, H. Cao, X. Zhong, X. Xu, Y. Gu, D. Cheng, Y. Huang, Z. Li, W. Guo, Z. Liu, L. Li, Cu10Sn to Ti6Al4V bonding mechanisms in laser-based powder bed fusion multiple material additive manufacturing with different build strategies, Addit. Manuf. 51 (2022). https://doi.org/10.1016/j.addma.2021.102588.
[155] C. Tan, X. Zhang, D. Dong, B. Attard, D. Wang, M. Kuang, W. Ma, K. Zhou, In-situ synthesised interlayer enhances bonding strength in additively manufactured multi-material hybrid tooling, Int. J. Mach. Tools Manuf. 155 (2020) 103592. https://doi.org/10.1016/j.ijmachtools.2020.103592.
[156] D. De Baere, M. Moshiri, L. Smolej, J.H. Hattel, Numerical investigation into laser-based powder bed fusion of cantilevers produced in 300-grade maraging

steel, Addit. Manuf. 50 (2022). https://doi.org/10.1016/j.addma.2021.102560.
[157] Y. Huang, M.B. Khamesee, E. Toyserkani, A comprehensive analytical model for laser powder-fed additive manufacturing, Addit. Manuf. 12 (2016) 90–99. https://doi.org/10.1016/j.addma.2016.07.001.
[158] C. Kamath, Data mining and statistical inference in selective laser melting, Int. J. Adv. Manuf. Technol. 86 (2016) 1659–1677. https://doi.org/10.1007/s00170-015-8289-2.
[159] T.H. Becker, D. Dimitrov, The achievable mechanical properties of SLM produced Maraging Steel 300 components, Rapid Prototyp. J. 22 (2016) 487–494. https://doi.org/10.1108/RPJ-08-2014-0096.
[160] G.A. Webster, A.N. Ezeilo, Residual stress distributions and their influence on fatigue lifetimes, Int. J. Fatigue. 23 (2001) 375–383. https://doi.org/10.1016/s0142-1123(01)00133-5.
[161] C.S. Montross, T. Wei, L. Ye, G. Clark, Y.W. Mai, Laser shock processing and its effects on microstructure and properties of metal alloys: A review, Int. J. Fatigue. 24 (2002) 1021–1036. https://doi.org/10.1016/S0142-1123(02)00022-1.
[162] G.S. Schajer, M.B. Prime, Use of inverse solutions for residual stress measurements, J. Eng. Mater. Technol. 128 (2006) 375–382. https://doi.org/10.1115/1.2204952.
[163] M.B. Prime, M.R. Hill, Uncertainty, model error, and order selection for series-expanded, residual-stress inverse solutions, J. Eng. Mater. Technol. 128 (2006) 175–185. https://doi.org/10.1115/1.2172278.
[164] G.S. Schajer, Measurement of Non-Uniform Residual Stresses Using the Hole-Drilling Method. Part I—Stress Calculation Procedures, J. Eng. Mater. Technol. 110 (1988) 338–343. https://doi.org/10.1115/1.3226059.
[165] G.S. Schajer, Measurement of Non-Uniform Residual Stresses Using the Hole-Drilling Method. Part II—Practical Application of the Integral Method, J. Eng. Mater. Technol. 110 (1988) 344–349. https://doi.org/10.1115/1.3226060.
[166] G.S. Schajer, Hole-drilling residual stress profiling with automated smoothing, J. Eng. Mater. Technol. 129 (2007) 440–445. https://doi.org/10.1115/1.2744416.
[167] B. Zuccarello, Optimal calculation steps for the evaluation of residual stress by the incremental hole-drilling method, Exp. Mech. 39 (1999) 117–124. https://doi.org/10.1007/BF02331114.
[168] D. Vangi, Data management for the evaluation of residual stresses by the incremental hole-drilling method, J. Eng. Mater. Technol. Trans. ASME. 116 (1994) 561–566. https://doi.org/10.1115/1.2904329.
[169] G.S. Schajer, E. Altus, Stress calculation error analysis for incremental hole-drilling residual stress measurements, J. Eng. Mater. Technol. Trans. ASME. 118 (1996) 120–126. https://doi.org/10.1115/1.2805924.
[170] D. Peral, J. de Vicente, J.A. Porro, J.L. Ocaña, Uncertainty analysis for non-uniform residual stresses determined by the hole drilling strain gauge

method, Meas. J. Int. Meas. Confed. 97 (2017) 51–63. https://doi.org/10.1016/j.measurement.2016.11.010.
[171] T.C. Smit, R.G. Reid, Tikhonov regularization with Incremental Hole-Drilling and the Integral Method in Cross-Ply Composite Laminates, Exp. Mech. 60 (2020) 1135–1148. https://doi.org/10.1007/s11340-020-00629-x.
[172] J.P. Nobre, C. Polese, S.N. van Staden, Incremental Hole Drilling Residual Stress Measurement in Thin Aluminum Alloy Plates Subjected to Laser Shock Peening, Exp. Mech. 60 (2020) 553–564. https://doi.org/10.1007/s11340-020-00586-5.
[173] T.C. Smit, R.G. Reid, Imposition of Constraints on the Regularized Integral Method of Incremental Hole-Drilling, Exp. Mech. (2022). https://doi.org/10.1007/s11340-022-00851-9.
[174] T.C. Smit, R.G. Reid, Residual Stress Measurement in Composite Laminates Using Incremental Hole-Drilling with Power Series, Exp. Mech. 58 (2018) 1221–1235. https://doi.org/10.1007/s11340-018-0403-6.
[175] T.C. Smit, R.G. Reid, Use of Power Series Expansion for Residual Stress Determination by the Incremental Hole-Drilling Technique, Exp. Mech. 60 (2020) 1301–1314. https://doi.org/10.1007/s11340-020-00642-0.
[176] M.D. Olson, A.T. DeWald, M.R. Hill, Precision of Hole-Drilling Residual Stress Depth Profile Measurements and an Updated Uncertainty Estimator, Exp. Mech. 61 (2021) 549–564. https://doi.org/10.1007/s11340-020-00679-1.
[177] C. Cellard, D. Retraint, M. François, E. Rouhaud, D. Le Saunier, Laser shock peening of Ti-17 titanium alloy: Influence of process parameters, Mater. Sci. Eng. A. 532 (2012) 362–372. https://doi.org/10.1016/j.msea.2011.10.104.
[178] U. Trdan, J.A. Porro, J.L. Ocaña, J. Grum, Laser shock peening without absorbent coating (LSPwC) effect on 3D surface topography and mechanical properties of 6082-T651 Al alloy, Surf. Coatings Technol. 208 (2012) 109–116. https://doi.org/10.1016/j.surfcoat.2012.08.048.
[179] M.R. Viotti, A. Albertazzi, Approximated Repair Methods for Outlier Strain Data from Hole-Drilling Residual Measurements, Exp. Mech. 53 (2013) 393–403. https://doi.org/10.1007/s11340-012-9642-0.
[180] B. Gore, J.P. Nobre, Effects of Numerical Methods on Residual Stress Evaluation by the Incremental Hole-Drilling Technique Using the Integral Method, Mater. Res. Proc. 2 (2017) 587–592. https://doi.org/10.21741/9781945291173-99.
[181] C.E. Rasmussen, C.K.I. Williams, Gaussian processes for machine learning, The MIT Press, 2006.
[182] J. Wang, An Intuitive Tutorial to Gaussian Processes Regression, (2020). https://doi.org/http://arxiv.org/abs/2009.10862.
[183] A. Tognan, L. Laurenti, E. Salvati, Contour Method with Uncertainty Quantification: A Robust and Optimised Framework via Gaussian Process Regression, Exp. Mech. (2022). https://doi.org/10.1007/s11340-022-00842-w.

[184] JCGM 101:2008 Supplement 1 – Propagation of distributions using a Monte Carlo method, 1 (2008) 90.
[185] M.A. Attolico, C. Barile, C. Casavola, V. Moramarco, D. Furfari, D.O. Busse, Effects of Laser Shock Peening on Surface Roughness and Residual Stress of AA 7050-T7451, J. Mater. Eng. Perform. (2022). https://doi.org/10.1007/s11665-022-06857-7.
[186] C.A. Micchelli, Y. Xu, H. Zhang, Universal kernels, J. Mach. Learn. Res. 7 (2006) 2651–2667.
[187] D.K. Duvenaud, Automatic Model Construction with Gaussian Processes, University of Cambridge, 2014. https://www.cs.toronto.edu/~duvenaud/thesis.pdf.
[188] F. Pedregosa, G. Varoquaux, A. Gramfort, V. Michel, B. Thirion, 0. Grisel, M. Blondel, P. Prettenhofer, R. Weiss, V. Dubourg, J. Vanderplas, A. Passos, D. Cournapeau, M. Brucher, M. Perrot, E. Duchesnay, Scikitlearn: machine learning in python, J. Mach. Learn. Res. 12 (2011) 2825–2830.
[189] C. Correa, D. Peral, J.A. Porro, M. Díaz, L. Ruiz De Lara, A. García-Beltrán, J.L. Ocaña, Random-type scanning patterns in laser shock peening without absorbing coating in 2024-T351 Al alloy: A solution to reduce residual stress anisotropy, Opt. Laser Technol. 73 (2015) 179–187. https://doi.org/10.1016/j.optlastec.2015.04.027.
[190] M. Beghini, L. Bertini, C. Santus, A procedure for evaluating high residual stresses using the blind hole drilling method, including the effect of plasticity, J. Strain Anal. Eng. Des. 45 (2010) 301–318. https://doi.org/10.1243/03093247JSA579.
[191] J. Mathew, R. Kshirsagar, S. Zabeen, N. Smyth, S. Kanarachos, K. Langer, M.E. Fitzpatrick, Machine learning-based prediction and optimisation system for laser shock peening, Appl. Sci. 11 (2021). https://doi.org/10.3390/app11072888.
[192] P. Mylavarapu, C. Bhat, M.K.R. Perla, K. Banerjee, K. Gopinath, T. Jayakumar, Identification of critical material thickness for eliminating back reflected shockwaves in laser shock peening – A numerical study, Opt. Laser Technol. 142 (2021). https://doi.org/10.1016/j.optlastec.2021.107217.